

Institut für Informatik
Lehrstuhl für Robotik und Telematik
Prof. Dr. K. Schilling
Prof. Dr. A. Nüchter



Würzburger Forschungsberichte
in Robotik und Telematik

Uni Wuerzburg Research Notes
in Robotics and Telematics

Julius-Maximilians-

**UNIVERSITÄT
WÜRZBURG**

Band 15

Pablo A. Baier

Simulator for Minimally
Invasive Vascular
Interventions:
Hardware and Software



Die Schriftenreihe

wird vom Lehrstuhl für Informatik VII: Robotik und Telematik der Universität Würzburg herausgegeben und präsentiert innovative Forschung aus den Bereichen der Robotik und der Telematik.

Die Kombination fortgeschrittener Informationsverarbeitungsmethoden mit Verfahren der Regelungstechnik eröffnet hier interessante Forschungs- und Anwendungsperspektiven. Es werden dabei folgende interdisziplinäre Aufgabenschwerpunkte bearbeitet:

- Robotik und Mechatronik: Kombination von Informatik, Elektronik, Mechanik, Sensorik, Regelungs- und Steuerungstechnik, um Roboter adaptiv und flexibel ihrer Arbeitsumgebung anzupassen.
- Telematik: Integration von Telekommunikation, Informatik und Steuerungstechnik, um Dienstleistungen an entfernten Standorten zu erbringen.

Anwendungsschwerpunkte sind u.a. mobile Roboter, Tele-Robotik, Raumfahrtssysteme und Medizin-Robotik.

Lehrstuhl Informatik VII
Robotik und Telematik
Am Hubland
D-97074 Würzburg

Tel.: +49 (0) 931 - 31 - 86678
Fax: +49 (0) 931 - 31 - 86679

schi@informatik.uni-wuerzburg.de
<http://www7.informatik.uni-wuerzburg.de>

Dieses Dokument wird bereitgestellt
durch den Online-Publikationsservice
der Universität Würzburg.

Universitätsbibliothek Würzburg
Am Hubland
D-97074 Würzburg

Tel.: +49 (0) 931 - 31 - 85906

opus@bibliothek.uni-wuerzburg.de
<https://opus.bibliothek.uni-wuerzburg.de>

ISSN: 1868-7474 (online)
ISSN: 1868-7466 (print)
ISBN: 978-3-945459-22-5 (online)

Zitation dieser Publikation

BAIER, P. A. (2018). Simulator for Minimally Invasive Vascular Interventions: Hardware and Software. Schriftenreihe Würzburger Forschungsberichte in Robotik und Telematik, Band 15. Würzburg: Universität Würzburg.
URN: urn:nbn:de:bvb:20-opus-161190

Simulator for Minimally Invasive Vascular Interventions: Hardware and Software

Dissertation zur Erlangung des
naturwissenschaftlichen Doktorgrades
der Julius-Maximilians-Universität Würzburg

vorgelegt von

Pablo Alfredo Saip Baier

aus

Manaus - Brasilien

Würzburg 2018

Eingereicht am: 27.04.2017

bei der Fakultät für Mathematik und Informatik

1. Gutachter: Prof. Dr. Klaus Schilling

2. Gutachter: Prof. Dr. Sergio Montenegro

3. Gutachter: Prof. Dr. Med. Wolfram Voelker

Tag der mündlichen Prüfung: 25.04.2018

Acknowledgments

First and foremost I offer my sincerest gratitude to my advisor Prof. Dr. Klaus Schilling, who has supported me throughout my thesis with his patience and knowledge whilst allowing me the room to work in my own way. My sincere thanks also goes to Prof. Dr. Med. Wolfram Voelker, for his motivation and enthusiasm when receiving me at INTUS¹.

I would like to thank my fellow doctoral students for their feedback, cooperation and of course friendship and also to the office staff for all the instances in which their assistance helped me along the way. In particular, I am grateful to Dr. Lei Ma, Dr. Christian Herrmann, MSc. Lakshminarasimhan Srinivasan, Med. Nils Petri and Heidi Frankenberger. I also would like to thank for the technical support to Dieter Ziegler, Alfredo Baier and Med. Marcos Chahuan.

I would like to thank my Brazilian sponsor CNPq² for their support and patience. They never stop believe in me.

Last but not the least, I would like to thank my family: my parents 📞, brothers 🏠, wife ❤️ and children ✂️. Each one knows how important he/she was to this work.

¹Interdisziplinäres Trainings- und Simulationszentrum <http://www.intus-wuerzburg.de/>

²National Counsel of Technological and Scientific Developmen <http://www.cnpq.br/>

In memory of
Benjamin Jaramillo

Abstract

A complete simulation system is proposed that can be used as an educational tool by physicians in training basic skills of Minimally Invasive Vascular Interventions. In the first part, a surface model is developed to assemble arteries having a planar segmentation. It is based on Sweep Surfaces and can be extended to T- and Y-like bifurcations. A continuous force vector field is described, representing the interaction between the catheter and the surface. The computation time of the force field is almost unaffected when the resolution of the artery is increased.

The mechanical properties of arteries play an essential role in the study of the circulatory system dynamics, which has been becoming increasingly important in the treatment of cardiovascular diseases. In Virtual Reality Simulators, it is crucial to have a tissue model that responds in real time. In this work, the arteries are discretized by a two dimensional mesh and the nodes are connected by three kinds of linear springs. Three tissue layers (Intima, Media, Adventitia) are considered and, starting from the stretch-energy density, some of the elasticity tensor components are calculated. The physical model linearizes and homogenizes the material response, but it still contemplates the geometric nonlinearity. In general, if the arterial stretch varies by 1% or less, then the agreement between the linear and nonlinear models is trustworthy.

In the last part, the physical model of the wire proposed by Konings is improved. As a result, a simpler and more stable method is obtained to calculate the equilibrium configuration of the wire. In addition, a geometrical method is developed to perform relaxations. It is particularly useful when the wire is hindered in the physical method because of the boundary conditions. The physical and the geometrical methods are merged, resulting in efficient relaxations. Tests show that the shape of the virtual wire agrees with the experiment. The proposed algorithm allows real-time executions and the hardware to assemble the simulator has a low cost.

Contents

1	Introduction	1
1.1	Motivation	2
1.2	Contributions	6
1.3	Organization	7
2	Surfaces for Modeling Arteries	9
2.1	State of the Art	10
2.2	Methods	11
2.2.1	Surfaces	11
2.2.2	Catheter-Surface Interaction	14
2.3	Technical Evaluation	17
2.4	Software	20
2.5	Conclusions	22
3	Approximate Artery Elasticity	23
3.1	State of the Art	24
3.2	Methods	25
3.2.1	Elasticity Tensor	25
3.2.2	Spring Stiffness	28
3.2.2.1	Normal Spring κ_i	30
3.2.2.2	Angular Spring τ	30
3.2.2.3	Angular Spring ζ	33
3.2.2.4	Generalizations to Other Geometries	34
3.3	Pseudocode	36
3.4	Technical Evaluation	38
3.4.1	Stiffness Analysis	38
3.4.2	Comparison of Models	41
3.4.2.1	Pressure-Inflation	42
3.4.2.2	Axial Force	44
3.4.2.3	Bending	45
3.4.3	Large Stretch	46
3.5	Conclusions	46
4	Simulator	49
4.1	State of the Art	50
4.2	Methods	51
4.2.1	Physical Relaxation	52
4.2.1.1	Bending Energy	53

4.2.1.2	Energy Minimization	55
4.2.1.3	First Order Correction	58
4.2.1.4	Pseudocode	60
4.2.2	Geometrical Relaxation	61
4.2.2.1	Bending Energy	61
4.2.2.2	Energy Minimization	62
4.2.2.3	Point Slide	63
4.2.2.4	Cubic Spline	65
4.2.2.5	Interval Selection	66
4.2.2.6	Pseudocode	67
4.2.3	Combination of Physical and Geometrical Relaxation	68
4.2.4	Wire Device	68
4.3	Technical Evaluation	71
4.3.1	Stability Analysis	71
4.3.2	Segment Size	73
4.3.3	Physical and Geometrical Processing Time	73
4.3.4	Wire-Artery Contact	77
4.3.5	Comparison of Physical Models	78
4.3.6	Validation Tests	79
4.4	Software	80
4.5	Conclusions	81
5	Conclusions and Future Works	83
A	Formulary	87
	List of Abbreviations	89
	List of Figures	91
	List of Tables	99
	List of Algorithms	101
	References	103

Chapter 1

Introduction

1.1 Motivation

Over the last decades, Minimally Invasive Surgery (MIS) has revolutionized many surgical procedures [1]. The treatment is delivered using image guidance, so that skillful instrument navigation and a thorough understanding of the anatomy are critical to avoid complications. MIS surgery has demonstrably better quality-of-life outcomes than open surgery [2]. According to Fusch [3] “...two major drawbacks have emerged with the introduction of MIS: firstly, the prolonged learning curve for most surgeons, in comparison to the learning process in open surgery; and secondly, increased costs due to investment in the equipment required and the use of disposable instruments...”

Because MIS has a reduced sense of touch compared to open surgery, surgeons must rely more on the feeling of net forces resulting from tool-tissue interactions [4]. Thus longer training is needed to develop sufficient skills. The outcomes of surgical procedures and the possibility of medical training have been subject of exhaustive research [5].

The combination of traditional learning methods and technology enhances trainee satisfaction and skill acquisition level [6, 7]. The training methods include live observation of procedures, practicing on mechanical models, and hands-on training using human cadavers or live animals [8]. In the past, hands-on training was considered the best available method [9, 10]. However, it has ethical issues and it is also expensive, owing to the costs associated to the use of animals in the process and because the instruments can be used only once [11].

Nowadays, Virtual Reality Simulators (VRS) provide an initial training step to develop basics skills [12]. With the aid of simulation techniques, several training sessions can be performed, which provide certain levels of proficiency to the physician [13]. Moreover, no radiation is required and the simulation can be made specific [14]. Based on these findings, the US Food and Drug Administration accepted a proposal that VRS is an important component of a training package for carotid stenting: “*Trainees would learn catheter and wire handling skills on a high-fidelity VRS until the trainees achieved a level of proficiency in didactic and technical skills*” [15].

Cardiac catheterization (Fig. 1.1) is a Minimally Invasive Vascular Surgery (MIVS) commonly used to diagnose and treat heart conditions [17]. During catheterization, small tubes (catheter) are inserted into the circulatory system through the femoral artery and vein as the preferred access sites [18]. Using X-ray fluoroscopy, information is obtained about blood flow and pressures within the heart. As a result, it is determined if there are obstructions within the blood vessels feeding the heart muscle [19]. For interventional procedures (e.g. stenting and balloon angioplasty), a wire must be inserted through the catheter [20, 21] and maneuvered in the coronaries.

The wires are commonly fabricated from type 304 stainless steel [22], but some recent studies are trying replace metal by optical fiber, so that it can be used in Magnetic Resonance (MR) environments [23]. Thus, it offers new possibilities of measurements and analysis [24]. To control the motion of the catheter within the



Figure 1.1: *Interventional cardiologists from NewYork-Presbyterian Hospital and Columbia University Medical, performing a coronary angiogram in a cardiac catheterization laboratory. The C-Arm [16] generates/detects the X-Rays and the images are displayed on the screen.*

vascular network, the radiologist can push, pull or twist the proximal end of the device [25]. Achieving optimal outcomes requires operator skills in guiding the wire, as well as selecting and using the surgical tools [26].

In general, MIVS such as the ones showed in Fig. 1.2, are expensive and complex [27]. Procedures start with a needle insertion into the vascular system, but current commercial simulators skip this step¹ in order to reduce complexity and cost. The wire and the catheter are then manipulated within the vascular anatomy to navigate to the position of interest [29]. Rudin et al. [30] offer a vision for the future of this dynamic field in the form of predictions.

Local deformations are important because they increase the realism in proximity to the surgical tool [31]. However, changes in tool geometry cause variations in the force-deflection responses only for large localized deformations of tissues [32], which is not the case in catheter simulations. Thus, the catheter shape is not crucial and it can be represented by a curve discretized by points.

Simulators are also able to differentiate advanced from novice operators, suggesting that it is a valid tool in the assessment of performances [33]. VRS are not exclusively used for training purposes, because they can be easily customized to

¹Specific needle simulation can be practice in a different VRS [28].



Figure 1.2: Commercial VRS for endovascular procedures: (a) Mentice VIST-C (www.mentice.com), (b) CAE Cath VR (www.caehealthcare.com), and (c) Symbionix ANGIO Mentor (<http://symbionix.com>).

provide both medical programs and certification boards with an objective tool for assessing physician skill and knowledge [34].

Dawson et al. [35] proposed an organogram of a MIVS (Fig. 1.3). According to Sanz-Lopes et al. [36], the design of VRS, and more specifically those dedicated to surgery training, implies to take into account numerous constraints so that simulators look realistic and train proper skills for surgical procedures. Among those constraints, the accuracy of the biophysical models [37] remains a very hot topic, since parameter estimation and experimental validation often rely on invasive protocols that are obviously not suited for living beings [38]. In the context of Interventional Radiology, the procedures involve the navigation of surgical catheter tools inside the vascular network where many contacts, sliding, and friction phenomena occur [39].

According to Peterson et al. [41], one of the major components of the cardiovascular system is its arterial network, the mechanical properties of which determine the propagation of energy from the heart to the periphery. The relationships of blood flow and blood pressure [42], of intravascular pressure and vessel volume [43], of pulse wave velocity and blood pressure [44] are but a few of the variables often measured which depend, quantitatively, on the mechanical properties of the blood vessel walls.

The arterial wall is composed by three tissue layers: Intima, Media, and Adventitia [45]. A better understanding of the arterial wall mechanics can provide relevant information for medical diagnosis and therapies of some vascular pathologies [46]. For example, the measurements obtained by an Intravascular Ultrasound (IVUS) (Fig. 1.4) of the arterial tree stiffness, can be applied in routine clinical practice for risk stratification [47]. Detailed knowledge of vascular tissue properties is required to improve procedures such as angioplasty, to design arterial prostheses, and to describe the dynamics of the interaction between the heart and the circulatory system [48].

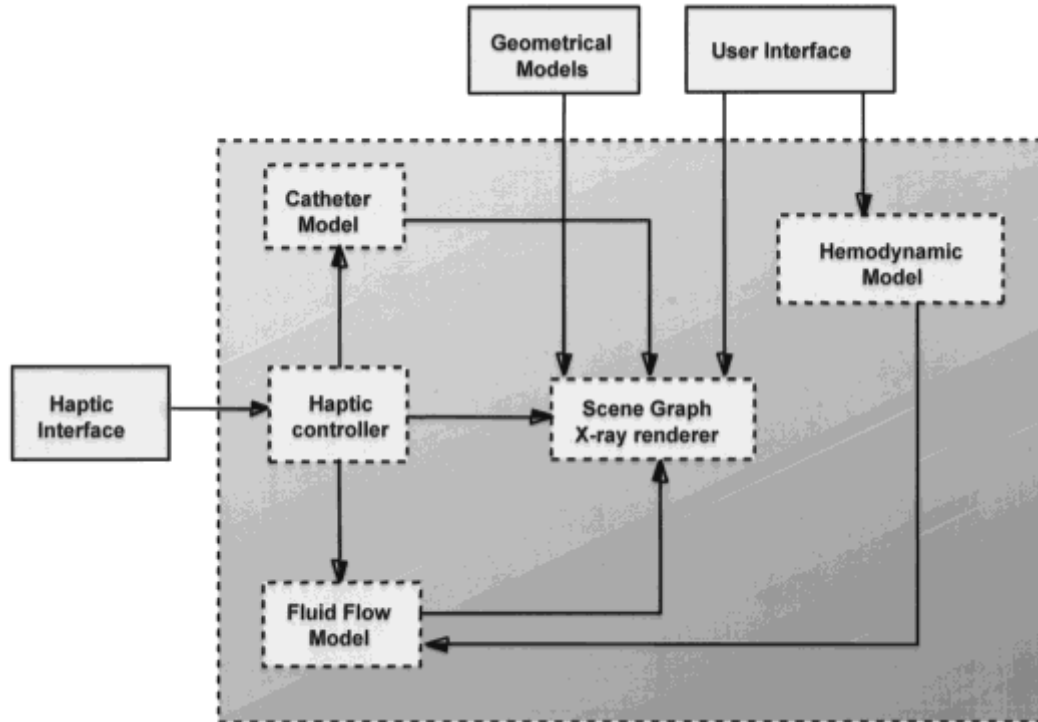


Figure 1.3: *Components of a real-time simulator proposed by Dawson et al. [35]. The user interacts with the haptics interface device containing catheters and guidewires linked to force-feedback mechanisms. A haptic controller integrates the catheter model, blood flow models, and synthetic fluoroscopy renderer. Hemodynamic models affect fluid flow and subsequent fluoroscopic appearance. Geometric models of anatomy and devices used during procedures provide tissue-tool interactions. The user interface relays information about the physiologic state of the patient (hemodynamic model) and the progress of the procedure through the fluoroscopic display.*

Moreover, in order to show the artery deformation caused by the introduction of medical devices, a truthful simulator of the MIVS must consider the physical models of the devices and of the artery [49, 50].

The mechanical properties of vascular tissues can not be described in terms of homogeneous cell agglomerations [51]. Tissues have microscopic and macroscopic organizations, which need to be considered in the context of multiple scales [52]. The arterial wall is incompressible, inhomogeneous, and exhibits hysteresis under a cyclic load [53]. When modeling the artery, a complex set of nonlinear equations results and considerable Processing Time (PT) is consumed to solve them [54].

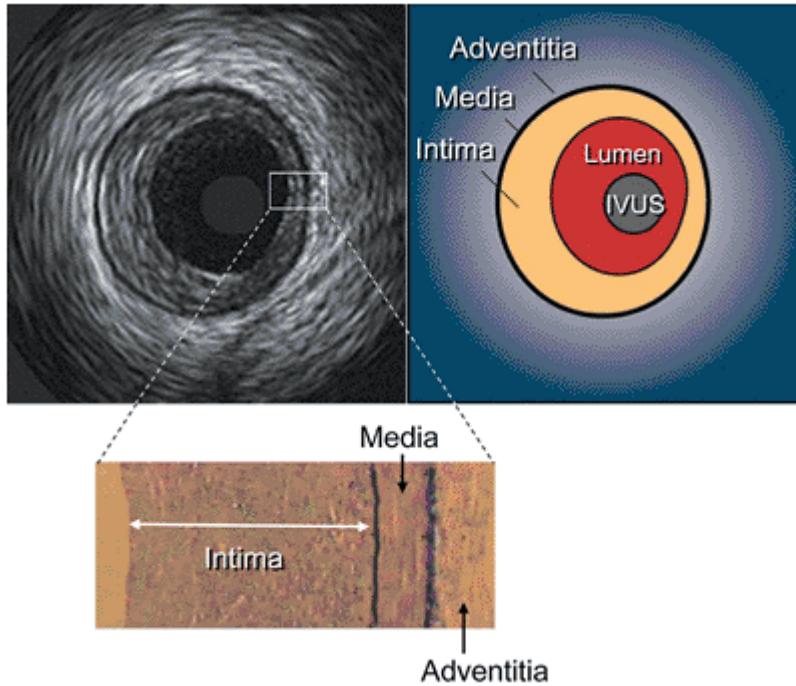


Figure 1.4: *Cross-sectional format of a typical IVUS image. The bright-dark-bright, three-layered appearance is seen in the image with corresponding anatomy as defined. The IVUS represents the imaging catheter in the blood vessel lumen. Histologic correlation with intima, media, and adventitia are shown. The media has lower ultrasound reflectance owing to less collagen and elastin compared with neighboring layers. Because the intimal layer reflects ultrasound more strongly than the media [40], there is a spillover in the image, which results in a slight overestimation of the thickness of the intima and a corresponding underestimation of the medial thickness (black and white image). Figure extracted from Moscucci [26].*

1.2 Contributions

The publications of the author are the Refs. [55–63] and the results appearing in this thesis have been published mainly in the last three ones. Specifically, the major contributions are:

- A model that assembles arteries and has planar segmentation to increase efficiency of the collision-detection algorithm. It is based on Sweep Surfaces and can be extended to T- and Y-like bifurcations.
- Description of a continuous force vector field, representing the interaction between the catheter and the surface of the artery.
- Linearization of an artery model to calculate the stiffness of springs used in

Two-Dimensional (2D) Finite Element Method (FEM).

- In comparison with the paper of Konings et al. [64]:
 - The wire model is more accurate, especially when the bending is large.
 - The update equations are simpler and the calculations are faster.
 - The wire segment can be introduced at once (it is not necessary to make subdivisions).
- A new method, the Geometrical Relaxation (GR), is introduced. It helps to improve the speed when the wire is hindered by boundary conditions.
- A hardware device is described, which is simple to deploy and has a low cost. This can help to disseminate the technique and make it widespread.

1.3 Organization

The chapters are independent, complementary, and are organized as follows:

- Chapter 2 (based on Ref. [61])

A model is proposed to assemble arteries which includes planar segmentation, increasing the efficiency of the collision-detection algorithm. Specifically, in Section 2.2.1 the *Sweep Surfaces* and the T- and Y-like bifurcations are described. Then, in Section 2.2.2 a continuous force vector field, representing the interaction between the catheter and the surface, is presented.

- Chapter 3 (based on Ref. [62])

The artery model is linearized to calculate the stiffness of springs. Arteries with three tissue layers (Intima, Media, Adventitia) are considered and, starting from the stretch-energy density, some of the elasticity tensor components are calculated. The artery is discretized by a 2D mesh where the nodes are connected by three kinds of linear springs (one normal and two angular ones). The model linearizes and homogenizes the material response, but it still contemplates the geometric nonlinearity. Specifically, a linearization is performed in Section 3.2 to determine the Elasticity Tensor (ET) for each layer. Furthermore, the interaction between the nodes is simulated using normal and angular springs. Then, in Section 3.4 the stiffnesses are determined and the results are compared to the calculations performed with a nonlinear model. Finally, in Section 3.4.1 the range of validity in the linear approximation is analyzed.

- Chapter 4 (based on Ref. [63])

In this chapter, a complete system for the simulation of MIVS is described. The environment is composed of a hardware that captures the movements of the wire and an algorithm that simulates in real-time the motion inside

arteries. In Section 4.2.1 the physical model of the wire proposed by Konings is improved. As a result, a simpler and more stable method is obtained to calculate the equilibrium configuration of the wire. Then, in Section 4.2.2 the GR method is developed to perform relaxations. It is particularly useful when the wire is hindered in the Physical Relaxation (PR) method because of the boundary conditions. Also, in Section 4.2.3 a recipe is given to merge the PR and the GR methods, resulting in efficient relaxations. The hardware has a low cost and is explained in Section 4.2.4. Moreover, in Section 4.3 tests show that the shape of the virtual wire agrees well with the experiment.

Finally, in Chapter 5 the main conclusions of the previous chapters are addressed and future works are pointed out.

Chapter 2

Surfaces for Modeling Arteries

2.1 State of the Art

According to Kretschmer et al. [65], current vascular modeling methods can be roughly categorized as model-free or model-based. Model-free methods are also referred to as implicit methods, since they usually rely on generic point cloud-based interpolation techniques [66] and make extensive use of implicit indicator functions to interpolate models. Common choices for interpolation techniques include multilevel partition of unity implicits [67] and Poisson surface reconstruction [68]. Model-free methods are usually concerned with a robust extraction of point clouds from binary segmentation masks that is able to capture fine vessels. To generate reliable interpolations, these methods need a dense sampling and usually they do not incorporate explicit topological and geometric information on the underlying vasculature.

Model-based methods, in contrast, are motivated by the tubular structure of vascular systems and are frequently used to visualize centerline descriptions [65]. Many techniques rely on explicit mesh generation methods [69–71], which is usually fast but often leads to selfintersecting meshes at vascular bifurcations. For computational hemodynamics, the generated models need to be smooth and free of selfintersections or unwanted inner structures [72]. Implicit modeling provides inherent composition mechanisms to solve this problem and has been successfully used to generate model-based vascular models. The Oeltze & Preim [73] approach is based on convolution surfaces and produces closed, intersection-free models. It has, however, limited expressiveness, since it is restricted to polar definitions of cross sections. An implicit modeling technique that supports free-form shapes was proposed by Kretschmer et al. [74].

Workflows to interactively segment or correct vascular segmentations have been proposed by Diepenbrock & Ropinski [75] and by Wang et al. [76]. These semi-automatic methods, however, are bound to the resolution of the underlying dataset and allow only for an indirect manipulation of the vascular representation.

A mesh generation of image-based vascular models has been implemented by Santis et al. [77] combining two software packages: the **Vascular Modeling Toolkit** from www.vmtk.org (a software for Three-Dimensional (3D) reconstruction and geometric analysis of image-based modeling of blood vessels) and **pyFormex** from www.pyformex.org (a software for generating, transforming, and manipulating large geometrical models of 3D structures by sequences of mathematical operations). A common problem of surface mesh generation is the intersecting triangulations. Cebra et al. [78] described an algorithm for merging these triangulations in the context of FEM applied to blood flow.

Sometimes a complicated geometry is not adequate, especially at initial learning stages. Currently, there are no implementations of hands-on online learning platforms for physicians in this area, because the algorithms used are computationally expensive to simulate a real-time experience [79]. The need for such a platform inspired the development of our model-base algorithm, which generates virtual arteries using Sweep Surfaces.¹ In particular, the planar geometry of the contour

¹See a video at <https://youtu.be/MXHTxOMjNNo>

curves improves the collision-detection [80] between the tool and the artery.

2.2 Methods

2.2.1 Surfaces

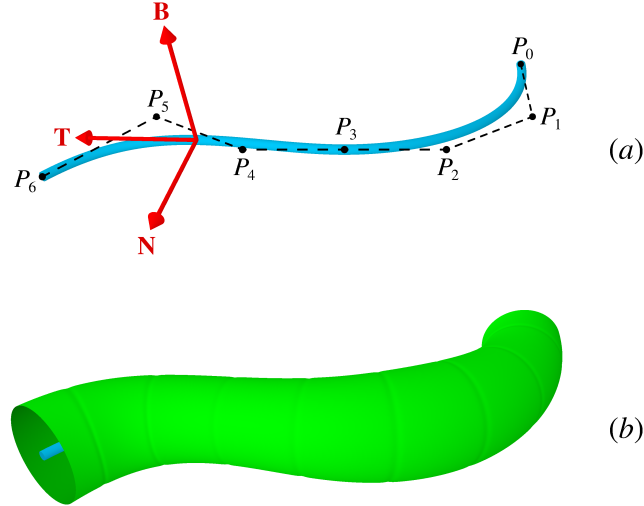


Figure 2.1: (a) A Bezier curve defined by 7 control points representing the trajectory $\alpha(t)$. The orthonormal vectors \mathbf{T} , \mathbf{N} , and \mathbf{B} are illustrated at a particular point. (b) The parametric curve $\xi_t(u)$ changes its shape smoothly. The cross section in this example is a circumference with variable radius.

Sweep surfaces have already been used for modeling vascular structures applied to blood flow simulations [65, 81]. This idea is extended to show how it can be used to generate virtual arteries suitable for simulators of MIVS.

Generating a 3D surface by sweeping a curve along a trajectory $\alpha(t)$ as in Fig. 2.1(a), consists of forward mapping a contour set $\xi_t(u)$ [82]. The general transformation describing the parametric surface can be written as the isometry

$$S(t, u) = \xi_t(u) \begin{pmatrix} \mathbf{N}(t) \\ \mathbf{B}(t) \\ \mathbf{T}(t) \end{pmatrix}_{3 \times 3} + \alpha(t)$$

where the tangent $\mathbf{T}(t)$, the normal $\mathbf{N}(t)$, and binormal $\mathbf{B}(t)$ are the vectors in the Frenet-Serret frame [83]. To simplify the equations and to introduce a planar segmentation, we use 2D curves $\xi_t(u) = (x_t(u), y_t(u))$, *i.e.* with $z_t(u) = 0$. Then

the Sweep Surface becomes (Fig. 2.1(b))

$$S(t, u) = (x_t(u), y_t(u)) \begin{pmatrix} \mathbf{N}(t) \\ \mathbf{B}(t) \end{pmatrix}_{2 \times 3} + \boldsymbol{\alpha}(t) \quad (2.1)$$

Sometimes, it is convenient to rotate the normal and binormal vectors in order to adjust the curves close to the bifurcation. The 2D planar curves are discretized by polylines with N_v vertices. The topology of the inner surface, where the interaction with the catheter takes place, is defined by a triangularization [84].

It is possible to connect arteries through “T” or “Y” bifurcations, preserving planar polylines in the intersection. Some vertices of the polylines are removed and additional planes are required to decide in which artery the catheter is located (see Fig. 2.2 for details). To avoid holes in the connection of consecutive segments, all polylines must have the same number of vertices.

The idea of planar surfaces can be extended to real objects (Fig. 2.3). This can be done by defining planes intersecting the real model and constructing a polyline which fits the cross section by means of a least square procedure. Finally, note that the resolution in the intersection region depends solely on N_v , which must be a multiple of 4. Specifically, the number of Surface Elements (SE) equals N_v^2 and $\frac{3}{4}N_v^2$ in a T-like and in a Y-like bifurcation respectively.

In a VRS the collision-detection must be carried out between the catheter and the inner surface of the artery [85]. In principle, a simple algorithm checks if an intersection occurs between each segment of the catheter (a large number) and the triangles that mold the surface and represent the discretization of the artery wall (a huge number).

The collision search task is time-consuming and an efficient approach is to use the idea of boundary boxes [86]. In our case these become segment boxes and take advantage of the Sweep Surface geometry. Each segment box is bounded by two consecutive planar sections and the search is restricted to those triangular SE inside the segment.

A further improvement can be made by dividing each *cylindrical* segment into subsegments as slices of a cake (Fig. 2.4(a)). We take the number of subsegments to be equal to the number N_v of polyline vertices. Then the number N_s of SE per subsegment is approximately constant.

Making additional subdivisions (Fig. 2.4(b)) reduces the collision-detection calculation still further. Close to the border of the slices of a cake we insert a cutting plane (blue line), so that if the catheter is inside the white or light green region no collision-detection needs to be performed. Hence, by including a single additional step we can avoid testing the collision-detection with the SE, which are approximately five in number as observed in numerical simulations.

A straightforward procedure to find a cutting plane is as follows. Let $\mathbf{S}_1, \dots, \mathbf{S}_m$ be the vector areas of the SE (triangles) within the subsegment. First calculate $\mathbf{n}S = \mathbf{S}_1 + \dots + \mathbf{S}_m$, where S represents the modulus of the sum and \mathbf{n} is a unit vector. The normal \mathbf{n} points in the average direction of the triangles vector area.

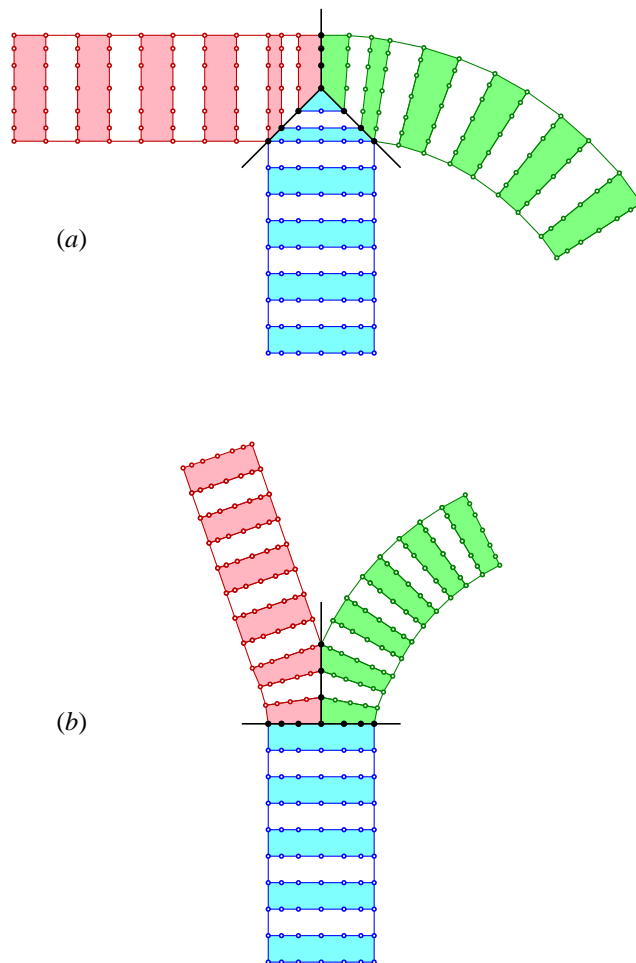


Figure 2.2: Top view of connected arteries having polylines with the same number of vertices (open points). The 3D segments are represented by white and light colored areas separated by planar polylines. When two planes intersect some vertices are removed and the truncated polylines have two vertices in common: one at the top (black point) and one at the bottom (not shown). The shape of the arteries is arbitrary, since the only requirement is that the black point remains in the line given by the intersection of the two planes. The black lines represent additional planes that split the volume between adjacent arteries. We show in (a) a *T*-like bifurcation and in (b) a *Y*-like bifurcation.

Further, if $\mathbf{r}_{1a}, \mathbf{r}_{1b}, \mathbf{r}_{1c}, \dots, \mathbf{r}_{ma}, \mathbf{r}_{mb}, \mathbf{r}_{mc}$ are the vertices of the triangles, test which one gives the smallest dot product $\mathbf{n} \cdot \mathbf{r}_{ix}$ and label it as \mathbf{r}_{\min} . An equation for the cutting plane is $\mathbf{n} \cdot (\mathbf{r} - \mathbf{r}_{\min}) = 0$, since all triangles will be on the upper side of this plane.

To decide which SE the catheter joint intercepts, it is necessary to have additional planes (black lines in Fig. 2.4) dividing the volume between adjacent triangles, *i.e.*

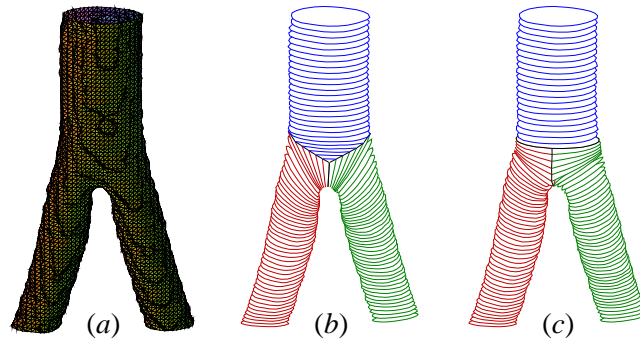


Figure 2.3: (a) Image from a bifurcation of the Abdominal Aorta into the Common Iliac Arteries. The image was extracted using the *Vascular Modeling Toolkit* software, which can also determine the central line $\alpha(t)$ (not shown). Virtual representation using planar polylines (b) in a T-like bifurcation and (c) in a Y-like bifurcation. Although both bifurcation styles can be applied, in this case the Y-like bifurcation looks more natural. For simplicity, the resolution is low with $N_v = 24$ vertices, and the triangularization is not displayed in order to make the Figure clear.

to build volume boxes similar to a triangular prism. We label this plane as *lateral plane* and it will be used in the calculation of the interaction force (Section 2.2.2).

Consider two vertices A and B common to the pair of triangles. The lateral plane goes through the vertices A , B , and has a normal vector $\hat{\mathbf{t}}_{AB}$. A natural definition for $\hat{\mathbf{t}}_{AB}$ is to take it parallel to the vector $(\mathbf{r}_A - \mathbf{r}_B) \times (\hat{\mathbf{n}}_A + \hat{\mathbf{n}}_B)$, where \mathbf{r}_i represents the position of the vertice and $\hat{\mathbf{n}}_i$ the surface normal. In this way $\hat{\mathbf{t}}_{AB}$ is perpendicular to the line joining A , B , and also to the average normal vector at these vertices. However, when A and B are in the same planar polyline, the vector $\hat{\mathbf{t}}_{AB}$ is the normal vector of the plane containing the polyline.

The video at https://youtu.be/q51hvXNd_Xg shows how the sections are created.

2.2.2 Catheter-Surface Interaction

A critical point in simulations is how the catheter interacts with the artery, since the finely tuned details will decide the way the catheter propagates in bifurcations, which is the significant part of the learning process [87].

We suppose that the catheter has intercepted a triangular SE with vertices ABC and we proceed to calculate the force \mathbf{F}_{ABC} acting on this surface.

At the A -th vertice we define the vector $\mathbf{k}_A = k_{\text{eq}A} \hat{\mathbf{n}}_A$, whose modulus $k_{\text{eq}A}$ represents the equivalent stiffness of the springs holding the vertice to the equilibrium position. The force associated with A reads

$$\mathbf{F}_A = s\mathbf{k}_A \tag{2.2a}$$

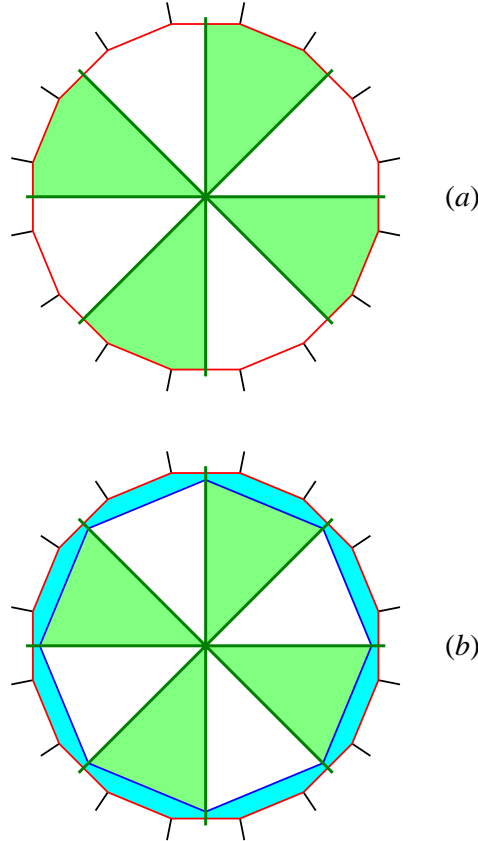


Figure 2.4: Cross section in the middle of a segment i.e. between two planar poly-lines. In this example each polyline has $N_v = 8$ vertices and there are $2N_v = 16$ triangular SE (red lines) defining the topology of the artery segment. Additional lateral planes (black lines) are used to divide the volume outside the artery between adjacent SE. Notice that the planes represented by lines are not perpendicular to the Figure but are inclined. (a) Cross section of an artery segment divided as slices of a cake (green lines). In practice the division need not be symmetric. (b) Further subdivision using a single additional plane per subsegment (blue lines).

where s stands for the distance between the joint and the SE.

Denoting by \mathbf{x} the joint position, we associate the following force with the line connecting A and B (Fig. 2.5(a))

$$\mathbf{F}_{AB} = \frac{d_B \mathbf{F}_A + d_A \mathbf{F}_B}{d_A + d_B} \quad (2.2b)$$

where $d_A = \sqrt{(\mathbf{x} - \mathbf{r}_A)^2 - [\hat{\mathbf{m}}_A \cdot (\mathbf{x} - \mathbf{r}_A)]^2}$ is the distance to the line going through A and parallel to the unit vector $\hat{\mathbf{m}}_A$, which points in the direction of $\hat{\mathbf{t}}_{AB} \times \hat{\mathbf{t}}_{CA}$.

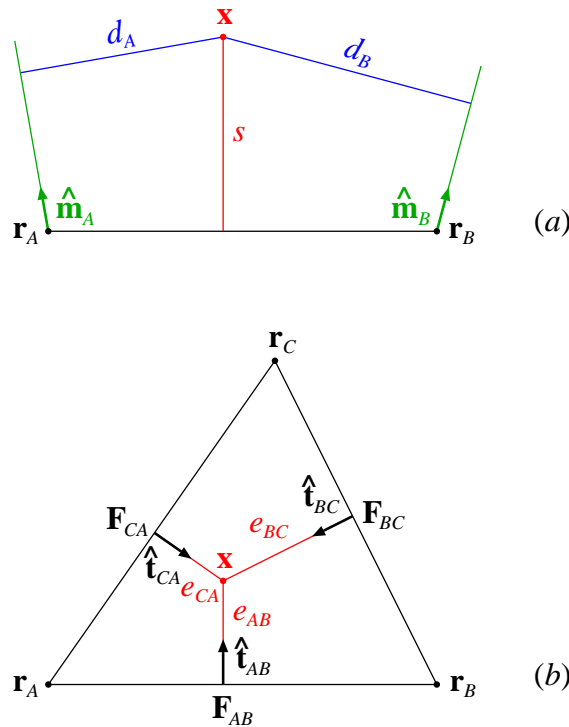


Figure 2.5: (a) Side view of the catheter joint at position \mathbf{x} between two vertices at \mathbf{r}_A , \mathbf{r}_B . The green lines go through A , B , and are parallel to the unit vectors $\hat{\mathbf{m}}_A$, $\hat{\mathbf{m}}_B$, respectively. The vectors \mathbf{x} , $\hat{\mathbf{m}}_A$, and $\hat{\mathbf{m}}_B$ are not in the plane of the Figure. (b) Top view of the joint over a triangular SE. The unit vectors $\hat{\mathbf{t}}_{ij}$ are not in the plane of the Figure, and the vectors \mathbf{F}_{ij} are not perpendicular to the plane of the Figure.

The resulting force acting on the SE is defined to be (Fig. 2.5(b))

$$\mathbf{F}_{ABC} = \frac{e_{AB} e_{CA} \mathbf{F}_{BC} + e_{BC} e_{AB} \mathbf{F}_{CA} + e_{CA} e_{BC} \mathbf{F}_{AB}}{e_{AB} e_{CA} + e_{BC} e_{AB} + e_{CA} e_{BC}} \quad (2.2c)$$

where $e_{AB} = \hat{\mathbf{t}}_{AB} \cdot (\mathbf{x} - \mathbf{r}_A) = \hat{\mathbf{t}}_{AB} \cdot (\mathbf{x} - \mathbf{r}_B)$ is the distance to the lateral plane.

The *weight* of \mathbf{F}_A in the calculation of \mathbf{F}_{AB} is inversely proportional to d_A , and for $d_A \rightarrow 0$ we get $\mathbf{F}_{AB} \rightarrow \mathbf{F}_A$. Similarly, the *weight* of \mathbf{F}_{AB} in the calculation of \mathbf{F}_{ABC} is inversely proportional to the distance e_{AB} , and for $e_{AB} \rightarrow 0$ we get $\mathbf{F}_{ABC} \rightarrow \mathbf{F}_{AB}$.

Lastly, according to Newton's third law the reaction force of the surface \mathbf{F}_{surf} equals minus the force $-\mathbf{F}_{ABC}$ exerted by the catheter. Since the force is related to the potential energy by $\mathbf{F}_{\text{surf}} = -\nabla U_{\text{surf}}$, the gradient of the surface energy coincides with \mathbf{F}_{ABC} . This gradient is used to determine the wire behaviour (see Section 4.2).

2.3 Technical Evaluation

Initially, the steps to calculate the force in a collision are examined. The recipe used in the collision-detection algorithm has the following steps. For each catheter joint perform the operations described below (Fig. 2.6):

1. Identify the artery segment where the joint is located. As the catheter is pushed into or removed from the vessel, the position of the joint changes along the artery. Thus, the first step is to verify if the joint remains in the segment, moves forward, or recedes. The search starts from the last known location and since this operation is repeated with a high frequency in comparison with the *speed* of the catheter, most of the time the joint will remain in the same segment.

The total wire length can be changed introducing or removing catheter segments close to the end instead of the beginning. In this way, the transition probability of a joint between adjacent artery segments becomes even smaller, since it does not change the position of the joints up to the beginning. However, decreasing the separation between planar polylines (*i.e.* increasing the resolution of the artery in the axial direction) increases the transition probability.

2. Search for the subsegment where the joint is located (slice of the cake in Fig. 2.4(a)). The subsegments are periodically ordered and the search is performed examining on which side of the green planes the joint is situated. As in step 1, most of the time the subsegment location will not change and this step usually reduces to test if the joint remains in the same subsegment. Thus, choosing a larger number of divisions (subsegments) does not affect the PT.
3. Test if the joint is in the inner side of the subsegment (white or light green regions in Fig. 2.4(b)). This check is easy to perform and in affirmative case there can be no collision, so that the calculation stops here. Since the inner volume is much larger than the outer volume (cyan region in Fig. 2.4(b)), this will be the result unless the joint is very close to the surface. The cyan region decreases when the number of vertices increases.
4. Test the collision of the joint with some triangular SE. This requires to verify if the joint crosses the plane defined by the triangle. Moreover, we must check the position within the volume enclosed by the *triangular prism* (Section 2.2.1). If the result is negative all SE within this subsegment must be tested. Furthermore, when a collision occurred previously, the new search starts from the last SE where the collision was detected.

Note that variations of the average N_s affect the PT, since a larger number means that more collision tests must be performed. We remark that increasing N_v and the number of subdivisions by the same amount can result in tiny variations of N_s . This happens because the surfaces are usually not right circular cylinders and the SE are triangles with variable shape. Hence, the PT

does not become appreciably larger using a higher resolution in the tangential direction.

5. Reaching this step means that a collision occurred and we have identified the triangular SE. Then proceed to calculate the reaction force on the SE (linear approximation) as described in Section 2.2.2.

The calculation of the force takes longer than testing all collisions in a subsegment (step 4) with a negative result. Changing the resolution modifies the geometry on a small scale. As a consequence, the contact points between the catheter and the surface will not be exactly the same. Thus, the collision number varies slightly with the resolution.

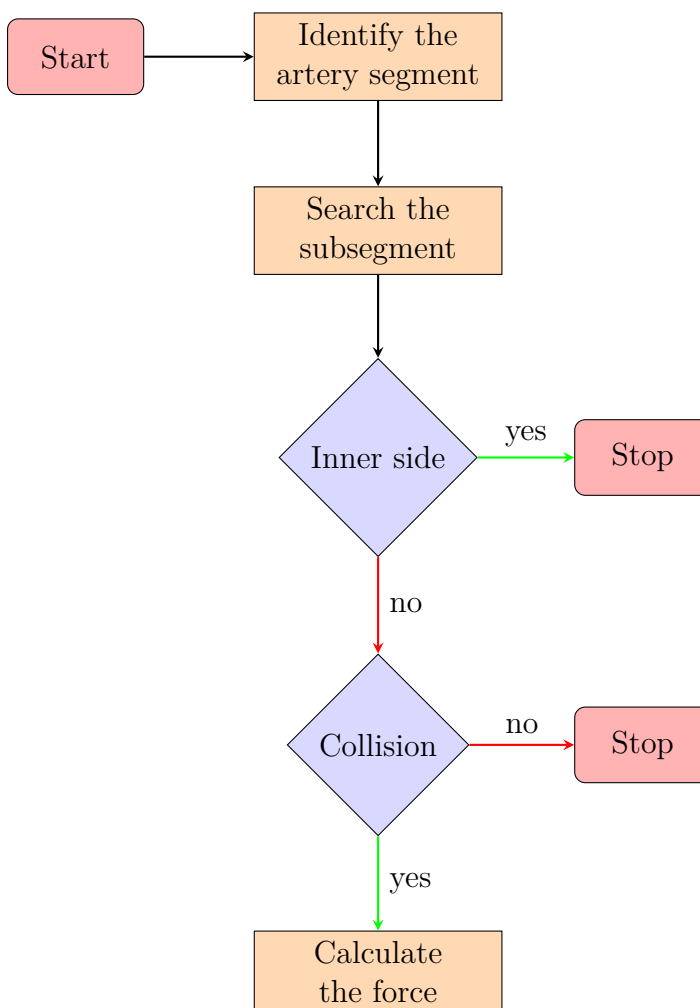


Figure 2.6: Workflow of steps 1–5 to calculate the force \mathbf{F}_{ABC} between the wire and the artery wall.

In CA simulations, most of the PT is spent in determining the interaction between the catheter and the surface [88]. The recipe above constitutes an efficient method

to perform this calculation. The PT does not increase appreciably using a higher artery resolution in the axial and/or tangential directions.

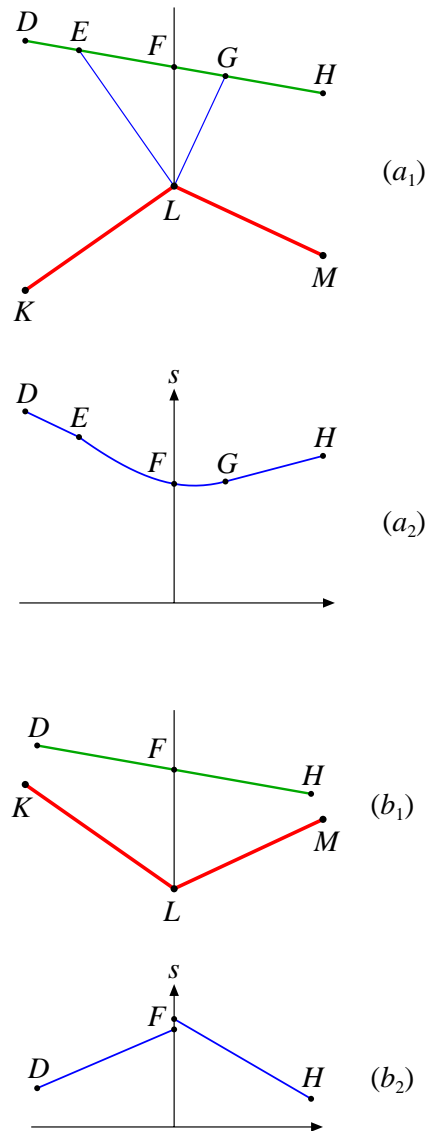


Figure 2.7: (a₁) Concave intersection KLM . As a point moves along the line $DEFGH$, the distance s to the planes KL and LM (perpendicular to the Figure) varies continuously as shown in (a₂). (b₁) Convex intersection KLM . As a point moves along the line DFH , the distance s to the planes KL and LM has the dependence shown in (b₂), which is not continuous at point F .

The force vector field defined in Section 2.2.2 is a continuous function of the position. Further, consider a lateral plane (line LF in Fig. 2.7) dividing two adjacent triangular regions. In a convex surface as in (a₁), the field is continuous at LF (point F in (b₂)), since for $e_{AB} \rightarrow 0$ the value is equal to \mathbf{F}_{AB} on both sides. For that

reason, no instabilities appear when the joint moves across the lateral plane. But in a nonconvex surface, as can happen for example in the bifurcation of arteries, the modulus of the field is discontinuous. The minimum distance s to the SE has a jump across the lateral plane (point F in (b_2)) and \mathbf{F}_{AB} differs on both sides. However, in the special case that the angles $\angle FLK$ and $\angle FLM$ are equal, s is continuous at F .

Close to equilibrium, the catheter joints which are not tightly bound to the surface bounce in and out by a small amount (a numerical artifact). When the joint leaves the surface, the repelling force instantaneously becomes zero and the joint moves back. Therefore, including dissipative forces in the calculations improves convergence [89].

2.4 Software

In order to model the sweep surfaces, a system was developed in C++ that uses the OpenGL² graphic library [90] and the GLUT user interface library.³

In the main window of the modeler, it is possible to add and to edit the parameters of the central line, to change the perspective, and to chose the objects to be visualized (Fig. 2.8). Specifically, the main controls are:

Segment - Add or delete a new segment of the central line. It can be connected with a T- or Y-like bifurcation.

Control Point - Edit the control points of the central line.

Model Rotation - Rotate the tubular or the bifurcation surface around the first control point.

Real movements - Change the position and scale of the real model.

Show - Specify how each object must appear.

Two auxiliary windows work in connection with the main window (Fig. 2.9). They are used to edit the planar curves of the sweep and of the bifurcation surfaces. Any change in the auxiliary windows is immediately updated in the main window. This ensure the correct visualization in the artery model.

The most relevant controls of the Builder of Sections window are:

Scale/Rotation - Change the scale and rotation of the curve around the central point (green in Fig. 2.9).

Position - Change the position of the planar curve over the central line. It varies from 0 to 1, which corresponds to the beginning and to the end of the central line respectively.

Curves selection - Select the active planar curve.

New curve 2D/Del - Add or delete a planar curve.

Orientation - Change the orientation of the polyline (clockwise or counterclockwise).

²Open Graphics Library www.opengl.org

³GLUT-based www.glui.sourceforge.net

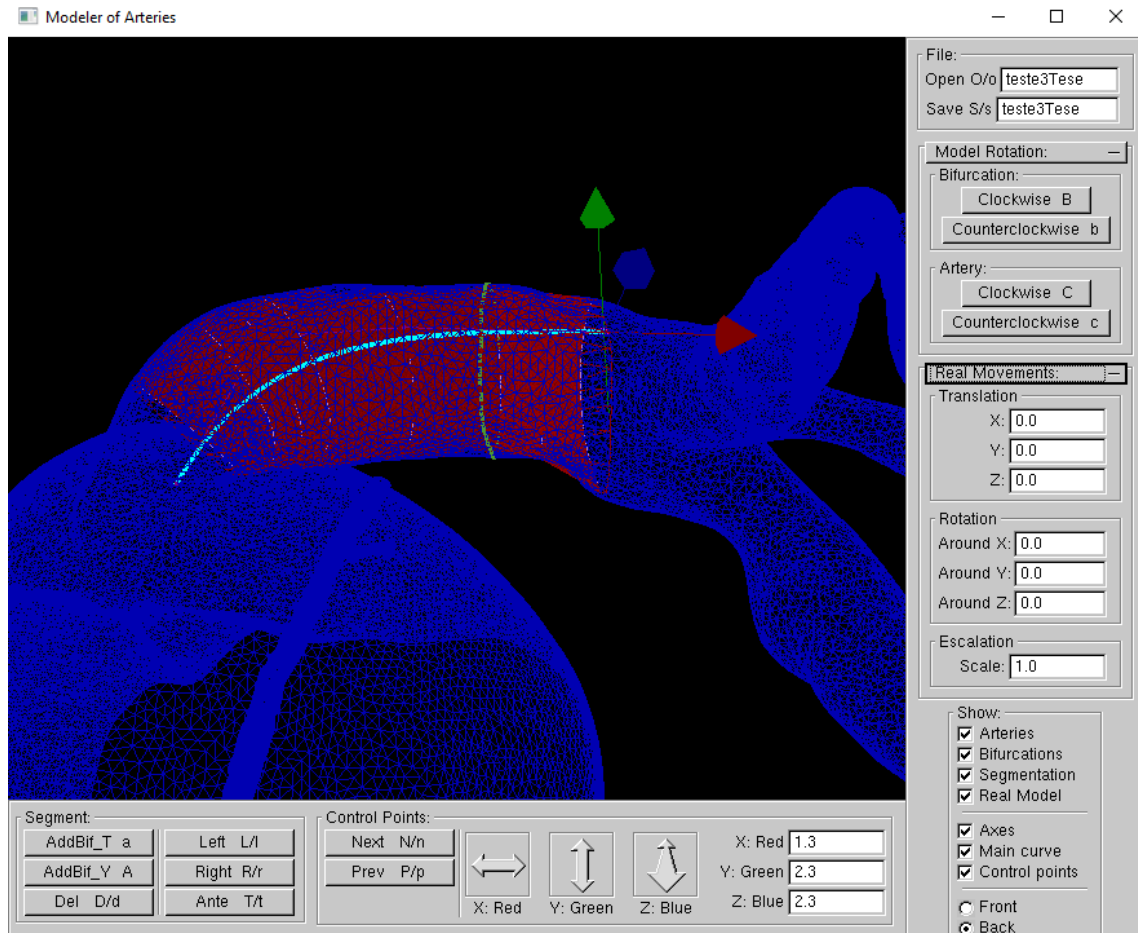


Figure 2.8: Main window of the *Modeler* software. The sweep surface in red is built over a real model of coronaries in blue (kindly yielded by LNCC www.lncc.br). The central line is a Bezier curve (cyan) with 4 control points.

Adj. Act/All Sec - Merge the planar curve in the real model.

The most relevant controls of the *Builder of Bifurcations* window are:

Surface - Chose the part of the bifurcation.

Curve - Chose the planar curve.

Separ - Select the distance between the adjacent central lines.

Adj. Act/All Sec - Merge the planar curve in the real model.

Once the central line is positioned inside of the real model, moving the 4 control points of the Bezier curve automatically fits all the planar sections. A similar procedure is performed at the bifurcation.

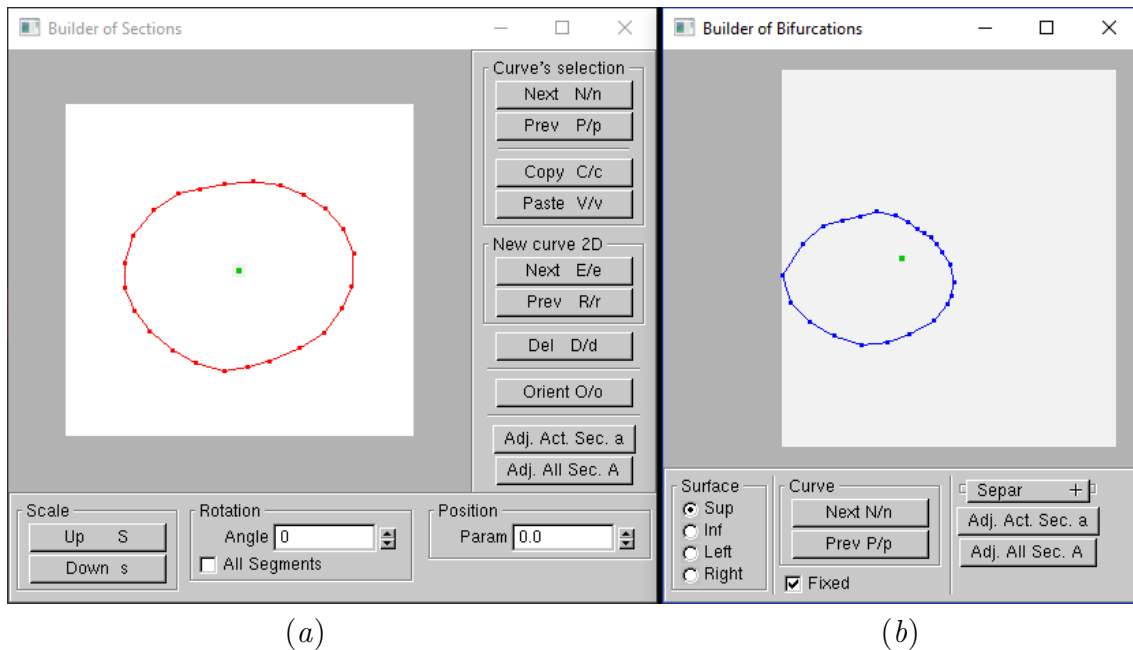


Figure 2.9: (a) “Builder of Sections” auxiliary window. Here it is possible to edit the planar curves which are swept over the main curve. (b) “Builder of Bifurcations” auxiliary window. In this window, the planar curves from the bifurcations are edited. The green point in both windows represents the intersection of the central line and the plane which contains the planar curves.

2.5 Conclusions

An intuitive way to create the geometry of an artery using the sweep technique was proposed, which can be extended to bifurcations. The method only requires to define the trajectory and the cross section with planar polylines. Then it quickly determines the topology of the inner surface. Furthermore, this procedure can also be applied to model arteries with real data.

The most time-consuming task in catheter simulations is the calculation of interactions with the surface. The use of planar surfaces in the segmentation simplifies the collision-detection algorithm. The idea of boundary boxes is key to create a simple and efficient method. A procedure has been introduced to create a smart volume partition of the arteries. The artery resolution can be increased and it does not affect the PT significantly.

A thorough recipe to calculate the gradient of the surface energy representing the interaction with the catheter was given. The resulting force field is a continuous function of position, except under special circumstances at bifurcations. This vector field is a milestone for the development of a catheter simulator.

Chapter 3

Approximate Artery Elasticity

3.1 State of the Art

According to Diez [91], physiological and pathological changes in the cardiovascular system directly influence the mechanical behaviour of arterial walls. With age, the normal wall stress is associated with a larger diameter and a stiffer material of the arteries (arteriosclerosis), which results in increased pulse-wave velocity and disproportionate increase in pressure [92]. It is, therefore, of crucial importance to improve the understanding of the mechanical properties of the constituents of arterial walls, including the inherent features of anisotropy and nonlinearity [93]. These properties pose formidable challenges in the constitutive modelling and numerical analysis of such tissues, and they can be clearly connected to the underlying structure of the tissues [94].

The passive mechanical behaviour of an arterial wall is governed mainly by the matrix material (which consists of water, elastin, and proteoglycans [95]) and the collagen fibre reinforcement [96]. The anisotropy is associated with the local mean alignment of the collagen fibres which stiffen their response under tension [97], leading to significant nonlinear characteristics. The fibres are not perfectly aligned but are dispersed around a mean direction [98]. The amount and character of the dispersion depends on the topography, the particular layer of the vessel considered, and the respective (patho)physiological condition, *inter alia*. Fibre dispersion and structural quantification of collagen in arterial walls has been documented and analysed, for example, in Refs. [99–103].

An overview of the main existing continuum mechanical models was provided by Holzapfel et al. [93]. Classical continuum mechanics assumes that the constitutive models and the corresponding simulations start from an unloaded, stress-free reference configuration [104]. This has been used to calculate the amount of stress applied to the tissue and its associated strain response [105–108]. Other models try to approximate the behavior by splitting the strain-energy function into an isotropic part for elastin and an anisotropic part for collagen [109, 110]. Collagen exhibits high non-linear behavior bearing the major part of the load transmitted through the tissue, while elastin has important flexibility and extensibility features for blood vessels [111].

Hill et al. [112] presented a new combined constitutive model in which fiber recruitment begins at a finite strain with activation stretch represented by a probability distribution function. By directly including this recruitment data, the collagen contribution was modeled using a simple Neo-Hookean equation [113]. As a result, only two phenomenological material constants were required to fit the stress-stretch data.

A nonlinear artery model has been proposed by Holzapfel et al. [48], which is well suited for numerical realization using FEM [114]. Due to its strong mathematical background, the FEM is physically more accurate than most methods [115, 116]. Linear FEM is the most popular technique to model tissue deformation in VRS [117]. However, it is a time-consuming process and can not support real time simulations unless some approximations are done. For instance, in the Condensation Method

only the displacements in the vicinity of the surgical instrument are calculated [118]. The simulation is restricted to specific tasks and regions, while the rest of the scene remains a static mesh.

An alternative approach to the FEM is the Mass-Spring Method, which uses springs to connect the nodes of the mesh [119–122]. In comparison to the FEM, it is relatively easy to simulate the soft tissue deformation [123]. Nevertheless, the outcomes depend on the springs stiffnesses and the determination of the stiffnesses is not a straightforward task [124].

In this chapter, a 2D mesh to calculate artery deformations is proposed. Therefore, the numerical difficulties arising from the isochoric constrain in 3D are avoided. The number of points in the FEM is substantially reduced and the calculations become simpler.

3.2 Methods

When accuracy is not the most relevant aspect and a real time response is required as in VRS, reduced mesh size and linearization increase the computing performance [125]. The method in this work is equivalent to a FEM using few mesh points. First, some ET components are determined and, afterwards, the stiffness of the springs connecting the nodes are calculated.

3.2.1 Elasticity Tensor

Any model used to describe tissues must be populated with data which are difficult to acquire *in vivo* [126]. It is not our purpose to develop a new artery prototype but to simplify the model of previous works. Our main interest is in tangential, axial, and radial deformations, so shear stretches will not be considered. Holzapfel et al. [127] have modeled each arterial layer \mathbf{t} with the following energy density function

$$\Psi_{\mathbf{t}} = \mu_{\mathbf{t}}(I_1 - 3) + \frac{k_{1\mathbf{t}}}{k_{2\mathbf{t}}}(\Gamma_{\mathbf{t}} - 1) \quad (3.1)$$

with

$$\Gamma_{\mathbf{t}} = e^{k_{2\mathbf{t}}[(1-\rho_{\mathbf{t}})(I_1-3)^2 + \rho_{\mathbf{t}}(I_{4\mathbf{t}}-1)^2]} \quad (3.2)$$

The invariants I_1 , $I_{4\mathbf{t}}$ are defined by

$$\begin{aligned} I_1 &= \Lambda_{r+\theta+z} \\ I_{4\mathbf{t}} &= \Phi_{\theta\mathbf{t}} + \Phi_{z\mathbf{t}} \end{aligned} \quad (3.3)$$

where

$$\begin{aligned}
 \Lambda_{\ell r + m\theta + nz} &= \ell\lambda_r^2 + m\lambda_\theta^2 + n\lambda_z^2 \\
 \Phi_{\theta\mathbf{t}} &= \lambda_\theta^2 \cos^2 \phi_{\mathbf{t}} \\
 \Phi_{z\mathbf{t}} &= \lambda_z^2 \sin^2 \phi_{\mathbf{t}}
 \end{aligned}
 \tag{3.4}$$

and ℓ, m, n represent integers. For example, $\Lambda_{r+\theta+z} = \lambda_r^2 + \lambda_\theta^2 + \lambda_z^2$, $\Lambda_{\theta-r} = \lambda_\theta^2 - \lambda_r^2$, and $\Lambda_{z+r} = \lambda_z^2 + \lambda_r^2$. The physical parameters of the layers $\mu_{\mathbf{t}}$, $k_{1\mathbf{t}}$, $k_{2\mathbf{t}}$, $\rho_{\mathbf{t}}$, $\phi_{\mathbf{t}}$ were experimentally obtained from the coronaries of human cadavers (Table 3.1).

Table 3.1: Average physical parameters from Holzapfel et al. [127] for the Intima (i), Media (m), and Adventitia (a) tissues. The thickness $a_{\mathbf{t}}$ is in mm, $\mu_{\mathbf{t}}$ and $k_{1\mathbf{t}}$ are in kPa, $k_{2\mathbf{t}}$ and $\rho_{\mathbf{t}}$ are dimensionless, and the angle $\phi_{\mathbf{t}}$ is in degrees.

\mathbf{t}	$a_{\mathbf{t}}$	$\mu_{\mathbf{t}}$	$k_{1\mathbf{t}}$	$k_{2\mathbf{t}}$	$\rho_{\mathbf{t}}$	$\phi_{\mathbf{t}}$
i	0.24	27.90	263.66	170.88	0.51	60.3
m	0.32	1.27	21.60	8.21	0.25	20.61
a	0.34	7.56	38.57	85.03	0.55	67.0

Soft tissues, composed of collagen fibers with a considerable amount of water, can be modeled as quasi-incompressible [128]. Their volumes do not change within the physiological range of interest, so that

$$\lambda_r \lambda_\theta \lambda_z = 1 \tag{3.5}$$

Hence, the radial stretch λ_r depends on the tangential stretch λ_θ and on the axial stretch λ_z . Furthermore, the stresses in the circumferential and axial directions are functions of λ_θ and λ_z

$$\begin{aligned}
 \sigma_{\theta\theta\mathbf{t}} &= \lambda_\theta \frac{\partial \Psi_{\mathbf{t}}}{\partial \lambda_\theta} \\
 \sigma_{zz\mathbf{t}} &= \lambda_z \frac{\partial \Psi_{\mathbf{t}}}{\partial \lambda_z}
 \end{aligned}
 \tag{3.6}$$

Several calculations in artery mechanics are inherently large deformation problems. However, our interest is in small deformations and a linearization is carried out in order to obtain the incremental elasticity constants. By expanding (3.6) in a Taylor series up to the first order

$$\begin{aligned}
 \sigma_{\theta\theta\mathbf{t}} &= \sigma_{\theta\theta\mathbf{t}0} + C_{\theta\theta\theta\mathbf{t}} \varepsilon_{\theta\theta} + C_{\theta\theta zz\mathbf{t}} \varepsilon_{zz} \\
 \sigma_{zz\mathbf{t}} &= \sigma_{zz\mathbf{t}0} + C_{\theta\theta zz\mathbf{t}} \varepsilon_{\theta\theta} + C_{zzzz\mathbf{t}} \varepsilon_{zz}
 \end{aligned}
 \tag{3.7}$$

where $c_{\theta\theta\theta\mathbf{t}}$, $c_{zzzz\mathbf{t}}$, $c_{\theta\theta zz\mathbf{t}}$ are ET components,

$$\begin{aligned}\varepsilon_{\theta\theta} &= \ln(\lambda_\theta/\lambda_{\theta 0}) \\ \varepsilon_{zz} &= \ln(\lambda_z/\lambda_{z0})\end{aligned}\quad (3.8)$$

are strains, and $\lambda_{\theta 0}$, λ_{z0} are the circumferential and axial stretches in the average blood pressure $\bar{p}_{\mathbf{in}}$.

It is convenient to define

$$\begin{aligned}P_{\theta\mathbf{t}} &= (1 - \rho_{\mathbf{t}})(I_1 - 3)\Lambda_{\theta-r} + \rho_{\mathbf{t}}(I_{4\mathbf{t}} - 1)\Phi_{\theta\mathbf{t}} \\ P_{z\mathbf{t}} &= (1 - \rho_{\mathbf{t}})(I_1 - 3)\Lambda_{z-r} + \rho_{\mathbf{t}}(I_{4\mathbf{t}} - 1)\Phi_{z\mathbf{t}} \\ Q_{\theta\theta\mathbf{t}} &= (1 - \rho_{\mathbf{t}})\left[(I_1 - 3)\Lambda_{\theta+r} + \Lambda_{\theta-r}^2\right] + \rho_{\mathbf{t}}(I_{4\mathbf{t}} - 1 + \Phi_{\theta\mathbf{t}})\Phi_{\theta\mathbf{t}} \\ Q_{zz\mathbf{t}} &= (1 - \rho_{\mathbf{t}})\left[(I_1 - 3)\Lambda_{z+r} + \Lambda_{z-r}^2\right] + \rho_{\mathbf{t}}(I_{4\mathbf{t}} - 1 + \Phi_{z\mathbf{t}})\Phi_{z\mathbf{t}} \\ Q_{\theta z\mathbf{t}} &= (1 - \rho_{\mathbf{t}})\left[(I_1 - 3)\Lambda_r + \Lambda_{\theta-r}\Lambda_{z-r}\right] + \rho_{\mathbf{t}}\Phi_{\theta\mathbf{t}}\Phi_{z\mathbf{t}}\end{aligned}\quad (3.9)$$

Then the stresses at average blood pressure are explicitly

$$\begin{aligned}\sigma_{\theta\theta\mathbf{t}0} &= 2\mu_{\mathbf{t}}\Lambda_{\theta-r} + 4k_{1\mathbf{t}}P_{\theta\mathbf{t}}\Gamma_{\mathbf{t}} \\ \sigma_{zz\mathbf{t}0} &= 2\mu_{\mathbf{t}}\Lambda_{z-r} + 4k_{1\mathbf{t}}P_{z\mathbf{t}}\Gamma_{\mathbf{t}}\end{aligned}\quad (3.10)$$

and the ET components in (3.7) are calculated with the formulas

$$\begin{aligned}c_{\theta\theta\theta\mathbf{t}} &= 4\mu_{\mathbf{t}}\Lambda_{\theta+r} + 8k_{1\mathbf{t}}Q_{\theta\theta\mathbf{t}}\Gamma_{\mathbf{t}} + 16k_{1\mathbf{t}}k_{2\mathbf{t}}P_{\theta\mathbf{t}}^2\Gamma_{\mathbf{t}} \\ c_{zzzz\mathbf{t}} &= 4\mu_{\mathbf{t}}\Lambda_{z+r} + 8k_{1\mathbf{t}}Q_{zz\mathbf{t}}\Gamma_{\mathbf{t}} + 16k_{1\mathbf{t}}k_{2\mathbf{t}}P_{z\mathbf{t}}^2\Gamma_{\mathbf{t}} \\ c_{\theta\theta zz\mathbf{t}} &= 4\mu_{\mathbf{t}}\Lambda_r + 8k_{1\mathbf{t}}Q_{\theta z\mathbf{t}}\Gamma_{\mathbf{t}} + 16k_{1\mathbf{t}}k_{2\mathbf{t}}P_{\theta\mathbf{t}}P_{z\mathbf{t}}\Gamma_{\mathbf{t}}\end{aligned}\quad (3.11)$$

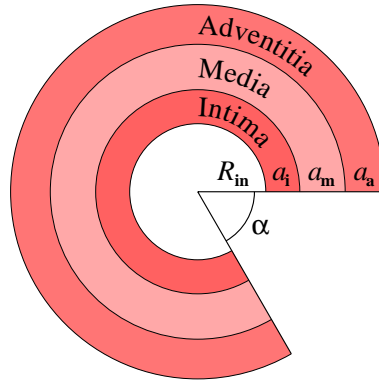


Figure 3.1: *Cross view of the arterial ring in the stress-free reference configuration (not to scale, see Fig. 1.4). The geometrical parameters are the inner radius $R_{\mathbf{in}}$, the tissue thicknesses $a_{\mathbf{i}}$, $a_{\mathbf{m}}$, $a_{\mathbf{a}}$, and the opening angle α .*

For simplicity, a cylindrical artery is considered. The inner radius is $R_{\mathbf{in}}$ and the

thicknesses of the Intima \mathbf{i} , Media \mathbf{m} , and Adventitia \mathbf{a} tissues are $a_{\mathbf{i}}$, $a_{\mathbf{m}}$, and $a_{\mathbf{a}}$ respectively (Fig. 3.1). After applying an internal pressure or stretching axially the artery, the geometry changes [128].

Because the tissues are incompressible [129, 130], the circumferential stretch has the following dependence on the radius r

$$\lambda_{\theta} = \frac{kr}{R} = \frac{kr}{\sqrt{R_{\mathbf{in}}^2 + k\lambda_z(r^2 - r_1^2)}} \quad (3.12)$$

where $k = 2\pi/(2\pi - \alpha)$ and $r_1 = \lambda_{\theta\mathbf{in}}R_{\mathbf{in}}/k$ is the inner radius in the deformed configuration (with internal pressure $p_{\mathbf{in}}$). Furthermore, α represents the opening angle (Fig. 3.1) and $\lambda_{\theta\mathbf{in}}$ represents the circumferential stretch at the inner surface. Particularly, the volume average is

$$\bar{\lambda}_{\theta} = \frac{1}{\lambda_z(r_2^2 - r_1^2)} \left[r_2 R_{\mathbf{a}} - r_1 R_{\mathbf{in}} + \frac{k\lambda_z r_1^2 - R_{\mathbf{in}}^2}{\sqrt{k\lambda_z}} \ln \left(\frac{\sqrt{k\lambda_z} r_2 + R_{\mathbf{a}}}{\sqrt{k\lambda_z} r_1 + R_{\mathbf{in}}} \right) \right] \quad (3.13)$$

where $R_{\mathbf{a}} = R_{\mathbf{in}} + a_{\mathbf{i}} + a_{\mathbf{m}} + a_{\mathbf{a}}$ and $r_2 = \Upsilon(R_{\mathbf{a}})$, the function Υ being defined by

$$\Upsilon(R) = \sqrt{r_1^2 + \frac{R^2 - R_{\mathbf{in}}^2}{k\lambda_z}} \quad (3.14)$$

When the cylindrical artery is subjected to the internal pressure, the deformation and the stress are axially symmetric. The equilibrium stress without external body forces satisfies the following differential equation [131]

$$\frac{d\sigma_{rr}}{dr} + \frac{\sigma_{rr} - \sigma_{\theta\theta}}{r} = 0 \quad (3.15)$$

The boundary condition at the inner surface is $\sigma_{rr}(r_1) = -p_{\mathbf{in}}$ and (3.15) can be integrated numerically to determine $\sigma_{rr}(r)$. However, the value of $\lambda_{\theta\mathbf{in}}$ is not yet known and it is chosen such that $\sigma_{rr}(r_2) = 0$ results. Physically, this condition is equivalent to a zero traction at the external surface [132].

3.2.2 Spring Stiffness

To simulate the physical properties of the tissues, the interaction between the nodes located at the inner surface of the Intima must be defined. For simplicity, the mesh of points forms a net of rectangles. They are connected with three kinds of linear springs:

1. *Normal* spring with stiffness κ_i and energy $\kappa_i(\Delta b_i)^2/2$, where Δb_i represents the departure from the equilibrium distance b_i between two nodes along the tangential, axial, or diagonal direction (Fig. 3.2(a)).

2. *Angular* spring with stiffness τ and energy $\tau(-\Delta[\cos \varphi])^2/2$, which is associated with the relative orientation (angle φ) between two neighboring rectangles. They have a common axis of rotation $\hat{\mathbf{n}}_z$ parallel to the axial direction (Fig. 3.2(b)).
3. *Angular* spring with stiffness ζ and energy $-\zeta \Delta[\cos \varphi]$. It is associated with the relative orientation of two neighboring rectangles, which have an axis of rotation $\hat{\mathbf{n}}_\theta$ pointing in the tangential direction (Fig. 3.2(c)).

The spring κ involves the relative position of two nodes, while the two angular springs involve three nodes simultaneously (e.g. $\mathbf{r}_1, \mathbf{r}_2, \mathbf{r}_3$ in Fig. 3.2(b) and $\mathbf{r}_4, \mathbf{r}_5, \mathbf{r}_6$ in Fig. 3.2(c)). The difference between spring τ and spring ζ is that, in the last one, the two rectangles lie in the same plane when there is no deformation. For example, in a right circular cylinder the adjacent rectangles of the spring τ and of the spring ζ are in the tangential and axial direction respectively.

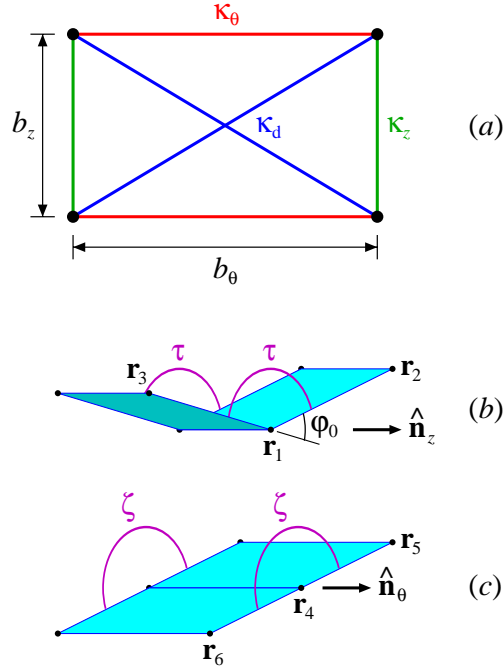


Figure 3.2: (a) Four nodes (black points) are connected by two springs of stiffness κ_θ (red lines), two springs of stiffness κ_z (green lines), and two springs of stiffness κ_d (blue lines). Increasing the distance b_θ by $b_\theta \varepsilon_{\theta\theta}$ (tangential direction) and the distance b_z by $b_z \varepsilon_{zz}$ (axial direction), also increases the length of the diagonal b_d . (b) Two adjacent non coplanar rectangles ($\varphi_0 \neq 0$) have two angular springs of stiffness τ connected to straight lines joining the nodes (e.g. $\mathbf{r}_2 - \mathbf{r}_1$ and $\mathbf{r}_3 - \mathbf{r}_1$). The axis of rotation is the unit vector $\hat{\mathbf{n}}_z$. (c) Two adjacent coplanar rectangles have two angular springs of stiffness ζ . The axis of rotation is $\hat{\mathbf{n}}_\theta$.

3.2.2.1 Normal Spring κ_i

The stiffness of the spring κ is related to the elastic properties of the tissues and to the geometry of the mesh. Consider a rectangle of size $b_\theta \times b_z$ subjected to the strains $\varepsilon_{\theta\theta}$ and ε_{zz} (Fig. 3.2(a)). Thus $\Delta b_\theta = b_\theta \varepsilon_{\theta\theta}$, $\Delta b_z = b_z \varepsilon_{zz}$, $\Delta b_d = (b_\theta^2 \varepsilon_{\theta\theta} + b_z^2 \varepsilon_{zz}) / \sqrt{b_\theta^2 + b_z^2}$, and since there are two springs κ of each kind in one rectangle, the stored energy reads

$$\begin{aligned} U_{\text{stretch}} &= 2 \frac{1}{2} \kappa_\theta (\Delta b_\theta)^2 + 2 \frac{1}{2} \kappa_z (\Delta b_z)^2 + 2 \frac{1}{2} \kappa_d (\Delta b_d)^2 \\ &= \left(\kappa_\theta b_\theta^2 + \kappa_d \frac{b_\theta^4}{b_\theta^2 + b_z^2} \right) \varepsilon_{\theta\theta}^2 + \left(\kappa_z b_z^2 + \kappa_d \frac{b_z^4}{b_\theta^2 + b_z^2} \right) \varepsilon_{zz}^2 \\ &\quad + 2 \kappa_d \frac{b_\theta^2 b_z^2}{b_\theta^2 + b_z^2} \varepsilon_{\theta\theta} \varepsilon_{zz} \end{aligned} \quad (3.16)$$

On the other hand, the elastic energy due to the homogeneous deformation is

$$U_{\text{stretch}} = \left(\frac{1}{2} c_{\theta\theta\theta\theta} \varepsilon_{\theta\theta}^2 + \frac{1}{2} c_{zzzz} \varepsilon_{zz}^2 + c_{\theta\theta zz} \varepsilon_{\theta\theta} \varepsilon_{zz} \right) V \quad (3.17)$$

where $V = \frac{1}{2} \theta (r_2^2 - r_1^2) b_z$ represents the volume. By comparing (3.16), (3.17), and solving for κ_i

$$\begin{aligned} \kappa_\theta &= \frac{1}{2} \left(\frac{c_{\theta\theta\theta\theta}}{b_\theta^2} - \frac{c_{\theta\theta zz}}{b_z^2} \right) V \\ \kappa_z &= \frac{1}{2} \left(\frac{c_{zzzz}}{b_z^2} - \frac{c_{\theta\theta zz}}{b_\theta^2} \right) V \\ \kappa_d &= \frac{1}{2} \left(\frac{1}{b_\theta^2} + \frac{1}{b_z^2} \right) c_{\theta\theta zz} V \end{aligned} \quad (3.18)$$

Because κ_θ , κ_z , and κ_d must be positive [133], the ratio between b_θ and b_z can not be arbitrary. Since $c_{\theta\theta\theta\theta} c_{zzzz} - c_{\theta\theta zz}^2 > 0$, it can be verified that for $b_\theta^2/b_z^2 = \sqrt{c_{\theta\theta\theta\theta}/c_{zzzz}}$ the stiffnesses are indeed positive. Finally, since the ET depends on the radius r , the components are replaced by the volume averages $\bar{c}_{\theta\theta\theta\theta}$, \bar{c}_{zzzz} , and $\bar{c}_{\theta\theta zz}$.

3.2.2.2 Angular Spring τ

The bending energy of a homogeneous beam of thickness $h = r_2 - r_1$ and a natural curvature radius R_0 , subjected to a deformation specified by a new radius R , is equal to

$$U_{\text{bend},\theta} = \frac{1}{2} \left(\frac{1}{R} - \frac{1}{R_0} \right)^2 g_\theta V \quad (3.19)$$

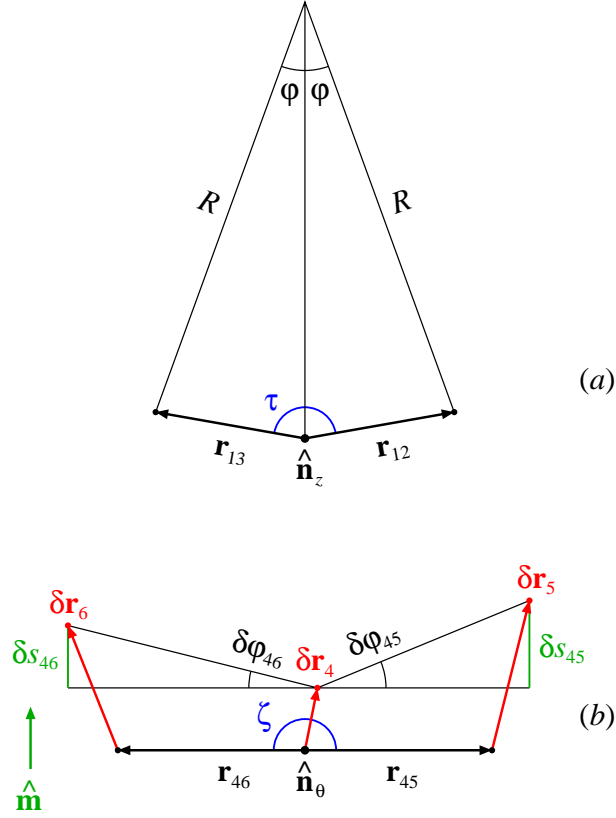


Figure 3.3: (a) Cross view of two adjacent rectangles perpendicular to the plane of the Figure, with nodes at the coordinates $\mathbf{r}_1, \mathbf{r}_2$ and $\mathbf{r}_1, \mathbf{r}_3$. The vectors \mathbf{r}_{12} and \mathbf{r}_{13} are the projections of $\mathbf{r}_2 - \mathbf{r}_1$ and $\mathbf{r}_3 - \mathbf{r}_1$ in the plane of the Figure. Without deformation, the moduli r_{12} and r_{13} are both equal to b_θ . The unit vector $\hat{\mathbf{n}}_z$, represented by the dot \bullet , is perpendicular to the Figure. When the rectangles are rotated along the axis defined by $\hat{\mathbf{n}}_z$, the structure is bent with a curvature radius R . The stiffness of the angular springs connected to the rectangles is τ (blue). (b) The unit vector $\hat{\mathbf{m}}$ is perpendicular to $\hat{\mathbf{n}}_\theta$ and to $\hat{\mathbf{r}}_{45} - \hat{\mathbf{r}}_{46}$. The lengths δs_{45} and δs_{46} are the projections of $\delta \mathbf{r}_5 - \delta \mathbf{r}_4$ and $\delta \mathbf{r}_6 - \delta \mathbf{r}_4$ along $\hat{\mathbf{m}}$. Hence, up to first order $\delta \varphi_{45} = \delta s_{45}/r_{45}$ and $\delta \varphi_{46} = \delta s_{46}/r_{46}$.

with $g_\theta = c_{\theta\theta\theta}h^2/12$. Notice that the bending energy of the bar is shared with two additional springs τ located at \mathbf{r}_2 and \mathbf{r}_3 (only the spring τ located at \mathbf{r}_1 is shown in Fig. 3.3(a)). Hence, V is only half of the bar volume which is associated with two adjacent rectangles of thickness h , so that V coincides with the value previously used in (3.17).

From Fig. 3.3(a) it can be inferred that $b_\theta = 2R \sin(\varphi/2)$, so that

$$\frac{1}{R} - \frac{1}{R_0} = \frac{2}{b_\theta} \left(\sin \frac{\varphi}{2} - \sin \frac{\varphi_0}{2} \right) \quad (3.20)$$

For φ close to φ_0 , it follows that up to first order in $\Delta\varphi = \varphi - \varphi_0$

$$2\left(\sin\frac{\varphi}{2} - \sin\frac{\varphi_0}{2}\right) = \Delta\varphi \cos\frac{\varphi_0}{2} = \frac{\cos\varphi_0 - \cos\varphi}{2\sin\frac{\varphi_0}{2}} \quad (3.21)$$

Substituting (3.20) and (3.21) in (3.19)

$$U_{\text{bend},\theta} = \frac{1}{2} \frac{g_\theta V}{\left(2b_\theta \sin\frac{\varphi_0}{2}\right)^2} (\cos\varphi_0 - \cos\varphi)^2 \quad (3.22)$$

On the other hand, there are two springs τ connected to a pair of rectangles (Fig. 3.2(b))

$$U_{\text{bend},\theta} = 2\frac{1}{2}\tau\left(-\Delta[\cos\varphi]\right)^2 \quad (3.23)$$

Hence, from (3.22) and (3.23)

$$\tau = \frac{1}{2} \frac{g_\theta V}{\left(2b_\theta \sin\frac{\varphi_0}{2}\right)^2} \quad (3.24)$$

Since $\hat{\mathbf{r}}_{12} \cdot \hat{\mathbf{r}}_{13} = \cos(\pi - \varphi) = -\cos\varphi$, for numerical purposes it is convenient to use $-\Delta[\cos\varphi] = \Delta[\hat{\mathbf{r}}_{12} \cdot \hat{\mathbf{r}}_{13}]$. The vectors \mathbf{r}_{12} and \mathbf{r}_{13} are the components of $\mathbf{r}_2 - \mathbf{r}_1$ and $\mathbf{r}_3 - \mathbf{r}_1$ perpendicular to the rotation axis $\hat{\mathbf{n}}_z$, respectively. Furthermore, some useful formulas are

$$\begin{aligned} \nabla_1[\hat{\mathbf{r}}_{12} \cdot \hat{\mathbf{r}}_{13}] &= \left(\frac{\hat{\mathbf{r}}_{12}}{r_{12}} - \frac{\hat{\mathbf{r}}_{13}}{r_{13}}\right) \times (\hat{\mathbf{r}}_{12} \times \hat{\mathbf{r}}_{13}) \\ \nabla_2[\hat{\mathbf{r}}_{12} \cdot \hat{\mathbf{r}}_{13}] &= -\frac{\hat{\mathbf{r}}_{12}}{r_{12}} \times (\hat{\mathbf{r}}_{12} \times \hat{\mathbf{r}}_{13}) \\ \nabla_3[\hat{\mathbf{r}}_{12} \cdot \hat{\mathbf{r}}_{13}] &= \frac{\hat{\mathbf{r}}_{13}}{r_{13}} \times (\hat{\mathbf{r}}_{12} \times \hat{\mathbf{r}}_{13}) \end{aligned} \quad (3.25)$$

and in particular

$$\delta[\hat{\mathbf{r}}_{12} \cdot \hat{\mathbf{r}}_{13}] = \nabla_1[\hat{\mathbf{r}}_{12} \cdot \hat{\mathbf{r}}_{13}] \cdot \delta\mathbf{r}_1 + \nabla_2[\hat{\mathbf{r}}_{12} \cdot \hat{\mathbf{r}}_{13}] \cdot \delta\mathbf{r}_2 + \nabla_3[\hat{\mathbf{r}}_{12} \cdot \hat{\mathbf{r}}_{13}] \cdot \delta\mathbf{r}_3 \quad (3.26)$$

which can be used in the derivation of the Stiffness Matrix. Notice that the Stiffness Matrix changes when the position of the nodes are updated. However, the displacement of the nodes is usually small [134] and the convergence is very fast. Although the model linearizes and homogenizes the material response in the linear springs, it still contemplates the geometric nonlinearity by updating the reference frame to the deformed geometry.

3.2.2.3 Angular Spring ζ

The previous calculation does not work if $R_0 \rightarrow \infty$, because $\varphi_0 = 0$ and the first order approximation in (3.21) vanishes (the right side becomes undetermined). For $\varphi \ll 1$ Eqs. (3.19) and (3.20) are replaced by

$$U_{\text{bend},z} = \frac{1}{2} \frac{g_z V}{R^2}$$

$$\frac{1}{R} = \frac{2}{b_z} \sin \frac{\varphi}{2} \approx \frac{\varphi}{b_z}$$

so that

$$U_{\text{bend},z} = \frac{g_z V}{b_z^2} \frac{\varphi^2}{2} \quad (3.27)$$

Up to second order in φ , it follows that $\Delta[\hat{\mathbf{r}}_{45} \cdot \hat{\mathbf{r}}_{46}] = -\Delta[\cos \varphi] = -\cos \varphi + 1 = \varphi^2/2$. There are two springs ζ connecting a pair of rectangles (Fig. 3.2(c)), so that (3.27) becomes

$$U_{\text{bend},z} = 2\zeta \Delta[\hat{\mathbf{r}}_{45} \cdot \hat{\mathbf{r}}_{46}] \quad (3.28)$$

where

$$\zeta = \frac{1}{2} \frac{g_z V}{b_z^2} \quad (3.29)$$

By replacing $\hat{\mathbf{r}}_{12} \rightarrow \hat{\mathbf{r}}_{45}$ and $\hat{\mathbf{r}}_{13} \rightarrow \hat{\mathbf{r}}_{46}$, the gradients in (3.25) vanish, because $\hat{\mathbf{r}}_{45}$ and $\hat{\mathbf{r}}_{46}$ are antiparallel. Thus, Eq. (3.26) can not be used to calculate the Stiffness Matrix. Instead, from the geometry in Fig. 3.3(b) it can be seen that

$$\delta\varphi = \delta\varphi_{45} + \delta\varphi_{46} = \frac{\hat{\mathbf{m}} \cdot (\delta\mathbf{r}_5 - \delta\mathbf{r}_4)}{r_{45}} + \frac{\hat{\mathbf{m}} \cdot (\delta\mathbf{r}_6 - \delta\mathbf{r}_4)}{r_{46}} \quad (3.30)$$

where the unit vector $\hat{\mathbf{m}}$ is parallel to $\hat{\mathbf{n}}_\theta \times (\hat{\mathbf{r}}_{45} - \hat{\mathbf{r}}_{46})$.

As noted previously, the ET depends on the radius r . Hence, g_i in (3.24) and (3.29) are replaced by the volume average

$$\bar{g}_i = \frac{1}{V} \int c_{iii}(r - \bar{r}_i)^2 dV \quad (3.31)$$

where \bar{r}_i is the radius to the neutral axis of the beam

$$\bar{r}_i = \frac{1}{\bar{c}_{iii} V} \int c_{iii} r dV \quad (3.32)$$

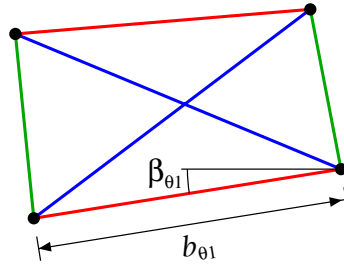


Figure 3.4: When the rectangle in Fig. 3.2(a) is deformed and/or rotated, the lengths and the orientations (relative to the tangential and axial directions) are modified. For simplicity, only the length $b_{\theta 1}$ and the angle $\beta_{\theta 1}$ are shown. The spring stiffnesses between the nodes are the same as before.

3.2.2.4 Generalizations to Other Geometries

When the rectangle is deformed to a quadrilateral or the orientation changes (Fig. 3.4), the results of Section 3.2.2.1 must be modified. Under the strains $\varepsilon_{\theta\theta}$ and ε_{zz} , the length variation of $b_{\theta 1}$ is

$$\Delta b_{\theta 1} = b_{\theta 1}(\varepsilon_{\theta\theta} \cos^2 \beta_{\theta 1} + \varepsilon_{zz} \sin^2 \beta_{\theta 1}) \quad (3.33)$$

with analogous formulas for $\Delta b_{\theta 2}$, Δb_{z1} , Δb_{z2} , Δb_{d1} , and Δb_{d2} . In addition, (3.16) must be replaced by

$$\begin{aligned} U_{\text{stretch}} = & \frac{1}{2} \kappa_{\theta} (\Delta b_{\theta 1})^2 + \frac{1}{2} \kappa_z (\Delta b_{z1})^2 + \frac{1}{2} \kappa_d (\Delta b_{d1})^2 \\ & + \frac{1}{2} \kappa_{\theta} (\Delta b_{\theta 2})^2 + \frac{1}{2} \kappa_z (\Delta b_{z2})^2 + \frac{1}{2} \kappa_d (\Delta b_{d2})^2 \end{aligned} \quad (3.34)$$

Substituting (3.33) in (3.34) and comparing the coefficients of $\varepsilon_{\theta\theta}^2$, $\varepsilon_{\theta\theta}\varepsilon_{zz}$, and ε_{zz}^2 with (3.17), the spring stiffnesses are obtained. Note that V in (3.17) now represents the volume of the quadrilateral of thickness h .

Furthermore, the calculations of Section 3.2.2.2 are also modified. Considering that part of the beam with radius R_{12} in Fig. 3.5(a) and proceeding as before, it is deduced that

$$U_{\text{bend},\theta 12} = \frac{1}{2} \frac{g_{\theta} V_{\theta 12}}{\left(2b_{\theta 12} \sin \frac{\varphi_0}{2}\right)^2} (\cos \varphi_0 - \cos \varphi)^2$$

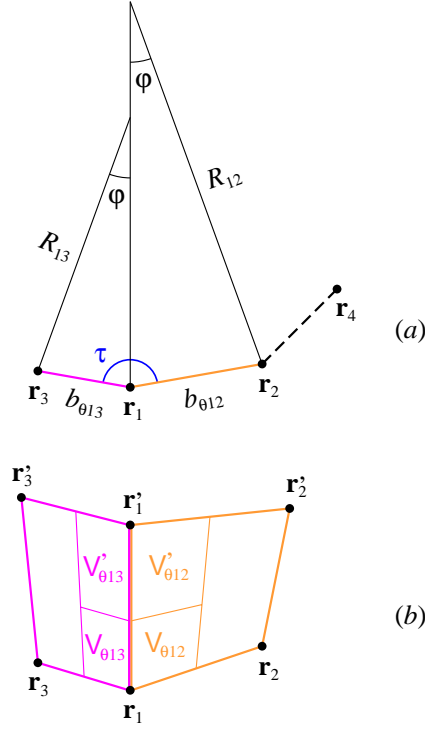


Figure 3.5: (a) If the adjacent rectangles in Fig. 3.3(a) are not rectangles with the same dimensions, then the bending radius on the right (R_{12}) and the bending radius on the left (R_{13}) are different. The distances between the points are replaced by $b_{\theta 12} = 2R_{12} \sin(\varphi/2)$ and $b_{\theta 13} = 2R_{13} \sin(\varphi/2)$. It is possible to join the points using the same radius $R_{12} = R_{13}$ but different angles $\varphi_{12} \neq \varphi_{13}$. However, in this case, the line defining the beam will not be smooth when connecting consecutive parts, since the radius and the center of the circles (e.g. through \mathbf{r}_3 , \mathbf{r}_1 , \mathbf{r}_2 and through \mathbf{r}_1 , \mathbf{r}_2 , \mathbf{r}_4) will not coincide. (b) Top view of Fig. (a). Note that the points \mathbf{r}'_1 , \mathbf{r}'_2 , and \mathbf{r}'_3 are not represented because they are hidden behind \mathbf{r}_1 , \mathbf{r}_2 , and \mathbf{r}_3 . The sum $V_{\theta 12} + V'_{\theta 12}$ is equal to one half of V_{right} (the volume of the yellow region of thickness h defined by the points \mathbf{r}_1 , \mathbf{r}_2 , \mathbf{r}'_2 , and \mathbf{r}'_1) and $V'_{\theta 12}/V_{\theta 12} = V'_{\theta 13}/V_{\theta 13}$.

The volumes $V_{\theta 12}$ and $V_{\theta 13}$ are calculated with the formulas

$$\begin{aligned} V_{\theta 12} &= \frac{f'_\theta}{f_\theta + f'_\theta} \frac{V_{\text{right}}}{2} \\ V_{\theta 13} &= \frac{f'_\theta}{f_\theta + f'_\theta} \frac{V_{\text{left}}}{2} \end{aligned} \quad (3.35)$$

where V_{right} and V_{left} represent the beam volumes to the right and to the left in Fig.

3.5(b) respectively, and

$$\begin{aligned} f_\theta &= \frac{1}{\sin^2 \frac{\varphi_0}{2}} \left(\frac{V_{\text{right}}}{b_{\theta 12}^2} + \frac{V_{\text{left}}}{b_{\theta 13}^2} \right) \\ f'_\theta &= \frac{1}{\sin^2 \frac{\varphi'_0}{2}} \left(\frac{V_{\text{right}}}{b_{\theta 12}^2} + \frac{V_{\text{left}}}{b_{\theta 13}^2} \right) \end{aligned} \quad (3.36)$$

An analogous formula is obtained for $U_{\text{bend},\theta 13}$. Comparing the sum $U_{\text{bend},\theta 12} + U_{\text{bend},\theta 13}$ with $\frac{1}{2}\tau(-\Delta[\cos \varphi])^2$, it is deduced that

$$\tau = \frac{g_\theta}{4 \sin^2 \frac{\varphi_0}{2}} \left(\frac{V_{\theta 12}}{b_{\theta 12}^2} + \frac{V_{\theta 13}}{b_{\theta 13}^2} \right) \quad (3.37)$$

Notice that in Fig. 3.5(b) there is a second spring of stiffness τ' connected to the straight lines through $\mathbf{r}'_1, \mathbf{r}'_2$ and through $\mathbf{r}'_1, \mathbf{r}'_3$. Using (3.35) and (3.36), it can be shown that τ' coincides with τ in (3.37).

Proceeding in a similar way, the stiffness of the spring ζ is generalized to

$$\zeta = g_z \left(\frac{V_{z 12}}{b_{z 12}^2} + \frac{V_{z 13}}{b_{z 13}^2} \right) \quad (3.38)$$

Further, the computation of the volumes $V_{z 12}$ and $V_{z 13}$ is similar to (3.35), but making use of

$$\begin{aligned} f_z &= \frac{V_{\text{right}}}{b_{z 12}^2} + \frac{V_{\text{left}}}{b_{z 13}^2} \\ f'_z &= \frac{V_{\text{right}}}{b'_{z 12}^2} + \frac{V_{\text{left}}}{b'_{z 13}^2} \end{aligned} \quad (3.39)$$

3.3 Pseudocode

The pseudocode to calculate the spring constants in the cylindrical case is shown in the Algorithm 3.1. Briefly, it involves the determination of the strain field (lines 1–3), the calculation of \bar{c}_{ijj} , \bar{r}_i , \bar{g}_i (lines 4–6), and the computation of the spring constants (lines 8–9).

To apply the method to other geometries (Section 3.2.2.4) it is necessary to modify the calculations in the following way:

- The integration methods in lines 1–3 are no longer valid. Instead, FEM can be used to find the strain field and after that obtain c_{ijj} as function of the position.
- The neutral axis in line 5 is a cylindrical surface of radius \bar{r}_i . However, when the tissue thicknesses or the shape of the artery vary, the surface of the neutral

Algorithm 3.1: Calculation of the spring constants for a right circular cylindrical artery. The input geometrical parameters are the tissue thicknesses a_i , a_m , a_a , the internal radius R_{in} , the opening angle α , and the axial stretch λ_z . The physical parameters are those appearing in Eqs. (3.1)–(3.4). Finally, n_{vert} represents the number of vertices of the polyline discretizing the artery in the tangential direction and \bar{p}_{in} is the average internal pressure.

```

void SpringConstants(artery geometry, physical constants, int  $n_{\text{vert}}$ , float
 $\bar{p}_{\text{in}}$ ) {
  1. set  $\sigma_{rr}(r_1) = -\bar{p}_{\text{in}}$  and  $\lambda_{\theta\text{in}} = 1$ ;
  2. integrate Eq. (3.15) to obtain  $\sigma_{rr}(r_2)$ ;
  3. if  $\sigma_{rr}(r_2) \neq 0$ , then vary  $\lambda_{\theta\text{in}}$  and go back to 2;
  4. calculate the volume integrals of  $c_{\theta\theta\theta\theta}$ ,  $c_{\theta\theta z z}$ ,  $c_{z z z z}$  in Eq. (3.11) and
    divide by the volume  $V$  to obtain  $\bar{c}_{\theta\theta\theta\theta}$ ,  $\bar{c}_{\theta\theta z z}$ ,  $\bar{c}_{z z z z}$ ;
  5. calculate the volume integrals of  $rc_{\theta\theta\theta\theta}$ ,  $rc_{z z z z}$  and divide by  $V\bar{c}_{\theta\theta\theta\theta}$ ,
     $V\bar{c}_{z z z z}$  respectively, to obtain the radii  $\bar{r}_\theta$ ,  $\bar{r}_z$  to the neutral axis (Eq.
    (3.32));
  6. calculate the volume integrals of  $(r - \bar{r}_\theta)^2 c_{\theta\theta\theta\theta}$ ,  $(r - \bar{r}_z)^2 c_{z z z z}$  and divide
    by  $V$  to obtain  $\bar{g}_\theta$ ,  $\bar{g}_z$  (Eq. (3.31));
  7. determine the dimensions of the rectangle in Figure 3.2 with the
    formulas  $\theta = 2\pi/n_{\text{vert}}$ ,  $b_\theta = 2r_1 \sin(\theta/2)$ ,  $b_z = b_\theta(\bar{c}_{z z z z}/\bar{c}_{\theta\theta\theta\theta})^{1/4}$ ;
  8. use the values of  $\bar{c}_{\theta\theta\theta\theta}$ ,  $\bar{c}_{\theta\theta z z}$ ,  $\bar{c}_{z z z z}$  in line 4 and of  $b_\theta$ ,  $b_z$  in line 7 to
    calculate the spring constants  $\kappa_\theta$ ,  $\kappa_z$ ,  $\kappa_d$  (Eq. (3.18));
  9. use the values of  $\bar{g}_\theta$ ,  $\bar{g}_z$  in line 6 and of  $b_\theta$ ,  $b_z$  in line 7 to calculate the
    angular spring constants  $\tau$  in Eq. (3.24) (with  $\varphi_0 \rightarrow \theta$ ) and  $\zeta$  in Eq. (3.29);
}

```

axis is not cylindrical. For example, consider a voxel as shown in Fig. 3.6. The neutral axis \bar{x} depends on z (black line)

$$\bar{x}(z) = \frac{\iint x c_{zzzz}(x, y, z) dx dy}{\iint c_{zzzz}(x, y, z) dx dy} \quad (3.40)$$

where the integral is carried out over the cross section with $z = \text{const}$ (red). Then

$$\bar{g}_z = \frac{1}{V} \iiint [x - \bar{x}(z)]^2 c_{zzzz}(x, y, z) dx dy dz \quad (3.41)$$

The value of \bar{g}_θ can be calculated in a similar way.

- In general, the rectangles are deformed into quadrilaterals and the formulas in line 7 are not used.¹ However, after the spring constants have been calculated, it must be checked if all constants are positive [133]. Otherwise the quadrilateral geometry has to be changed² and the calculations are repeated.
- Finally, to determine the springs constants in lines 8 and 9, Eqs. (3.37)–(3.38) are used.

3.4 Technical Evaluation

Experimental and computational studies suggest a substantial variation in the mechanical responses of the arterial wall layers [135]. In order to calculate values for the ET, the physical parameters listed in Table 3.1 are used. The mean pressure loading \bar{p}_{in} is assumed to be equal to $(80 + 120)/2 = 100$ mm Hg [136]. Furthermore, the internal radius is $R_{\text{in}} = 1.35$ mm and in the special case $\lambda_z = 1$ and $k = 1$ (no residual strains), the calculated stretch at the inner surface is $\lambda_{\theta\text{in}} = 1.1495$, the mean stretch is $\bar{\lambda}_\theta = 1.088$, and the internal radius is $r_1 = 1.55$ mm. Then the volume averages of the ET components are $\bar{c}_{\theta\theta\theta\theta} = 558$ kPa, $\bar{c}_{zzzz} = 844$ kPa, and $\bar{c}_{\theta\theta zz} = 505$ kPa. Moreover, $\bar{g}_\theta = 15.3$ mN and $\bar{g}_z = 29.7$ mN.

3.4.1 Stiffness Analysis

The cylindrical artery is discretized by a polyline having 24 vertices in the tangential direction (Fig. 3.7). Using (3.18), (3.24), and (3.29) the following spring stiffnesses are obtained: $\kappa_\theta = 85.3$ N/m, $\kappa_z = 105$ N/m, $\kappa_d = 532$ N/m, $\tau = 130$ μJ , and $\zeta = 14.0$ μJ . When two or three nodes have multiple rectangles in common, the equivalent stiffness equals the sum.

¹When the quadrilateral becomes a rectangle, line 7 can be applied and the calculated spring constants are always positive. Line 7 is not a “must” but it is a convenient choice.

²Note that this action affects neighbouring quadrilaterals.

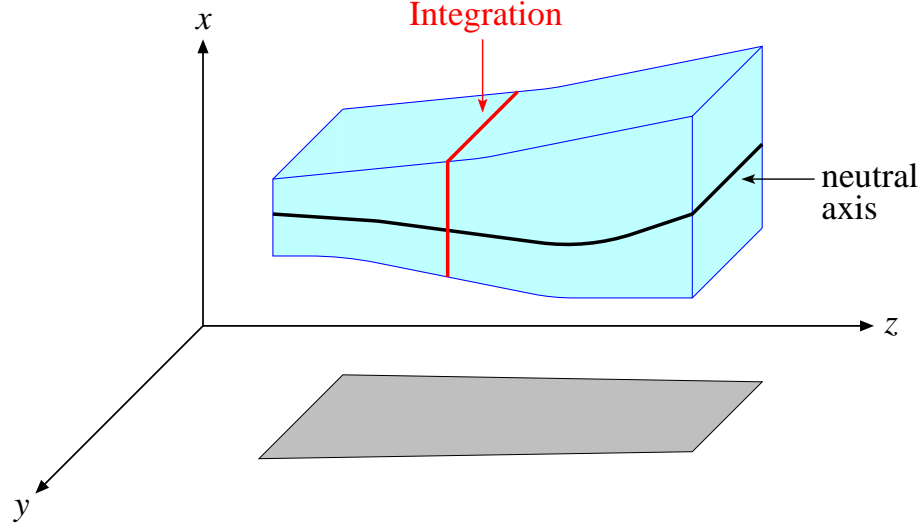


Figure 3.6: View of a voxel (cian) corresponding to the volume V of the arterial wall delimited by a quadrilateral parallel to the yz plane (shadow). The normal to the arterial wall points in the x axis direction. For a given z , the integration area (red) of Eq. (3.40) is parallel to the xy plane. The neutral axis (black line) depends on the z coordinate.

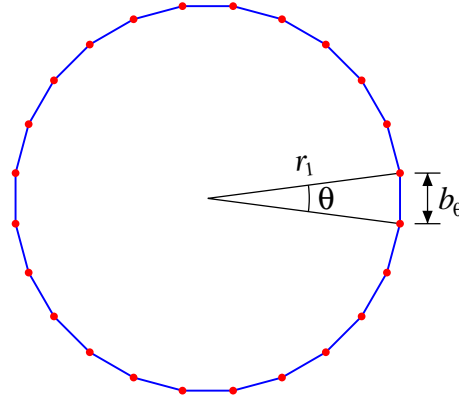


Figure 3.7: Cross view of the artery discretized by a polyline. The angle is $\theta = 2\pi/24$ and the inner radius (with an internal pressure equal to \bar{p}_{in}) is $r_1 = 1.55$ mm. Thus, the rectangle dimensions in Fig. 3.2 are $b_\theta = 2r_1 \sin(\theta/2) = 0.405$ mm and $b_z = b_\theta (\bar{c}_{zzzz}/\bar{c}_{\theta\theta\theta})^{1/4} = 0.449$ mm.

It is instructive to analyze the behavior of the stiffnesses when the resolution or radius change. For simplicity, let the thickness h and the ET be constants. First, consider the case where the radius does not vary and $\theta \rightarrow \theta' = \theta/2$ with $\theta \ll 1$ rad. Then $b_\theta \rightarrow b'_\theta = b_\theta / (2 \cos[\theta/4]) \approx b_\theta/2$, $b_z \rightarrow b'_z = b_z / (2 \cos[\theta/4]) \approx b_z/2$, $V \rightarrow V' = V / (4 \cos[\theta/4]) \approx V/4$, and $\varphi_0 \rightarrow \varphi'_0 = \varphi_0/2$. Within this approximation,

it can be concluded from (3.18), (3.24), and (3.29), that all spring stiffnesses are nearly the same before and after increasing the resolution, with the exception of τ which is replaced by $\tau' \approx 4\tau$. Indeed, by repeating the previous calculations with 48 vertices, the ratio between the new and the old spring stiffnesses are $\kappa'_\theta/\kappa_\theta = \kappa'_z/\kappa_z = \kappa'_d/\kappa_d = \zeta'/\zeta = 0.9979$ and $\tau'/\tau = 3.974$.

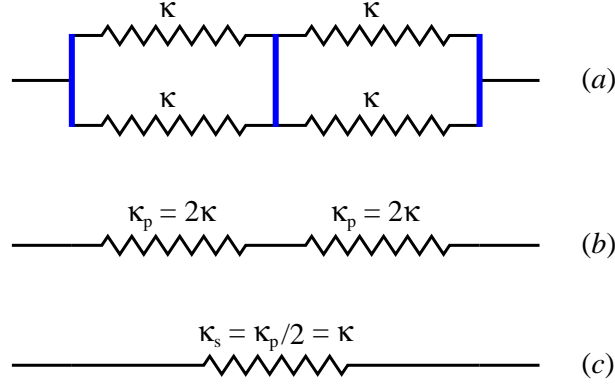


Figure 3.8: (a) Four springs of stiffness κ (connected in parallel and then in series) are joined by rigid vertical bars (blue). (b) Two springs connected in parallel are equivalent to one spring of stiffness $\kappa_p = \kappa + \kappa = 2\kappa$ [137]. (c) The two springs connected in series are equivalent to one spring of stiffness $\kappa_s = \kappa_p \kappa_p / (\kappa_p + \kappa_p) = \kappa_p / 2$.

With this new resolution, the number of springs κ connected in *series* doubles and the number of springs κ connected in *parallel* doubles, so that the *equivalent* stiffness is the same (Fig. 3.8). In other words, increasing the resolution does not change the stiffness κ_i up to first order.

Consider now the situation where the artery has a bigger radius. If $r_1 \rightarrow r'_1 = 2r_1$, then $b_\theta \rightarrow b'_\theta = 2b_\theta$, $b_z \rightarrow b'_z = 2b_z$, and $V \rightarrow V' = 4V - \theta h^2 b_z \approx 4V$ for $h \ll r_1$. Hence, doubling the radius keeps the spring stiffness constant. Since the radial force acting on the nodes is given by $F_r = b_\theta b_z p_{\text{in}}$, it follows that $F'_r = b'_\theta b'_z p_{\text{in}} = 4F_r$ and the deformation must be 4 times larger to balance the applied force. As a consequence, the tangential strain

$$\varepsilon_{\theta\theta} = \frac{\Delta r_1}{r_1} \quad (3.42)$$

doubles. However, a numerical calculation with the method described in Section 3.2 shows that $\kappa'_i \neq \kappa_i$ (case (i) of Table 3.2), because V' is substantially smaller than $4V$ (the condition $h \ll r_1$ is not fulfilled). Moreover, by increasing the radius, the tangential stress as well as the tangential strain increase, and the ET components become larger (Section 3.4.3).

Finally, if h is also doubled, then $V' = 8V$ and the stiffness of the springs κ is multiplied by 2 (case (ii) of Table 3.2). Note that the deformation Δr_1 ($\propto F_r/\text{stiffness}$) is two times bigger and according to (3.42) the tangential strain does not vary, so

Table 3.2: Ratio between the physical parameters for $R'_{\text{in}} = 2R_{\text{in}}$ and two different layer thicknesses: (i) $h' = h$, (ii) $h' = 2h$. In the calculations the values $R_{\text{in}} = 1.35$ mm and $h = a_i + a_m + a_a = 0.90$ mm are used.

case	$\bar{\lambda}'_{\theta}/\bar{\lambda}_{\theta}$	$\bar{c}'_{\theta\theta\theta\theta}/\bar{c}_{\theta\theta\theta\theta}$	$\bar{c}'_{zzzz}/\bar{c}_{zzzz}$	$\bar{c}'_{\theta\theta zz}/\bar{c}_{\theta\theta zz}$	$\bar{g}'_{\theta}/\bar{g}_{\theta}$	\bar{g}'_z/\bar{g}_z
i	1.0365	2.962	2.367	2.918	1.567	1.238
ii	1	1	1	1	4	4
case	V'/V	$\kappa'_{\theta}/\kappa_{\theta}$	κ'_z/κ_z	κ'_d/κ_d	τ'/τ	ζ'/ζ
i	3.367	1.721	1.538	2.499	1.274	1.126
ii	8	2	2	2	8	8

that $\bar{c}_{\theta\theta\theta\theta}$, \bar{c}_{zzzz} , and $\bar{c}_{\theta\theta zz}$ remain constant. On the other hand, the \bar{g}_i are multiplied by 4 because they are proportional to h^2 .

These conclusions are in conformity with a mechanical analysis. If the internal pressure in a cylinder equals p_{in} , then the tangential force per unit length is $F_{\theta}/b_z = r_1 p_{\text{in}}$. Assuming $h \ll r_1$ the tangential stress is then

$$\sigma_{\theta\theta} = \frac{r_1}{h} p_{\text{in}}$$

At low stretches the strain is proportional to the stress [53] so that $\varepsilon_{\theta\theta} \propto r_1/h$. If $r_1 \rightarrow 2r_1$ and $h = \text{constant}$, then the strain doubles, but if $r_1 \propto h$, the strain does not change. In general, the following equation holds for a cylinder under a uniform tangential strain

$$\varepsilon_{\theta\theta} = \frac{r_1}{\Omega} p_{\text{in}}$$

where

$$\Omega = \int_{r_1}^{r_1+h} c_{\theta\theta\theta\theta} dr$$

The artery deformation depends on the pressure, on the internal radius, and on the parameter Ω , which in turn is a function of the thickness and of the elasticity.

3.4.2 Comparison of Models

Three different tests are performed to validate the calculations. Specifically, the results of our discrete model (label **A**) are compared with the nonlinear incompressible artery model of Holzapfel et al. [127] (label **B**), corresponding to Eqs. (3.1)-(3.6), (3.12), (3.14), and (3.15).

Furthermore, these models are compared with calculations performed using a

plane strain FEM (label C). Due to the axial symmetry, it gets reduced to a one dimensional problem and the displacement field can be characterized by a single parameter r_1 , which ensures incompressibility. From (3.8) and (3.12)

$$\delta\varepsilon_{\theta\theta} = \delta\left[\ln(\lambda_\theta/\lambda_{\theta 0})\right] = \frac{k\lambda_z r_1 \delta r_1}{R_{\text{in}}^2 + k\lambda_z(r^2 - r_1^2)}$$

The stress component σ_{rr} cannot be calculated with the model described by Eq. (3.1). Moreover, $\sigma_{rr} \ll \sigma_{\theta\theta}$ because the fiber reinforcement is mainly between the tangential and axial directions, not in the radial direction [128]. Thus, the approximation $\boldsymbol{\sigma} : \delta\boldsymbol{\varepsilon} = \sigma_{\theta\theta} \delta\varepsilon_{\theta\theta} + \sigma_{rr} \delta\varepsilon_{rr} \approx \sigma_{\theta\theta} \delta\varepsilon_{\theta\theta}$ is assumed. The internal virtual work is

$$\int \boldsymbol{\sigma} : \delta\boldsymbol{\varepsilon} dV = \int_{r_1}^{r_2} \sigma_{\theta\theta} \frac{k\lambda_z r_1 \delta r_1}{R_{\text{in}}^2 + k\lambda_z(r^2 - r_1^2)} 2\pi r l dr \quad (3.43)$$

where l represents the axial length of the right circular cylinder. Furthermore, the external virtual work due to the surface force is

$$\int p \delta r_1 dS = 2\pi r_1 l p \delta r_1 \quad (3.44)$$

At equilibrium (3.43) and (3.44) are equal³, so

$$p = \int_{r_1}^{r_2} \sigma_{\theta\theta} \frac{k\lambda_z r}{R_{\text{in}}^2 + k\lambda_z(r^2 - r_1^2)} dr \quad (3.45)$$

Note that $\sigma_{\theta\theta} = \sigma_{\theta\theta}(\lambda_\theta, \lambda_z)$, $\lambda_\theta = \lambda_\theta(r_1)$, and $r_2 = r_2(r_1)$ (see (3.12) and (3.14)). Hence $p = p(r_1)$ or, inverting numerically this equation, $r_1 = r_1(p)$. The knowledge of r_1 allows for the calculation, for example, of the average tangential stretch $\bar{\lambda}_\theta$ in (3.13) or the axial force component $\int \sigma_{zz} dS$.

Usually, the velocity of the arterial wall displacement is slow, because in a surgical procedure the tool movements are not abrupt [139]. Thus, the deformation is quasi-static which means that the nodes should reach the equilibrium position instantaneously. Hence, it is necessary to compare only static deformations.

3.4.2.1 Pressure-Inflation

The inflation is the most common artery deformation [140]. Since the radial stress is smaller than the tangential stress by a factor $h/r_1 < 1$ (Section 3.4.1), it is reasonable to neglect the radial direction and to work in two dimensions. Furthermore, in this case there is no axial displacement (Fig. 3.9(a)) and the essential parameter describing the deformation is the tangential stretch.

Figure 3.10 illustrates the mechanical response for pressures varying between 80 and 120 mm Hg. If the residual strain ($\lambda_z > 1$, $k > 1$) is considered or the external

³The external virtual work is equal to internal virtual work when equilibrated forces and stresses undergo unrelated but consistent displacements and strains [138].

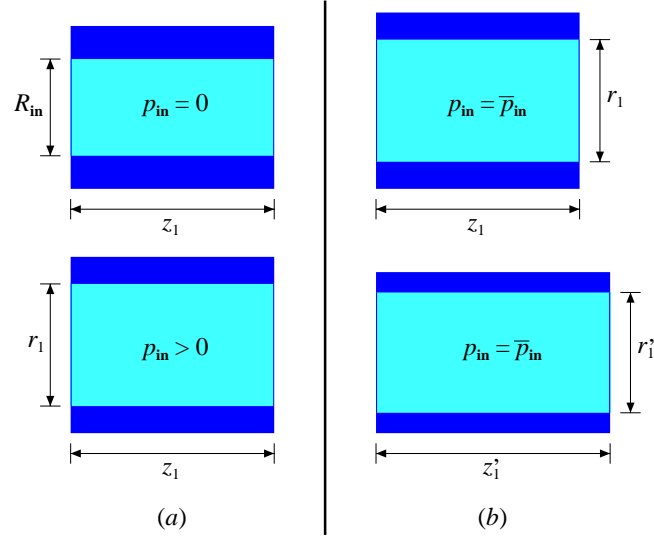


Figure 3.9: Axial view of the artery submitted to different boundary conditions.
 (a) The pressure p_{in} increases and the axial length z_1 is kept constant. As a result, the tangential stretch and the radius r_1 vary (bottom).
 (b) The pressure is kept constant at \bar{p}_{in} , the length increases from z_1 (top) to z'_1 (bottom), and the radius becomes smaller ($r_1 \rightarrow r'_1$).

surface is not stress-free ($\sigma_{rr}(r_2) > 0$), then the pressure/radius response of the artery and the tangential stress would change [128, 141]. The computed stretch $\bar{\lambda}_\theta = 1.088$ at $p_{in} = \bar{p}_{in}$ is not far from the average experimental result of 1.06 obtained by Schulze-Bauer et al. [142] for arteries of elderlies. Further, they found the average 1.07 for the axial stretch λ_z and in one case it was negative, showing that λ_z has a wide variation.

Models B and C are nonlinear and show a similar stretch variation. If $p_{in} > \bar{p}_{in}$ the artery in model B becomes stiffer than in model A. The stresses are nonlinear functions of the stretches and the stiffnesses increase as the circumferential stretch increase [106]. On the other hand, model A corresponds to a linearization around \bar{p}_{in} , so that for small deformations the stress is proportional to the strain. In the stretch calculations of model A, only $\Delta\bar{\lambda}_\theta$ is meaningful because the initial stretch $\bar{\lambda}_\theta$ is given beforehand, when the spring stiffnesses at $p_{in} = \bar{p}_{in}$ are computed.

Considering the internal pressure p_{in} in the range from 80 and 120 mm Hg, the average strain $\bar{\varepsilon}_{\theta\theta}$ in model A is in the interval [0.07703, 0.09187] (the variation is smaller than 1.5%). It can be inferred from Fig. 3.10 that the linearization gives a good approximation within this pressure range, in accordance with the conclusions of Kerdok et al. [143].

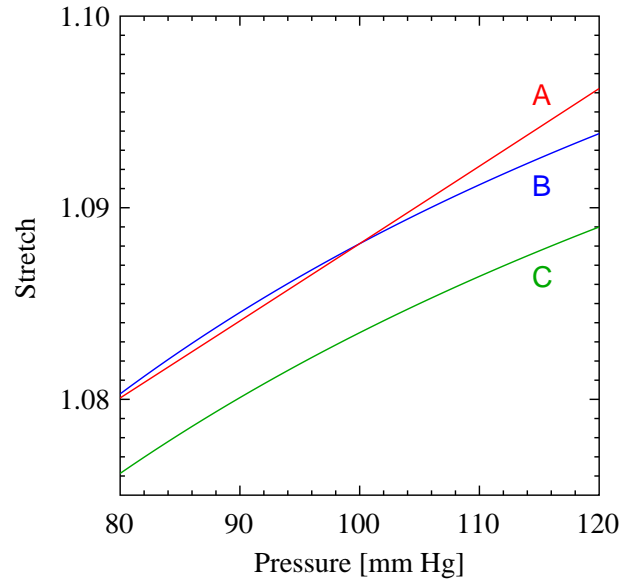


Figure 3.10: Average circumferential stretch $\bar{\lambda}_\theta$ as a function of blood pressure p_{in} without residual strain and without external surface traction. The red, blue, and green lines correspond to the calculations with model A (this work), with model B (nonlinear and incompressible artery of Holzapfel et al. [127]), and with model C (one dimensional FEM).

3.4.2.2 Axial Force

Besides the tangential direction, the axial direction is also relevant in the two dimensional model. Thus, a test including the axial deformation from $\lambda_z = 1$ to $\lambda_z = 1.01$ is performed to further validate the model. The blood pressure is kept constant at \bar{p}_{in} , the radius is not fixed (Fig. 3.9(b)), and as a consequence $\bar{\lambda}_\theta$ decreases. The axial forces calculated with models A, B, and C are 0.03971 N, 0.03633 N, and 0.03530 N, respectively. The discrepancy of 9.3% between models A and B can be mainly attributed to variations of the ET when the stretches are modified. On the other hand, the discrepancy between models B and C is only 2.8%, showing that it is more accurate than model A.

However, the calculations with model C become more difficult as the symmetry is reduced because the displacement field is not given by the single parameter r_1 . Therefore, a 3D mesh of points must be considered and the displacement must keep the isochoric constrain. In model A and in traditional FEM each point has three degrees of freedom, but the number of points is smaller in the former one. In numerical tests performed with bigger mesh resolutions, the accuracy of the results obtained with model A did not change appreciably.

Note that if the artery is stretched axially, it becomes stiffer (model B). Hence, the variation of the internal radius when the pressure changes, is smaller. Or, what is the same, keeping the pressure constant and stretching the artery axially, the radius decreases. Indeed, Table 3.3 shows the radius r_1 for two different values of

λ_z . The variation of r_1 is similar in the linear model A and in the nonlinear models B and C. Therefore, the axial forces as well as the radial deformations are alike.

Table 3.3: *Dependence of the internal radius r_1 on the axial stretch λ_z for a constant pressure equal to \bar{p}_{in} .*

model	$r_1(\lambda_z = 1)$	$r_1(\lambda_z = 1.01)$	Δr_1
A	1.5518 mm	1.5377 mm	-0.91%
B	1.5518 mm	1.5351 mm	-1.08%
C	1.5414 mm	1.5253 mm	-1.04%

3.4.2.3 Bending

Since the model is essentially a two dimensional mesh, it is important to examine deformations in the perpendicular direction. To this end, a planar slice of an artery with a rectangular shape is considered. The slice hangs from the two extremes and it is subjected to a uniform load (Fig. 3.11). The deflection v of a simply supported beam as a function of the distance z is [144]

$$v = -\frac{wz}{24EI}(L^3 - 2Lz^2 + z^3) \quad (3.46)$$

where $w = pW$ is the load per unit length, $EI = \bar{g}_z hW$ is the flexural rigidity, and L is the separation between the two supporting points. Furthermore, W and h represent the width and the height of the beam respectively.

The ET is not the same as in Section 3.4.1, because the artery is planar and no stress (internal pressure) deforms the artery at the onset. The spring stiffnesses now become $\kappa_\theta = 28.4$ N/m, $\kappa_z = 45.2$ N/m, $\kappa_d = 98.4$ N/m, $\zeta_\theta = 4.46$ μJ , and $\zeta_z = 7.64$ μJ (here τ is replaced by ζ_θ and ζ is replaced by ζ_z). Moreover, $\bar{g}_z = 21.4$ mN, $p = 200$ Pa, $h = 0.90$ mm, and $L = 8.72$ mm. Observe that L is shorter than the original length 8.90 mm of the artery when there is no bending.

The results of our numerical calculation and of the beam deflection are compared in Fig. 3.11. The modulus of the maximum deflection $\delta = |v|_{\text{max}}$ varies from 0.8145 mm in our calculation to 0.7795 mm using (3.46). The difference is only 4.5%, showing a fairly good agreement. Furthermore, as long as the distance between adjacent nodes is kept nearly constant (i.e. large κ_θ , κ_z , κ_d), the only relevant parameter in this deformation is ζ_z . For example, reducing κ_θ , κ_z , κ_d , and ζ_θ by a factor 2, but keeping the same value for ζ_z , the new value of δ is 0.8157 mm, i.e. it increases by 0.15%.

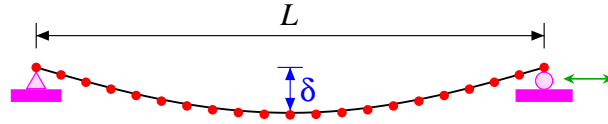


Figure 3.11: *Bending of a planar artery subjected to a uniform vertical load. The triangle and the circle at the ends support the artery vertically: the triangle is fixed but the circle can move freely in the horizontal direction (green arrows). The black curve represents Eq. (3.46) and the red points are the result of the calculations performed with the model developed in this work.*

3.4.3 Large Stretch

The artery deformations can be large [145] and since the model is nonlinear, it is significant to see how the ET depends on the stretches. Figure 3.12 shows the calculations for each tissue layer when the stretches λ_θ and λ_z vary between 1 and 1.1.

The largest increase of the ET components is found in the Intima layer (Fig. 3.12(d)), because it has the biggest constitutive parameter k_2 entering in the exponential of Eq. (3.2). In particular, the largest component is c_{zzzz} , which increases by a factor of 72.5 when $\lambda_z = 1 \rightarrow 1.1$. However, the most relevant dependence is on λ_θ , because λ_z is nearly constant in most artery deformations.

Observe that, in the shorter interval $1 < \lambda_\theta < 1.01$, the ET does not vary appreciably and the linear approximation can be used. The average stiffness μ of the tissues in the low loading domain (at which the noncollagenous matrix material is mainly active) is lower for the Media compared to the Adventitia [146]. According to Holzapfel et al. [127] the Intima is the stiffest layer over the whole deformation domain, whereas the Media is the softest in the axial direction.

Lastly, in Table 3.1 the angle ϕ between the tangential direction and the fiber reinforcement is smaller than 45° in the Media, so that $c_{\theta\theta\theta\theta} > c_{zzzz}$ (the red curve in Fig. 3.12 (b, e) is above the green curve). On the other hand, ϕ is larger than 45° in the Intima and in the Adventitia, so the opposite behavior is observed.

3.5 Conclusions

The artery model developed in this chapter is linear and two dimensional, which results in shorter PT. So, it is suitable for computing small and noninvasive artery deformations. Furthermore, it implicitly includes the individual characteristics and inhomogeneous properties of the artery layers. Some of the elasticity tensor components were obtained and a method to calculate the spring stiffnesses connecting the nodes of the mesh was described.

Three kinds of springs are used. The stiffnesses of the normal springs κ are derived by comparing the elastic energy stored in the springs and in the layers subjected to

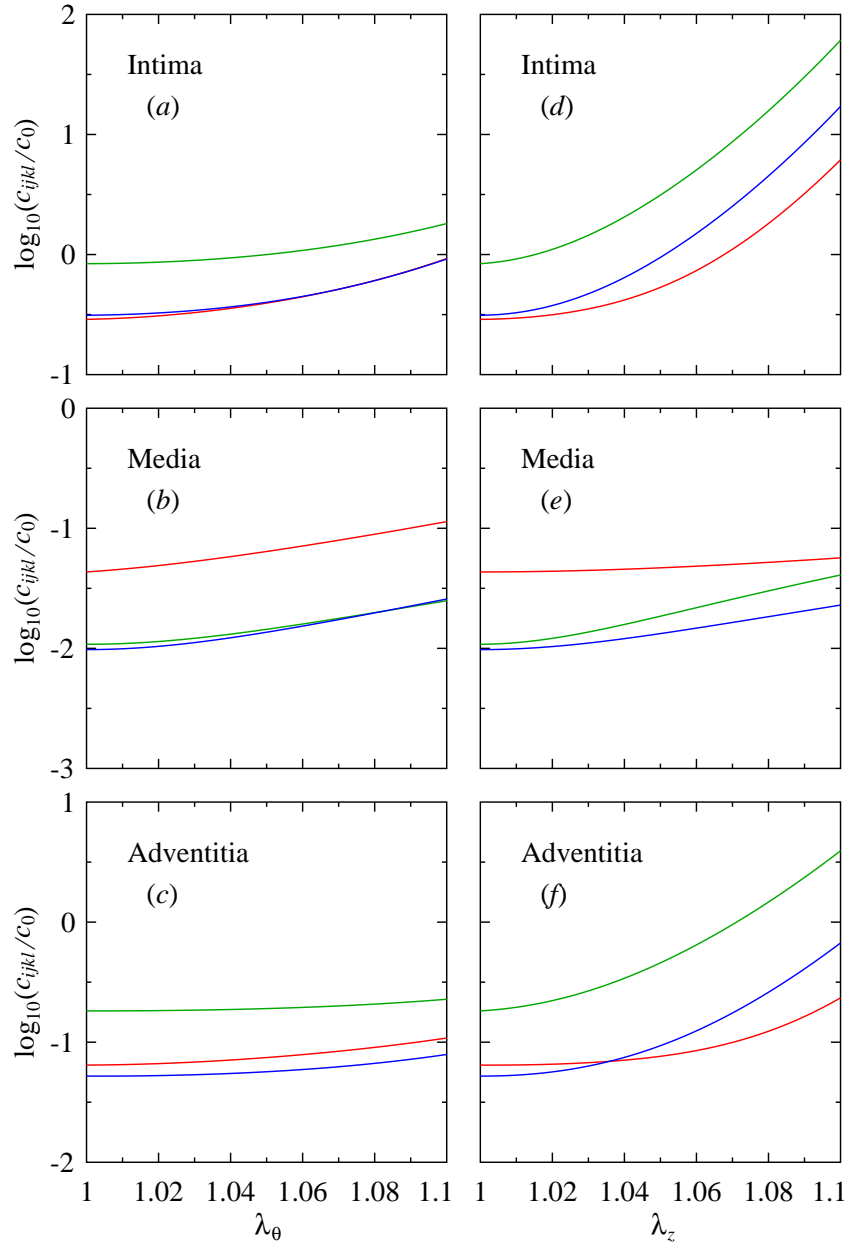


Figure 3.12: *Logarithm of the ET as function of the tangential stretch λ_θ (a, b, c) and of the axial stretch λ_z (d, e, f) in the interval $[1, 1.1]$. The constant c_0 is equal to 1 MPa. The different colors indicate the ET components $c_{\theta\theta\theta\theta}$ (red), c_{zzzz} (green), and $c_{\theta\theta zz}$ (blue). The results are given for the Intima (a, d), Media (b, e), and Adventitia (c, f) tissues.*

the same strain. The determination of the angular spring stiffnesses τ and ζ is carried out by comparing the energies when the tissues are bent. The resulting formulas are compact and the procedure was generalized in order to include geometries other

than the cylindrical.

The stiffness of the springs κ was analyzed for different mesh resolutions and artery sizes (radius r_1 and thickness h). Increasing the resolution, κ_i remain constant up to first order. If the ratio r_1/h does not vary, κ_i are proportional to r_1 . On the other hand, it becomes difficult to predict the behavior when r_1/h varies, because the strain inside the layer changes and the average elasticity tensor is a nonlinear function of the strain.

The method was validated by different loads. The first one evaluated the most relevant case, where the blood pressure inflates the artery, and the outcome was close to the nonlinear and incompressible artery, which was also modeled by plane strain FEM. When the artery is stretched by a small amount in the axial direction, the calculations with the models led to similar results. The nonlinear FEM is more accurate than our method, but its precision decreases if the symmetry is lowered. Furthermore, the angular springs are essential in the case that the structure undergoes bending deformations. Finally, the elasticity tensor strongly depends on the stretch, especially if the Intima layer is axially deformed. However, assuming a stretch variation smaller than 1%, the linear approximation is accurate.

Chapter 4

Simulator

4.1 State of the Art

In 2003 Konings et al. [64] proposed an analytical approximation to the problem of the wire. Their algorithm is highly generic and has good but slow convergence properties. It is based on quasi-static mechanics [147], which models the wire propagation without specific knowledge about friction forces. The motion is considered to be the result of a forced translation of the proximal wire body into the introduced sheath, effected by the physician. The translation is a stepwise process which calculates how the wire reacts to an introduction of a small wire segment, giving a new steady-state position. In 2007 Alderliesten et al. [49] improved the model, incorporating the friction between the wire and the vasculature.

The wire is similar to the model of the rope (knot) proposed by Brown et al. [148] and extended by Müller et al. [149] to simulate hair and fur. They apply the idea based on “Follow The Leader”, which is a purely geometrical technique where a chain of particles defines a curve representing a rope. Each particle moves towards its predecessor to enforce their mutual distance to be constant. The speed of the algorithm for computing the global shape of the rope saves time that can be used on the collision detection and on the management modules.

The Cosserat continuum theory of thin objects (shells, rods, and points) can be used to model the wire [150, 151]. Cao et al. [152] employed the Cosserat method to explore the nonplanar nonlinear dynamics of elastic rods. Later, Gao et al. [153] described the dynamic behavior of the wire with the Lagrange equations of motion and applied the penalty method to maintain the constraints. They proposed a simplified solving procedure to integrate the resulting equations more easily.

Another method to model the deformation of a wire or a similar body, is a representation based on the 3D beam theory [154]. The elementary stiffness matrix relates angular and spatial positions of each end of a beam element to the applied forces and torques. Duriez et al. [155] improved the accuracy and treat geometric non-linearities, while maintaining real-time computation. They considered a FEM approach and developed a new mathematical representation combined with an incremental technique, that allows for highly non-linear behavior. In particular, a new method is presented for correctly handling contact response in complex situations, where a large number of nodes are subject to non-holonomic constraints.

According to Coles et al. [11], some simulators also include interactive fluid dynamics of blood flow [156], volumetric contrast agent propagation, and real time collision detection and response [157]. Also, the artery deformation can be considered [158]. This problem was dealt in chapter 3, where some of the ET components were determined and, afterwards, the stiffness of the springs connecting the nodes were calculated. Current efforts are aimed towards integrating performance assessment and user guidance [34].

One of the most time consuming tasks in the simulation is the calculation of energy gradients in the PR. This problem has been addressed in chapter 2. In particular, an efficient collision-detection algorithm was developed based on space partitioning. Furthermore, a continuous vector field (modulus and direction) was

proposed, giving a realistic representation of the wire-surface interaction. On the other hand, Luboz et al. [159] introduced a simplified deformable vascular model, but it is not smooth and contains surface irregularities which affect the collision response.

Besides the virtual model, the simulator must capture the wire motion. The hardware can be built e.g. using an optical encoder [160] or a haptic device [159]. For instance, the Vascular Simulation Platform by Xitact is specifically designed to coaxially track a catheter and a wire. However, these solutions are expensive and difficult to assemble.

A promising surgery technique uses teleoperation [161]. This technique protects the physician from X-ray radiation and solves the problem of lack of experienced physicians in remote areas [162]. The slave manipulator detects the force of a catheter being inserted into the blood vessels. Then the master manipulator produces an equal damping force based on magnetorheological fluids [163]. Since VRS is similar to teleoperation, any progress made on one front can contribute to the other one.

4.2 Methods

The model of Konings et al. [64] considers the wire as a discrete set of joints at positions $\mathbf{x}_0, \dots, \mathbf{x}_n$, with \mathbf{x}_0 fixed. There are n segments and the i -th segment $\boldsymbol{\lambda}_i = \mathbf{x}_i - \mathbf{x}_{i-1}$ is represented by a small rigid rod which is neither compressible nor bendable. Further, the size $|\boldsymbol{\lambda}_i|$ is the same for all segments [164].

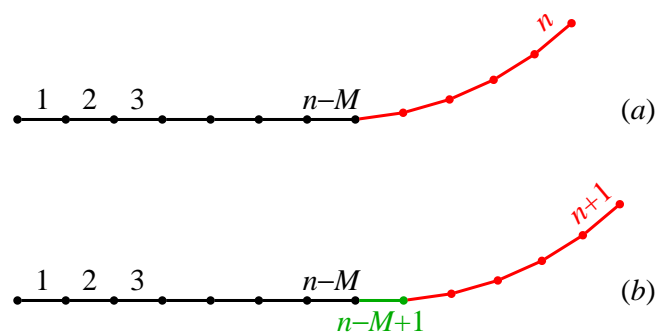


Figure 4.1: (a) The wire has a curved tip (red) with M segments. They are numbered from the proximal end to the distal end of the wire. (b) The new segment (green) points to the same direction as the segment number $n - M$, and the total number increases to $n + 1$.

When parts of the wire are inserted into the vessel, the current representation is adapted by adding segments and computing a new configuration with an optimization algorithm (relaxations). Pushing the wire into the vessel mainly affects its end, while the rest of the scene looks almost static. Hence, the natural way to add a new segment is to introduce it just before the curved tip, with the same orientation as

the previous segment (Fig. 4.1). The wire can also be rotated but this action affects only the tip which is intrinsically curved.

In Sections 4.2.1 and 4.2.2, two different and complementary methods are explained to implement the relaxation. The combination of both methods is shown in Section 4.2.3. In addition, Section 4.2.4 presents a hardware which can be used to build this simulator.

4.2.1 Physical Relaxation

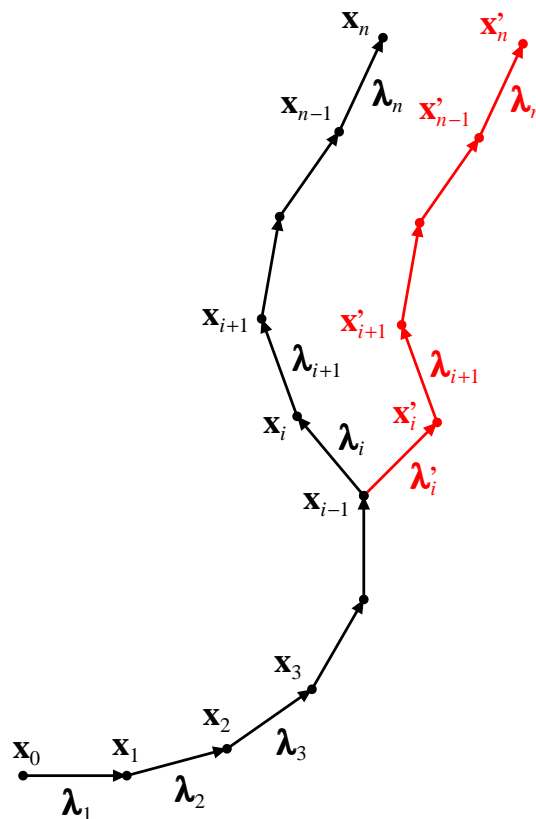


Figure 4.2: *The wire geometry. The difference between the coordinates of two consecutive joints $\mathbf{x}_j - \mathbf{x}_{j-1}$ is equal to the vector $\boldsymbol{\lambda}_j$, which has a constant length λ . Changing $\boldsymbol{\lambda}_i$ modifies only $\mathbf{x}_i, \mathbf{x}_{i+1}, \dots, \mathbf{x}_{n-1}, \mathbf{x}_n$, and the difference between the new and the old coordinates $\mathbf{x}'_j - \mathbf{x}_j = \boldsymbol{\lambda}'_j - \boldsymbol{\lambda}_j$ is the same for $j = i, i + 1, \dots, n - 1, n$.*

Figure 4.2 illustrates the wire geometry. Since

$$\mathbf{x}_j = \mathbf{x}_0 + \sum_{k=1}^j \boldsymbol{\lambda}_k$$

updating the i -th segment $\boldsymbol{\lambda}_i$ influences the joints from \mathbf{x}_i up to \mathbf{x}_n . For this reason,

more relaxations are needed close to the distal end of the wire. A PR cycle is defined to be the sequence of n iterations

- iteration 1: update segment n ,
- iteration 2: update segments $n, n - 1$,
- iteration 3: update segments $n, n - 1, n - 2$,
- \vdots
- iteration n : update segments $n, n - 1, \dots, 2, 1$.

The algorithm of Konings et al. [64] also proceeds from the distal end to the proximal end. The total number of updates in one cycle equals $\frac{1}{2}n(n + 1)$.

To ensure numerical stability, every time an ‘‘action’’ is performed (add a segment, remove a segment, or rotate the wire) a Tip Relaxation is executed:

1. A number of $\frac{1}{2}m(m + 1)$ updates (corresponding to the first m iterations) is carried out. Thus, the m segments closest to the tip are always updated. Since the actions take place just before the curved tip (Fig. 4.1), m is chosen as $M + 5$ to ensure that all affected segments will be updated at least five times before a new action is performed. However, if the wire is very stiff, then it is necessary to replace 5 by a bigger number.
2. Additionally, one update is executed for the segment numbers $n - m - 5, n - m - 10, n - m - 15, \dots$ up to the proximal end of the wire. This ensures some degree of relaxation besides the tip. Otherwise, if a large number of actions performed in a short time interval, the rest of the wire would be far away from equilibrium.

The numerical performance can be increased if incomplete cycles are carried out, i.e. some of the last iterations [49] are suppressed. In what follows, the physical model of the wire is improved and an updating recipe is given, which is simpler to apply than the recipe of Konings et al. [64].

4.2.1.1 Bending Energy

Consider the bending energy U_i of a wire segment (an arc) defined by three points \mathbf{x}_{i-1} , \mathbf{x}_i , and \mathbf{x}_{i+1} (Fig. 4.3)

$$U_i = \frac{1}{2} \frac{EI_i}{R_i^2} s_i \quad (4.1)$$

where EI_i represents the flexural rigidity, R_i is the radius, and $s_i = R_i\theta_i$ is the arc length between \mathbf{x}_{i-1} and \mathbf{x}_i (or equivalently between \mathbf{x}_i and \mathbf{x}_{i+1}). Note that U_i does not represent the elastic energy between the points \mathbf{x}_{i-1} and \mathbf{x}_{i+1} , but only half of this arc.

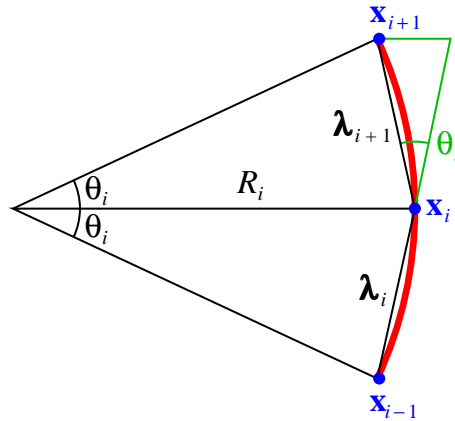


Figure 4.3: Three successive points \mathbf{x}_{i-1} , \mathbf{x}_i , and \mathbf{x}_{i+1} separated by an equal distance $\lambda = |\boldsymbol{\lambda}_i| = |\boldsymbol{\lambda}_{i+1}|$ define a circular arc of radius R_i and angle $2\theta_i$.

From Fig. 4.3 it follows that the distance between two points is given by $\lambda = 2R_i \sin(\theta_i/2)$. Hence Eq. (4.1) can be put in the form

$$U_i = \frac{EI_i}{2R_i} \theta_i = \frac{EI_i}{\lambda} \theta_i \sin \frac{\theta_i}{2} \quad (4.2)$$

For $\theta_i \ll 1$ the last equation reduces to Eq. (3) of Alderliesten et al. [12]

$$U_i = \frac{1}{2} \frac{EI_i}{\lambda} \theta_i^2$$

The angle θ_i can be calculated using the formula $\cos \theta_i = \boldsymbol{\lambda}_i \cdot \boldsymbol{\lambda}_{i+1} / \lambda^2$. If the wire is intrinsically curved at joint i , then $\boldsymbol{\lambda}_{i+1}$ must be replaced by $\mathbf{x}_{i+1} - \mathbf{x}_i - \boldsymbol{\omega}_{i+1}$ (Fig. 4.4). Further, rotating the wire changes the orientation of $\boldsymbol{\omega}_{i+1}$. Since

$$\theta \sin \frac{\theta}{2} \approx (1 - \cos \theta) + \frac{1}{12} (1 - \cos \theta)^2 + \frac{3}{1280} \theta^6 \quad (4.3)$$

up to fourth order in θ_i

$$\begin{aligned} U_i(\boldsymbol{\lambda}_i, \boldsymbol{\lambda}_{i+1}) &= \frac{EI_i}{12\lambda} [13 - 14 \cos \theta_i + \cos^2 \theta_i] \\ &= \frac{C_i}{12} \left[13 - 14 \frac{\boldsymbol{\lambda}_i \cdot \boldsymbol{\lambda}_{i+1}}{\lambda^2} + \frac{(\boldsymbol{\lambda}_i \cdot \boldsymbol{\lambda}_{i+1})^2}{\lambda^4} \right] \end{aligned} \quad (4.4)$$

where $C_i = EI_i/\lambda$ is a springs constant.

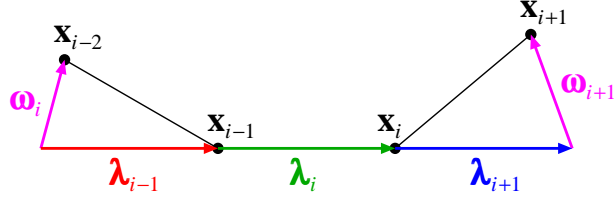


Figure 4.4: The minimum energy of a wire without external forces results when λ_{i-1} is parallel to λ_i , and λ_i is parallel to λ_{i+1} . If $\lambda_{i-1} = \mathbf{x}_{i-1} - \mathbf{x}_{i-2} + \boldsymbol{\omega}_i$, $\lambda_i = \mathbf{x}_i - \mathbf{x}_{i-1}$, and $\lambda_{i+1} = \mathbf{x}_{i+1} - \mathbf{x}_i - \boldsymbol{\omega}_{i+1}$, then the equilibrium is obtained when \mathbf{x}_{i-2} , \mathbf{x}_{i-1} , \mathbf{x}_i , and \mathbf{x}_{i+1} are in the positions indicated. Thus, the vectors $\boldsymbol{\omega}_i$ bend a free wire.

4.2.1.2 Energy Minimization

The orientation of the i -th segment is updated ($\lambda_i \rightarrow \lambda_i + \alpha_i$) while the others λ_j are kept constant, in such a way that the energy decreases. The energy variation of $U_i(\lambda_i + \alpha_i, \lambda_{i+1})$ around the new position $\lambda_i + \alpha_i \rightarrow \lambda_i + \alpha_i + \delta\alpha_i$ is up to first order

$$\delta U_i(\lambda_i + \alpha_i, \lambda_{i+1}) = \frac{C_i}{6\lambda^2} \left[-7 + \frac{\lambda_{i+1} \cdot \lambda_i + \lambda_{i+1} \cdot \alpha_i}{\lambda^2} \right] \lambda_{i+1} \cdot \delta\alpha_i \quad (4.5a)$$

Furthermore, U_{i-1} also varies

$$\delta U_{i-1}(\lambda_{i-1}, \lambda_i + \alpha_i) = \frac{C_i}{6\lambda^2} \left[-7 + \frac{\lambda_{i-1} \cdot \lambda_i + \lambda_{i-1} \cdot \alpha_i}{\lambda^2} \right] \lambda_{i-1} \cdot \delta\alpha_i \quad (4.5b)$$

Similarly, if the wire is intrinsically curved at joint $i-1$, then λ_{i-1} must be replaced by $\mathbf{x}_{i-1} - \mathbf{x}_{i-2} + \boldsymbol{\omega}_i$ (Fig. 4.4).

It is convenient to introduce the vectors $\hat{\mathbf{u}}_i$, $\boldsymbol{\eta}_i$, $\boldsymbol{\varepsilon}_i$, and the scalar κ_i defined by

$$\begin{aligned} \hat{\mathbf{u}}_i &= \lambda_i / \lambda \\ \boldsymbol{\eta}_i &= \hat{\mathbf{u}}_{i-1} - \hat{\mathbf{u}}_i \\ \boldsymbol{\varepsilon}_i &= \hat{\mathbf{u}}_{i+1} - \hat{\mathbf{u}}_i \\ \kappa_i &= \hat{\mathbf{u}}_i \cdot \hat{\mathbf{u}}_{i+1} \end{aligned} \quad (4.6)$$

The elastic energy variation of the wire is the sum of Eqs. (4.5a) and (4.5b)

$$\delta U_{\text{elas}} = -\frac{C_i}{\lambda} \left[(p_i + q_i) \hat{\mathbf{u}}_i + p_i \boldsymbol{\eta}_i + q_i \boldsymbol{\varepsilon}_i \right] \cdot \delta\alpha_i \quad (4.7)$$

with

$$\begin{aligned} p_i &= \frac{1}{6} \left[7 - \kappa_{i-1} - (\hat{\mathbf{u}}_i + \boldsymbol{\eta}_i) \cdot \frac{\boldsymbol{\alpha}_i}{\lambda} \right] \approx \frac{7 - \kappa_{i-1}}{6} \\ q_i &= \frac{1}{6} \left[7 - \kappa_i - (\hat{\mathbf{u}}_i + \boldsymbol{\varepsilon}_i) \cdot \frac{\boldsymbol{\alpha}_i}{\lambda} \right] \approx \frac{7 - \kappa_i}{6} \end{aligned} \quad (4.8)$$

because $\kappa_i \lesssim 1$ and $|\boldsymbol{\alpha}_i| \ll \lambda$ for small corrections (i.e. nearby equilibrium).

Usually, the artery deformations caused by the wire are tiny [165], so that close to equilibrium the relation between stress and strain is linear. Changing $\boldsymbol{\lambda}_i + \boldsymbol{\alpha}_i$ by $\delta\boldsymbol{\alpha}_i$ affects the coordinates $\mathbf{x}_i, \dots, \mathbf{x}_n$ by the same amount. Hence, due to the interactions between the wire and the artery, the surface energy also varies $\delta U_{\text{surf}} = \mathbf{G}_i \cdot \delta\boldsymbol{\alpha}_i$. Here \mathbf{G}_i stands for the sum of the gradients from joint i up to the distal end of the wire [12]

$$\mathbf{G}_i = \sum_{j=i}^n \nabla_j U_{\text{surf}}(\mathbf{x}_j) \quad (4.9)$$

where $U_{\text{surf}}(\mathbf{x}_j)$ represents energy interaction of joint j with the artery's surface.

The total energy variation is

$$\begin{aligned} \delta U &= \left[-\frac{C_i}{\lambda} (p_i + q_i) \hat{\mathbf{u}}_i - \frac{C_i}{\lambda} (p_i \boldsymbol{\eta}_i + q_i \boldsymbol{\varepsilon}_i) + \mathbf{G}_i \right] \cdot \delta\boldsymbol{\alpha}_i \\ &= \left[(B_{\text{ui}} - \rho_i) \hat{\mathbf{u}}_i + B_{\text{vi}} \hat{\mathbf{v}}_i + B_{\text{wi}} \hat{\mathbf{w}}_i \right] \cdot \delta\boldsymbol{\alpha}_i \end{aligned} \quad (4.10)$$

where $\hat{\mathbf{v}}_i$ and $\hat{\mathbf{w}}_i$ are two unit vectors perpendicular to $\hat{\mathbf{u}}_i$, i.e. the set $\{\hat{\mathbf{u}}_i, \hat{\mathbf{v}}_i, \hat{\mathbf{w}}_i\}$ forms an orthonormal basis with $\hat{\mathbf{u}}_i$ parallel to $\boldsymbol{\lambda}_i$. Furthermore,

$$\begin{aligned} \rho_i &= \frac{C_i}{\lambda} (p_i + q_i) \\ \mathbf{B}_i &= \mathbf{G}_i - \frac{C_i}{\lambda} (p_i \boldsymbol{\eta}_i + q_i \boldsymbol{\varepsilon}_i) \end{aligned} \quad ((4.10)')$$

and $B_{\text{ui}} = \mathbf{B}_i \cdot \hat{\mathbf{u}}_i$, $B_{\text{vi}} = \mathbf{B}_i \cdot \hat{\mathbf{v}}_i$, $B_{\text{wi}} = \mathbf{B}_i \cdot \hat{\mathbf{w}}_i$.

Since the modulus of $\boldsymbol{\lambda}_i + \boldsymbol{\alpha}_i$ remains constant, it follows that $|\boldsymbol{\lambda}_i + \boldsymbol{\alpha}_i|^2 = \lambda^2$ or $2\boldsymbol{\lambda}_i \cdot \boldsymbol{\alpha}_i = -|\boldsymbol{\alpha}_i|^2$. Thus, $\boldsymbol{\alpha}_i$ can be written in the form (Fig. 4.5)

$$\boldsymbol{\alpha}_i = -\frac{a_i^2}{2\lambda} \hat{\mathbf{u}}_i + H(a_i) (\cos \psi_i \hat{\mathbf{v}}_i + \sin \psi_i \hat{\mathbf{w}}_i) \quad (4.11)$$

with

$$H(a_i) = \frac{a_i}{2\lambda} \sqrt{4\lambda^2 - a_i^2} \quad ((4.11)')$$

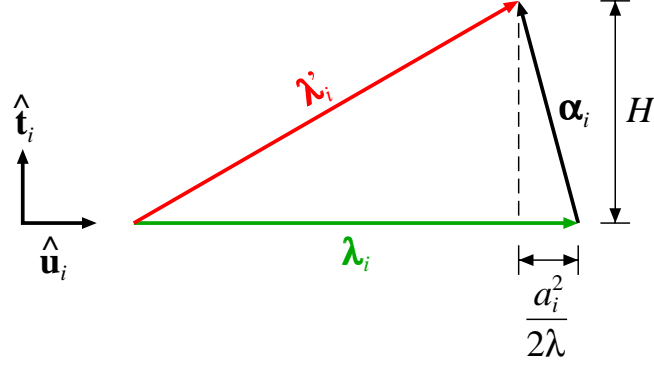


Figure 4.5: The lengths of the vectors λ_i (old), λ'_i (new) are equal, and the modulus of $\alpha_i = \lambda'_i - \lambda_i$ is a_i . Further, the unit vector \hat{u}_i is parallel to λ_i and perpendicular to $\hat{t}_i = \cos \psi_i \hat{v}_i + \sin \psi_i \hat{w}_i$, where ψ_i represents the azimuthal angle of α_i around λ_i .

Any variation of α_i can be expressed using the parameters a_i and ψ_i

$$\begin{aligned} \delta \alpha_i = & \left[-\frac{a_i}{\lambda} \hat{u}_i + \frac{dH}{da_i} (\cos \psi_i \hat{v}_i + \sin \psi_i \hat{w}_i) \right] \delta a_i \\ & + H(a_i) (-\sin \psi_i \hat{v}_i + \cos \psi_i \hat{w}_i) \delta \psi_i \end{aligned} \quad (4.12)$$

At the minimum, $\delta U = 0$ for arbitrary δa_i and $\delta \psi_i$. Considering first the case $\delta a_i = 0$ and $\delta \psi_i \neq 0$

$$\left[-B_{\mathbf{v}i} \sin \psi_i + B_{\mathbf{w}i} \cos \psi_i \right] H(a_i) \delta \psi_i = 0$$

from which it is deduced that $B_{\mathbf{w}i} \cos \psi_i = B_{\mathbf{v}i} \sin \psi_i$. Hence

$$\cos \psi_i \hat{v}_i + \sin \psi_i \hat{w}_i = \frac{B_{\mathbf{v}i} \hat{v}_i + B_{\mathbf{w}i} \hat{w}_i}{\sqrt{B_{\mathbf{v}i}^2 + B_{\mathbf{w}i}^2}} \quad (4.13)$$

Now, the case $\delta a_i \neq 0$ and $\delta \psi_i = 0$ is examined. From Eq. ((4.11)')

$$\frac{dH}{da_i} = \frac{d}{da_i} \left(a_i - \frac{a_i^3}{8\lambda^2} + \dots \right) = 1 - \frac{3a_i^2}{8\lambda^2} + \dots$$

so that up to first order in a_i/λ Eq. (4.12) becomes

$$\delta \alpha_i = \left[-\frac{a_i}{\lambda} \hat{u}_i + \frac{B_{\mathbf{v}i} \hat{v}_i + B_{\mathbf{w}i} \hat{w}_i}{\sqrt{B_{\mathbf{v}i}^2 + B_{\mathbf{w}i}^2}} \right] \delta a_i$$

where Eq. (4.13) has been used. Therefore Eq. (4.10) gives

$$\left[-\frac{a_i}{\lambda}(B_{\mathbf{u}i} - \rho_i) + \sqrt{B_{\mathbf{v}i}^2 + B_{\mathbf{w}i}^2} \right] \delta a_i = 0 \quad (4.14)$$

and solving

$$a_i = \lambda \frac{\sqrt{B_{\mathbf{v}i}^2 + B_{\mathbf{w}i}^2}}{B_{\mathbf{u}i} - \rho_i} \quad (4.15)$$

Note that changing the sign of Eq. (4.13) as in the work of Alderliesten et al. [12], also changes the sign of a_i in the last equation. Since $H(a_i)$ is an odd function, the product $H(a_i)(\cos \psi_i \hat{\mathbf{v}}_i + \sin \psi_i \hat{\mathbf{w}}_i)$ is the same irrespective of the chosen sign.

4.2.1.3 First Order Correction

Because the norm of the vector $\boldsymbol{\lambda}_i$ remains constant, only the change of direction needs to be updated in the calculations: $\hat{\mathbf{u}}_i \rightarrow \hat{\mathbf{u}}_i + \Delta \hat{\mathbf{u}}_i = \hat{\mathbf{u}}_i + \boldsymbol{\alpha}_i / \lambda$. In particular, note that for $a_i \ll \lambda$ Eq. (4.11) becomes

$$\boldsymbol{\alpha}_i \approx a_i (\cos \psi_i \hat{\mathbf{v}}_i + \sin \psi_i \hat{\mathbf{w}}_i) = \lambda \frac{B_{\mathbf{v}i} \hat{\mathbf{v}}_i + B_{\mathbf{w}i} \hat{\mathbf{w}}_i}{B_{\mathbf{u}i} - \rho_i}$$

or

$$\Delta \hat{\mathbf{u}}_i = \frac{\boldsymbol{\alpha}_i}{\lambda} \approx -\frac{\hat{\mathbf{u}}_i \times (\mathbf{B}_i \times \hat{\mathbf{u}}_i)}{\rho_i - \hat{\mathbf{u}}_i \cdot \mathbf{B}_i} \quad (4.16)$$

The scalar $\hat{\mathbf{u}}_i \cdot \mathbf{B}_i = B_{i\parallel}$ is the projection of \mathbf{B}_i along $\hat{\mathbf{u}}_i$ and $\hat{\mathbf{u}}_i \times (\mathbf{B}_i \times \hat{\mathbf{u}}_i) = \mathbf{B}_i - \hat{\mathbf{u}}_i (\hat{\mathbf{u}}_i \cdot \mathbf{B}_i) = \mathbf{B}_i - \mathbf{B}_{i\parallel} = \mathbf{B}_{i\perp}$ represents the component of \mathbf{B}_i perpendicular to $\hat{\mathbf{u}}_i$ (the infinitesimal variation of a vector with a constant modulus is perpendicular to the vector). Since $\Delta \hat{\mathbf{u}}_i$ is only an approximation, after updating $\hat{\mathbf{u}}_i$ a renormalization must be performed.

Mostly $\hat{\mathbf{u}}_i \cdot \mathbf{B}_i \ll \rho_i \sim 2C_i / \lambda$, so that from Eq. (4.16)

$$\Delta \hat{\mathbf{u}}_i \approx -\frac{\hat{\mathbf{u}}_i \times (\mathbf{B}_i \times \hat{\mathbf{u}}_i)}{\rho_i} \quad (4.17)$$

As ρ_i is nearly constant, to achieve equilibrium ($\Delta \hat{\mathbf{u}}_i \rightarrow 0$) the component of $\hat{\mathbf{u}}_i$ perpendicular to \mathbf{B}_i must be minimized. Notice that \mathbf{B}_i depends on \mathbf{G}_i , so that the calculation of \mathbf{G}_i plays a crucial role.

Suppose that all updates $\Delta \hat{\mathbf{u}}_i$ have nearly the same magnitude and are randomly oriented. As in random walks¹, the average distance covered by the tip when the segments between i and n are updated, is proportional to $\sqrt{n+1-i}$. Thus $|\mathbf{x}_{n,\text{new}} - \mathbf{x}_{n,\text{old}}|$ can become very large. To avoid this unstable behavior, the update is bounded

¹The expected translation distance after p steps varies as \sqrt{p} [166]

using the formula

$$|\Delta \hat{\mathbf{u}}_i| \leq \frac{\Delta u_{\max}}{\sqrt{n+1-i}} \quad (4.18)$$

where $i = 1, \dots, n$ and Δu_{\max} is small (~ 0.1). In a frontal collision of the wire with the surface, a single update can bend the tip at most by the amount Δu_{\max} . When the calculation proceeds, the next iterations will bend the tip further until $|\Delta \hat{\mathbf{u}}_i|$ naturally decreases and the wire approaches equilibrium.

The updates $\Delta \hat{\mathbf{u}}_i$ for small i are tiny, because they are bounded by Eq. (4.18). Hence, instabilities are dissipated and do not propagate to the proximal end of the wire. It is the tip of the wire (i close to n) which plays an important role in the simulation and, in this region, a higher number of updates is performed. Since the relaxation is stable, there is no need to introduce the segment in small steps as in the work of Alderliesten et al. [12], and it can be performed at once.

If $|\mathbf{B}_i| \ll \rho_i$ the update will be small. In this case, the denominator in Eq. (4.16) is positive and the update moves the wire in a direction so as to cancel \mathbf{B}_i . But in a frontal collision of the tip with the artery, \mathbf{B}_i can become very large because of \mathbf{G}_i . If the sign of the denominator is negative, \mathbf{B}_i will increase instead of canceling, and the calculations diverge. In particular, for $\rho_i - \hat{\mathbf{u}}_i \cdot \mathbf{B}_i \approx 0$ the modulus $|\alpha_i|$ becomes larger than 2λ , which is geometrically impossible. In such cases, the approximation $dH/da_i = 1$ fails.

To overcome this drawback, Eq. (4.14) should be considered without approximations

$$-\frac{a_i}{\lambda}(B_{\mathbf{u}i} - \rho_i) + \frac{2\lambda^2 - a_i^2}{\lambda\sqrt{4\lambda^2 - a_i^2}}\sqrt{B_{\mathbf{v}i}^2 + B_{\mathbf{w}i}^2} = 0$$

and solved numerically for a_i . However, a simple estimation for $\Delta \hat{\mathbf{u}}_i$ can be found. Taking the absolute value in the denominator of Eq. (4.16)

$$\Delta \hat{\mathbf{u}}_i = -\frac{\hat{\mathbf{u}}_i \times (\mathbf{B}_i \times \hat{\mathbf{u}}_i)}{|\rho_i - \hat{\mathbf{u}}_i \cdot \mathbf{B}_i|} \quad (4.19)$$

the update will always be in the right direction. Note that using Eq. (4.17) in place of Eq. (4.19) gives similar results. The magnitude of the correction can still be large, but since $|\Delta \hat{\mathbf{u}}_i|$ is bounded and $\hat{\mathbf{u}}_i$ is renormalized after each update, it poses no problem. Applying Eqs. (4.18) and (4.19) in the Tip Relaxation results in a stable algorithm even if, in a short time interval, a large number of actions are performed by the user.

Lastly, it is observed that Eq. (4.19) basically involves the calculation of \mathbf{B}_i and the computation of scalar and cross products with $\hat{\mathbf{u}}_i$. On the other hand, Eq. (11) of Alderliesten et al. [12] works implicitly with an orthonormal basis. It is necessary to calculate the projections of \mathbf{B}_i in this base, to determine the modulus a_i , the angle ψ_i , and then to construct the vector α_i again using the base. Thus, the method

developed in this work is simpler to apply.

4.2.1.4 Pseudocode

Algorithm 4.1: Pseudocode of the PR method. The entrance parameter is the segment i of the wire. The procedure updates the points \mathbf{x}_j and orientations $\boldsymbol{\omega}_j$ from $j = i$ up to the end of the wire $j = n$.

```

void PhysicalUpdate(segment  $i$ ) {
    1. calculate the gradient  $\mathbf{G}_i$ , see Eq. (4.9);
    2. calculate the update  $\Delta\hat{\mathbf{u}}_i$ , see Eqs. (4.18) and (4.19);
    3. update  $\hat{\mathbf{u}}_i$  and renormalize;
    4. update  $\mathbf{x}_i, \mathbf{x}_{i+1}, \dots, \mathbf{x}_n$ ;
    5. update  $\boldsymbol{\omega}_i, \boldsymbol{\omega}_{i+1}, \dots, \boldsymbol{\omega}_n$ ;
}

```

The pseudocode 4.1 implements the method described in this Section. Next, the PT spent in calling the procedure during a complete PR cycle is analyzed.

For a segment number i , the calculation of \mathbf{G}_i involves the collision test for $n - i$ segments. During the cycle of the PR, this procedure is called $\frac{1}{2}n(n + 1)$ times, and the total number of collision tests in one cycle is $\frac{1}{6}n(n + 1)(n + 2)$. If there is a collision for $j > i$, then $\nabla_j U_{\text{surf}}(\mathbf{x}_j)$ must be calculated. The number of times the gradient is computed depends on j . For example, if $j = n/2$ the computation is repeated $\frac{1}{8}n(n + 2) \approx n^2/8$ times, and in general it will be a fraction of n^2 . Thus, the PT of line **1** has the form $\frac{1}{6}n(n + 1)(n + 2)T_1 + n^2T_2$, where T_1 and T_2 are positive constants.

The lines **2** and **3** involve a single execution, so that the PT of one cycle is proportional to $\frac{1}{2}n(n + 1)$. Finally, lines **4** and **5** give a contribution similar to the number of collision tests executed, i.e. proportional to $\frac{1}{6}n(n + 1)(n + 2)$. Hence, the estimated PT of the physical update cycle is

$$\begin{aligned}
t_{\text{phy}} &= t_{\text{p1}}n + t_{\text{p2}}n^2 + t_{\text{p3}}n^3 \\
&\approx t_{\text{p2}}n^2 + t_{\text{p3}}n^3
\end{aligned} \tag{4.20}$$

In the last line, the PT is approximated by the two main contributions for large n .

Since Tip Relaxation plays a central role in the algorithm, its PT will also be examined. In the first part, when the first m segments are updated, the PT is similar to Eq. (4.20) but with $n \rightarrow m = M + 5$ (a constant). In the second part, when the segment numbers $n - m - 5, n - m - 10, n - m - 15, \dots$ are updated once, instead of $\frac{1}{2}n(n + 1)$ only $\sim (n - m)/5$ steps are executed. Hence, for large n

the term $n^2/2$ must be replaced by $n/5$ in Eq. (4.20). The overall result is

$$\begin{aligned} t_{\text{tip}} &\approx t_{\text{p1}}m + t_{\text{p2}}m^2 + t_{\text{p3}}m^3 + t_{\text{p3}}\left(\frac{2n}{5}\right)^{3/2} \\ &= \text{const} + t_{\text{p4}}n^{3/2} \end{aligned} \quad (4.21)$$

For example, if $m = 5 + 5$ and $n = 250$, then $m^3 = 1000 = (2n/5)^{3/2}$, i.e. the constant has the same order of magnitude as the last term in Eq. (4.21).

4.2.2 Geometrical Relaxation

Consider the problem of finding the minimum energy of a homogeneous wire ($EI = \text{const}$) with the following boundary conditions. The end points \mathbf{x}_μ and \mathbf{x}_ν are fixed as well as the tangent vectors to the trajectory $\dot{\mathbf{x}}_\mu$ and $\dot{\mathbf{x}}_\nu$ (the dot denotes differentiation with respect to the curve parameter τ). Between these points there is no contact with the surface and the total length of the curve is not fixed.

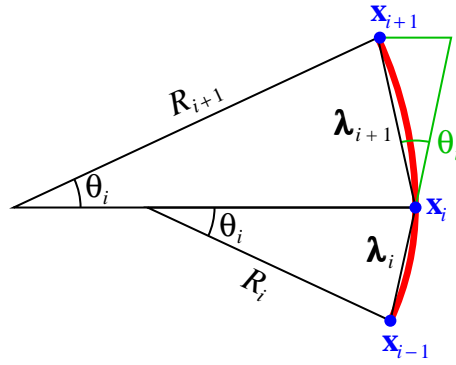


Figure 4.6: Three points \mathbf{x}_{i-1} , \mathbf{x}_i , and \mathbf{x}_{i+1} are separated by different distances $|\lambda_i| \neq |\lambda_{i+1}|$. The two circular arcs have the same angle θ_i but the radii R_i and R_{i+1} are not equal.

4.2.2.1 Bending Energy

Here, it is necessary to derive a generalization of Eq. (4.2) when the modulus $\lambda_i = |\lambda_i|$ is variable. In Fig. 4.6 the three points \mathbf{x}_{i-1} , \mathbf{x}_i , and \mathbf{x}_{i+1} are joined by two arcs having the same angle θ_i but different radii R_i and R_{i+1} . It is also possible to join the points using the same radius and different angles, but the calculations become cumbersome. The sum of the energies in half arc under and in half arc

above the point \mathbf{x}_i is

$$\begin{aligned} U_i &= \frac{1}{2} \frac{EI}{R_i^2} \frac{s_i}{2} + \frac{1}{2} \frac{EI}{R_{i+1}^2} \frac{s_{i+1}}{2} \\ &= \frac{EI}{2} \left(\frac{\theta_i}{2R_i} + \frac{\theta_i}{2R_{i+1}} \right) \\ &= \frac{EI}{2} \left(\frac{1}{\lambda_i} + \frac{1}{\lambda_{i+1}} \right) \theta_i \sin \frac{\theta_i}{2} \end{aligned}$$

because $\sin(\theta_i/2) = \lambda_i/2R_i = \lambda_{i+1}/2R_{i+1}$. Using Eq. (4.3) with $\cos \theta_i = \hat{\mathbf{u}}_i \cdot \hat{\mathbf{u}}_{i+1}$ results in

$$U_i = \frac{EI}{12} \left(\frac{1}{\lambda_i} + \frac{1}{\lambda_{i+1}} \right) \frac{13 - 14 \hat{\mathbf{u}}_i \cdot \hat{\mathbf{u}}_{i+1} + (\hat{\mathbf{u}}_i \cdot \hat{\mathbf{u}}_{i+1})^2}{2}$$

4.2.2.2 Energy Minimization

Since only λ_i and λ_{i+1} are functions of \mathbf{x}_i , it follows that U_{i-1} , U_i , and U_{i+1} depend on this coordinate. Omitting the constant multiplicative factor $EI/12$, it suffices to analyze the function

$$\begin{aligned} \Psi(\mathbf{x}_i) &= \left(\frac{1}{\lambda_{i-1}} + \frac{1}{\lambda_i} \right) \frac{13 - 14 \kappa_{i-1} + \kappa_{i-1}^2}{2} \\ &\quad + \left(\frac{1}{\lambda_i} + \frac{1}{\lambda_{i+1}} \right) \frac{13 - 14 \kappa_i + \kappa_i^2}{2} \\ &\quad + \left(\frac{1}{\lambda_{i+1}} + \frac{1}{\lambda_{i+2}} \right) \frac{13 - 14 \kappa_{i+1} + \kappa_{i+1}^2}{2} \end{aligned} \quad (4.22)$$

Notice that Ψ does not contain any physical parameter and depends solely on the geometry.

The label $*$ will be used to refer to the coordinates of the improved curve. In order to minimize Ψ , substitute \mathbf{x}_i^* by $\mathbf{x}_i^* + y_i \hat{\mathbf{y}}_i + z_i \hat{\mathbf{z}}_i$, where $\hat{\mathbf{y}}_i$ and $\hat{\mathbf{z}}_i$ are orthogonal to the vector $\mathbf{x}_{i+1} - \mathbf{x}_{i-1}$. The calculation of y_i and z_i can be carried out using the Hessian matrix and the gradient

$$\begin{pmatrix} \Psi_{yy,i} & \Psi_{yz,i} \\ \Psi_{yz,i} & \Psi_{zz,i} \end{pmatrix} \begin{pmatrix} y_i \\ z_i \end{pmatrix} = - \begin{pmatrix} \hat{\mathbf{y}}_i \cdot \nabla_i \Psi \\ \hat{\mathbf{z}}_i \cdot \nabla_i \Psi \end{pmatrix} \quad (4.23)$$

The Hessian matrix gives essentially a *metric* to find the length of the update $|\mathbf{x}_{i,\text{new}}^* - \mathbf{x}_{i,\text{old}}^*|$ in the *Newton* direction of steepest descent [167]. This direction is determined by the negative components of the gradient in the plane defined by $\hat{\mathbf{y}}_i$ and $\hat{\mathbf{z}}_i$. Near the minimum, the Hessian approaches a constant [168]. Thus, the

matrix elements can be computed numerically

$$\begin{aligned}
\Psi_{yy,i} &= \frac{1}{(\delta\lambda)^2} \left[\Psi(\mathbf{x}_i^* + \delta\lambda \hat{\mathbf{y}}_i) - 2\Psi(\mathbf{x}_i^*) + \Psi(\mathbf{x}_i^* - \delta\lambda \hat{\mathbf{y}}_i) \right] \\
\Psi_{yz,i} &= \frac{1}{4(\delta\lambda)^2} \left[\Psi(\mathbf{x}_i^* + \delta\lambda \hat{\mathbf{y}}_i + \delta\lambda \hat{\mathbf{z}}_i) \right. \\
&\quad - \Psi(\mathbf{x}_i^* + \delta\lambda \hat{\mathbf{y}}_i - \delta\lambda \hat{\mathbf{z}}_i) \\
&\quad - \Psi(\mathbf{x}_i^* - \delta\lambda \hat{\mathbf{y}}_i + \delta\lambda \hat{\mathbf{z}}_i) \\
&\quad \left. + \Psi(\mathbf{x}_i^* - \delta\lambda \hat{\mathbf{y}}_i - \delta\lambda \hat{\mathbf{z}}_i) \right] \\
\Psi_{zz,i} &= \frac{1}{(\delta\lambda)^2} \left[\Psi(\mathbf{x}_i^* + \delta\lambda \hat{\mathbf{z}}_i) - 2\Psi(\mathbf{x}_i^*) + \Psi(\mathbf{x}_i^* - \delta\lambda \hat{\mathbf{z}}_i) \right]
\end{aligned} \tag{4.23a}$$

where $\delta\lambda = \lambda/10^4$ for calculations performed with double precision.

On the other hand, the gradient is very sensitive to numerical round off errors near the minimum. Hence $\nabla_i \Psi$ must be determined analytically with the help of $\nabla_i \lambda_{i-1}^* = \mathbf{0}$, $\nabla_i \lambda_i^* = \hat{\mathbf{u}}_i^*$, $\nabla_i \lambda_{i+1}^* = -\hat{\mathbf{u}}_{i+1}^*$, $\nabla_i \lambda_{i+2}^* = \mathbf{0}$, and

$$\begin{aligned}
\nabla_i \kappa_{i-1}^* &= \frac{\hat{\mathbf{u}}_{i-1}^* - \kappa_{i-1}^* \hat{\mathbf{u}}_i^*}{\lambda_i^*} \\
\nabla_i \kappa_i^* &= \frac{\hat{\mathbf{u}}_{i+1}^* - \kappa_i^* \hat{\mathbf{u}}_i^*}{\lambda_i^*} - \frac{\hat{\mathbf{u}}_i^* - \kappa_i^* \hat{\mathbf{u}}_{i+1}^*}{\lambda_{i+1}^*} \\
\nabla_i \kappa_{i+1}^* &= -\frac{\hat{\mathbf{u}}_{i+2}^* - \kappa_{i+1}^* \hat{\mathbf{u}}_{i+1}^*}{\lambda_{i+1}^*}
\end{aligned} \tag{4.23b}$$

The minimization update is executed for the sequence $i = \mu + 1, \mu + 2, \dots, \nu - 1$, which is defined to be an iteration in the GR cycle. After repeating $\sim \nu - \mu$ times the iteration, the modulus of $\nabla_i \Psi$ is reduced by a considerable amount, i.e. the curve approaches the desired solution. Hence, one GR cycle consists of $\nu - \mu$ iterations, which has $(\nu - \mu)(\nu - \mu - 1) \approx (\nu - \mu)^2$ minimization updates.

Observe that the vectors $\hat{\mathbf{y}}_i$ and $\hat{\mathbf{z}}_i$ are calculated only at the beginning of the minimization procedure. Since the plane over which the point \mathbf{x}_i^* can move is kept constant, the possibility $\lambda_i^* \rightarrow \mathbf{0}$ is ruled out and numerical instabilities are avoided.

4.2.2.3 Point Slide

After executing the energy minimization, the point must be shifted ($\mathbf{x}_i^* \rightarrow \mathbf{x}'_i$) to restore $|\lambda'_i| = \lambda$. Specifically, \mathbf{x}'_i is displaced following the polyline to obtain $|\mathbf{x}'_i - \mathbf{x}'_{i-1}| = \lambda$ as depicted in Fig. 4.7(a), an idea which is based on the ‘‘Follow The Leader’’ technique [149].

To find \mathbf{x}'_j explicitly, consider Fig. 4.7(b). Let \mathbf{x}_{i-1}^* and \mathbf{x}_i^* be two vertices in the polyline such that $|\mathbf{x}_{i-1}^* - \mathbf{x}'_{j-1}| < \lambda$ and $|\mathbf{x}_i^* - \mathbf{x}'_{j-1}| > \lambda$. Then construct the vector

$$\mathbf{b}_{ij} = \hat{\mathbf{u}}_i^* \times \left[(\mathbf{x}_{i-1}^* - \mathbf{x}'_{j-1}) \times \hat{\mathbf{u}}_i^* \right] \tag{4.24}$$

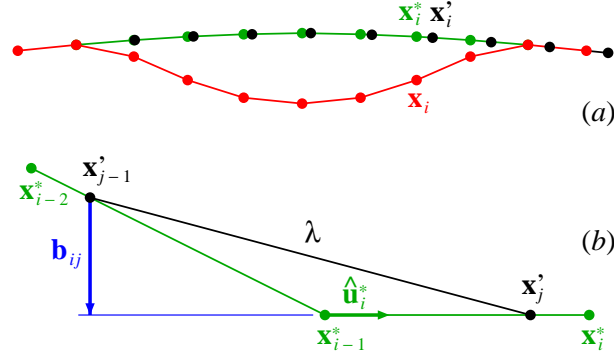


Figure 4.7: (a) Original curve \mathbf{x}_i (red), curve after executing the energy minimization \mathbf{x}_i^* (green), and displaced points \mathbf{x}_i' (black). (b) Closer view of three coordinates \mathbf{x}_{i-2}^* , \mathbf{x}_{i-1}^* , and \mathbf{x}_i^* after the minimization. The unit vector $\hat{\mathbf{u}}_i^*$ points from \mathbf{x}_{i-1}^* to \mathbf{x}_i^* , and the vector \mathbf{b}_{ij} goes from \mathbf{x}_{j-1}' to the line passing through \mathbf{x}_{i-1}^* and \mathbf{x}_i^* . The distance between \mathbf{x}_{j-1}' and \mathbf{x}_j' equals λ .

The j -th coordinate is calculated with the formula

$$\mathbf{x}'_j = \mathbf{x}'_{j-1} + \mathbf{b}_{ij} + \hat{\mathbf{u}}_i^* \sqrt{\lambda^2 - |\mathbf{b}_{ij}|^2} \quad (4.25)$$

In particular, at the beginning $\mathbf{x}'_\mu = \mathbf{x}_\mu$.

The previous displacement is performed using a linear interpolation between \mathbf{x}_{i-1}^* and \mathbf{x}_i^* . It is not difficult to find a second order correction for the interpolated point \mathbf{x}'_j . This procedure is illustrated in Fig. 4.8: the point \mathbf{x}'_j is displaced in the direction of the unit vector $\hat{\mathbf{e}}_i^*$ which is perpendicular to $\mathbf{x}_i^* - \mathbf{x}_{i-1}^* = \boldsymbol{\lambda}_i^* = \lambda_i^* \hat{\mathbf{u}}_i^*$. In order to find a formula for $\hat{\mathbf{e}}_i^*$, let $\hat{\mathbf{v}}_{i-}^*$ and $\hat{\mathbf{v}}_{i+}^*$ be two vectors parallel to $\hat{\mathbf{u}}_{i-1}^* \times \hat{\mathbf{u}}_i^*$ and $\hat{\mathbf{u}}_i^* \times \hat{\mathbf{u}}_{i+1}^*$ respectively. Then $\hat{\mathbf{e}}_i^*$ is chosen to point in the direction $\hat{\mathbf{u}}_i^* \times (\hat{\mathbf{v}}_{i-}^* + \hat{\mathbf{v}}_{i+}^*)$. Notice that $\hat{\mathbf{e}}_i^*$ lies in the average of the planes specified by $\hat{\mathbf{u}}_{i-1}^*$, $\hat{\mathbf{u}}_i^*$ and by $\hat{\mathbf{u}}_i^*$, $\hat{\mathbf{u}}_{i+1}^*$. But if $\hat{\mathbf{v}}_{i-}^* \cdot \hat{\mathbf{v}}_{i+}^* \leq 0$ it is not convenient to perform the second order correction, because the curve has an *inflection* and the circumference in Fig. 4.8 is no longer a good approximation.

To determine the length ε_{ij} of the displacement, first calculate the radius of the circumference

$$R_i^* = \frac{\lambda_i^*}{2 \sin(\bar{\theta}_i^*/2)} = \frac{\lambda_i^*}{\sqrt{2 - 2 \cos \bar{\theta}_i^*}}$$

The cosine of the angle $\bar{\theta}_i^*$ can be found with the dot product $\hat{\mathbf{u}}_{i-1}^* \cdot \hat{\mathbf{u}}_i^*$ or $\hat{\mathbf{u}}_i^* \cdot \hat{\mathbf{u}}_{i+1}^*$. In general, these products will be different and $\cos \bar{\theta}_i^*$ is set equal to the mean value.

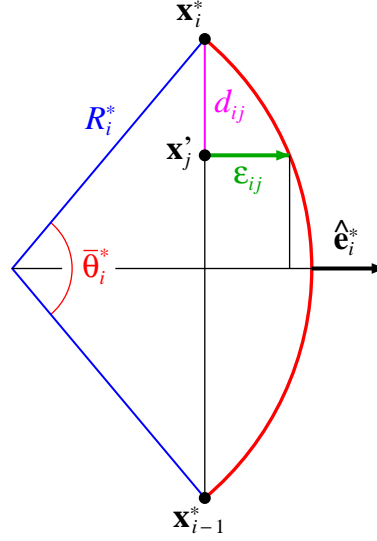


Figure 4.8: Second order correction $\varepsilon_{ij}\hat{e}_i^*$ to the coordinate \mathbf{x}_j' . The displacement is indicated by the green arrow. The arc segment has an angle $\bar{\theta}_i^*$ and a radius R_i^* . The distance between \mathbf{x}_{i-1}^* and \mathbf{x}_i^* is λ_i^* , and the distance between \mathbf{x}_j' and \mathbf{x}_i^* is d_{ij} .

Then the radius becomes

$$R_i^* = \frac{\lambda_i^*}{\sqrt{2 - \hat{\mathbf{u}}_i^* \cdot (\hat{\mathbf{u}}_{i-1}^* + \hat{\mathbf{u}}_{i+1}^*)}} \quad (4.26)$$

Let d_{ij} be the distance between \mathbf{x}_i and \mathbf{x}_j' . From Fig. 4.8 it is inferred that

$$\varepsilon_{ij} = \sqrt{(R_i^*)^2 - \left(\frac{\lambda_i^*}{2} - d_{ij}\right)^2} - \sqrt{(R_i^*)^2 - \left(\frac{\lambda_i^*}{2}\right)^2} \quad (4.27)$$

Finally, the replacement $\mathbf{x}_j' \rightarrow \mathbf{x}_j' + \varepsilon_{ij}\hat{e}_i^*$ is carried out. Observe that, after replacing, the modulus of the vector $\boldsymbol{\lambda}'_j = \mathbf{x}_j' - \mathbf{x}'_{j-1}$ becomes slightly different from λ . Therefore, it is necessary to move the point \mathbf{x}_j' to fix the length of $\boldsymbol{\lambda}'_j$.

The second order correction is in practice very small. But it is important for points close to the surface, because it avoids abrupt changes of the interaction force in the PR.

4.2.2.4 Cubic Spline

To select the interval to apply the GR, it is desirable to have an approximate analytical solution $\mathbf{x}(\tau)$ with boundary conditions \mathbf{x}_μ , $\dot{\mathbf{x}}_\mu$, \mathbf{x}_ν , and $\dot{\mathbf{x}}_\nu$. The 2D static

Euler-Bernoulli equation describing a beam having a small deflection v is [169]

$$\frac{d^4 v}{d\tau^4} = \frac{Q}{EI}$$

For zero transverse load ($Q = 0$) the solution is a cubic spline [170]. The four integration constants are determined using the boundary conditions $v(\tau_\mu)$, $\dot{v}(\tau_\mu)$, $v(\tau_\nu)$, and $\dot{v}(\tau_\nu)$.

In 3D the cubic spline becomes

$$\mathbf{x}_{\text{cub}} = (1 - \tau)\mathbf{x}_\mu + \tau\mathbf{x}_\nu + \tau(1 - \tau)\left[(1 - \tau)\mathbf{s}_\mu - \tau\mathbf{s}_\nu\right] \quad (4.28)$$

where $\tau \in [0, 1]$. Let $\mathbf{X}_{\mu\nu} = \mathbf{x}_\nu - \mathbf{x}_\mu$ and $\hat{\mathbf{U}}_\mu$, $\hat{\mathbf{U}}_\nu$ be two unit vectors parallel to $\dot{\mathbf{x}}_\mu$, $\dot{\mathbf{x}}_\nu$ respectively. If the vectors \mathbf{s}_μ and \mathbf{s}_ν (associated with the cubic dependencies on τ) are perpendicular to the line $(1 - \tau)\mathbf{x}_\mu + \tau\mathbf{x}_\nu$ connecting the points \mathbf{x}_μ and \mathbf{x}_ν , then

$$\begin{aligned} \mathbf{s}_\mu &= \frac{|\mathbf{X}_{\mu\nu}|^2}{\mathbf{X}_{\mu\nu} \cdot \hat{\mathbf{U}}_\mu} \hat{\mathbf{U}}_\mu - \mathbf{X}_{\mu\nu} \\ \mathbf{s}_\nu &= \frac{|\mathbf{X}_{\mu\nu}|^2}{\mathbf{X}_{\mu\nu} \cdot \hat{\mathbf{U}}_\nu} \hat{\mathbf{U}}_\nu - \mathbf{X}_{\mu\nu} \end{aligned} \quad (4.29)$$

A small deflection occurs when $\hat{\mathbf{U}}_\mu$ and $\hat{\mathbf{U}}_\nu$ are nearly parallel to $\hat{\mathbf{X}}_{\mu\nu} = \mathbf{X}_{\mu\nu}/|\mathbf{X}_{\mu\nu}|$.

4.2.2.5 Interval Selection

To find a suitable interval to apply the GR, the first step is to search for intervals whose end points \mathbf{x}_μ , \mathbf{x}_ν are *close* to the surface, and whose inner points $\mathbf{x}_{\mu+1}, \dots, \mathbf{x}_{\nu-1}$ are *far* from the surface. Specifically, we considered a point is close (far) when the distance to the surface is smaller (larger) than 5% of the average artery diameter. It will be seen that in the PR cycle a point near to the surface can be bouncing (Section 4.3.4).

Next, discard intervals having few segments, say less than 5. Also exclude the tip of the wire, which is curved, and any other interval having a non-constant flexural rigidity.

For each of the remaining intervals execute the following operations. Given \mathbf{x}_μ and \mathbf{x}_ν with tangent vectors $\dot{\mathbf{x}}_\mu = \hat{\mathbf{u}}_\mu + \hat{\mathbf{u}}_{\mu+1}$ and $\dot{\mathbf{x}}_\nu = \hat{\mathbf{u}}_\nu + \hat{\mathbf{u}}_{\nu+1}$, determine the cubic spline $\mathbf{x}_{\text{cub},i}$. Then calculate the mean square deviation [171]

$$\sigma_{\mu\nu}^2 = \frac{1}{\nu - \mu} \sum_{i=\mu}^{\nu} \sigma_i^2 \quad (4.30)$$

where $\sigma_i^2 = |\mathbf{x}_i - \mathbf{x}_{\text{cub},i}|^2$. The cases of interest occur when the deviation $\sigma_{\mu\nu}$ is large. Moreover, the cubic spline is not a good approximation unless $\hat{\mathbf{U}}_\mu$ and $\hat{\mathbf{U}}_\nu$ are nearly parallel to $\hat{\mathbf{X}}_{\mu\nu}$, i.e. a bad approximation results if $1 + \hat{\mathbf{U}}_\mu \cdot \hat{\mathbf{X}}_{\mu\nu}$ or $1 + \hat{\mathbf{U}}_\nu \cdot \hat{\mathbf{X}}_{\mu\nu}$ are

small. Hence, calculate the following figure of merit

$$\chi_{\mu\nu} = (1 + \hat{\mathbf{U}}_{\mu} \cdot \hat{\mathbf{X}}_{\mu\nu})^2 (1 + \hat{\mathbf{U}}_{\nu} \cdot \hat{\mathbf{X}}_{\mu\nu})^2 \sigma_{\mu\nu} \quad (4.31)$$

and select the interval with the largest $\chi_{\mu\nu}$.

It is not mandatory to move the points when the distance between \mathbf{x}_i and $\mathbf{x}_{\text{cub},i}$ is small, so that a reduced interval can be chosen. If $\sigma_i < 0.10 \sigma_{\mu\nu}$ for $i = \mu + 1, \mu + 2, \dots, \mu_+$, then replace $\mu \rightarrow \mu_+$. Likewise, if $\sigma_i < 0.10 \sigma_{\mu\nu}$ for $i = \nu - 1, \nu - 2, \dots, \nu_-$, then replace $\nu \rightarrow \nu_-$. Note that a shorter interval decreases the PT to calculate the improved curve, which is proportional to $(\nu - \mu)^2$. Moreover, the angles $\angle(\hat{\mathbf{N}}_{\mu}, \hat{\mathbf{U}}_{\mu})$, $\angle(\hat{\mathbf{N}}_{\nu}, \hat{\mathbf{U}}_{\nu})$ are likely bigger than the angles $\angle(\hat{\mathbf{N}}_{\mu_+}, \hat{\mathbf{U}}_{\mu_+})$, $\angle(\hat{\mathbf{N}}_{\nu_-}, \hat{\mathbf{U}}_{\nu_-})$, where $\hat{\mathbf{N}}_i$ stands for a vector normal to the artery's surface. Hence, there is a smaller probability that the improved curve intercepts the surface when the interval is reduced.

If an interception occurs, then do not update $\mathbf{x}_i \rightarrow \mathbf{x}_i^*$ but use a linear interpolation $\mathbf{x}_i \rightarrow \zeta \mathbf{x}_i^* + (1 - \zeta) \mathbf{x}_i$ with $\zeta \in (0, 1)$. In practice, ζ should be large but it must avoid the intersection. Further, to ensure numerical stability it is convenient to limit ζ such that the tip of the wire does not displace a distance greater than λ . Thus, after executing the GR check if $|\mathbf{x}_n - \mathbf{x}_n'| < \lambda$, otherwise decrease ζ and repeat the interpolation.

4.2.2.6 Pseudocode

Algorithm 4.2: Pseudocode of the GR method. The entrance parameter is the entire wire. The procedure chooses the best interval of the wire to apply the GR and updates the points \mathbf{x}_j from $j = \mu + 1$ up to the end $j = n$.

```

void GeometricalRelaxation(wire geometry) {
    6. select the interval  $\mu < i < \nu$  to apply the GR, see Section 4.2.2.5;
    7. execute  $\nu - \mu$  iterations (with a total of  $(\nu - \mu)^2$  energy minimization
       updates), see Section 4.2.2.2;
    8. shift the points  $\mathbf{x}_{\mu+1}, \mathbf{x}_{\mu+2}, \dots, \mathbf{x}_n$  to restore the length  $|\boldsymbol{\lambda}_j| = \lambda$ , see
       Section 4.2.2.3;
}

```

Now, the PT of the GR will be analyzed using the Algorithm 4.2. The number of operations necessary to determine the interval in line **6** is proportional to n . Let us change the resolution of the wire in such a way that $\lambda \propto 1/n$. If the shape of the wire does not vary appreciably, then the position of the points $\mathbf{x}_{\mu 1}, \mathbf{x}_{\nu 1}$ before and $\mathbf{x}_{\mu 2}, \mathbf{x}_{\nu 2}$ after changing the resolution will be nearly the same. Thus, it is concluded that μ, ν are proportional to n and the PT in line **7** scales with n^2 (Section 4.2.2.5). Similarly, the PT in line **8** (proportional to $n - \mu$) scales with n . In summary, the average PT of the GR cycle is

$$t_{\text{geo}} = t_{\text{g1}}n + t_{\text{g2}}n^2 \quad (4.32)$$

4.2.3 Combination of Physical and Geometrical Relaxation

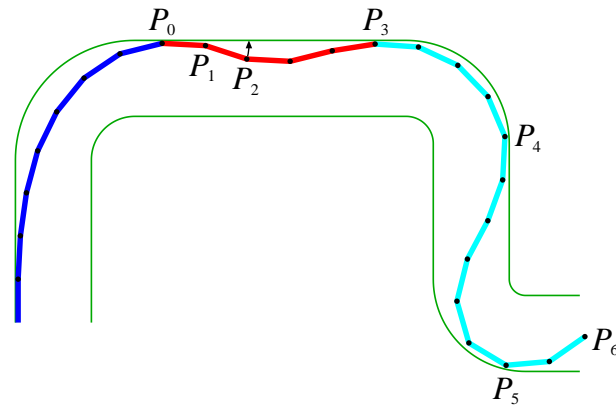


Figure 4.9: Wire segments inside an artery. In order to relax, the segment $\overline{P_1P_2}$ should rotate upwards about point P_1 as indicated by the arrow. Note that from P_2 to P_6 the wire is rigid, so that the resulting translation is hindered by the contact points P_3 and P_4 . Nor can it move downwards because of P_5 . The GR is not subjected to this restriction, since from P_3 up to P_6 the wire can slide. It is especially designed to relax intervals like from P_0 to P_3 (red).

A major drawback of the PR is that the wire moves as rigid structure about a fixed point. Depending on the boundary conditions this can be very hard to achieve. For example, the segment $\overline{P_1P_2}$ in Fig. 4.9 needs to turn up but it is hindered by contact points.

One possible solution is the GR developed in Section 4.2.2, which allows the wire to slide. The GR is executed after a PR cycle (Fig. 4.10) and does not interfere with it, because the GR is much faster than the PR (Section 4.3.3). In particular, if a user action takes place during a PR or a GR cycle, then it is interrupted and a Tip Relaxation is executed (this ensures stability). Moreover, the shape of the tip (where the actions take place) looks more natural. The combination of both techniques results in a more realistic wire behavior than using only the relaxation proposed by Konings et al. [64].

4.2.4 Wire Device

Here, a simple device to capture the wire motion is described (Fig. 4.11). In cardiovascular procedures, the wire sweeps at most a length of 150 mm inside the coronary [172]. In view of this fact, the required materials are:

- Support box.
- Pipe tube of length 320 mm, with a small window in the middle.

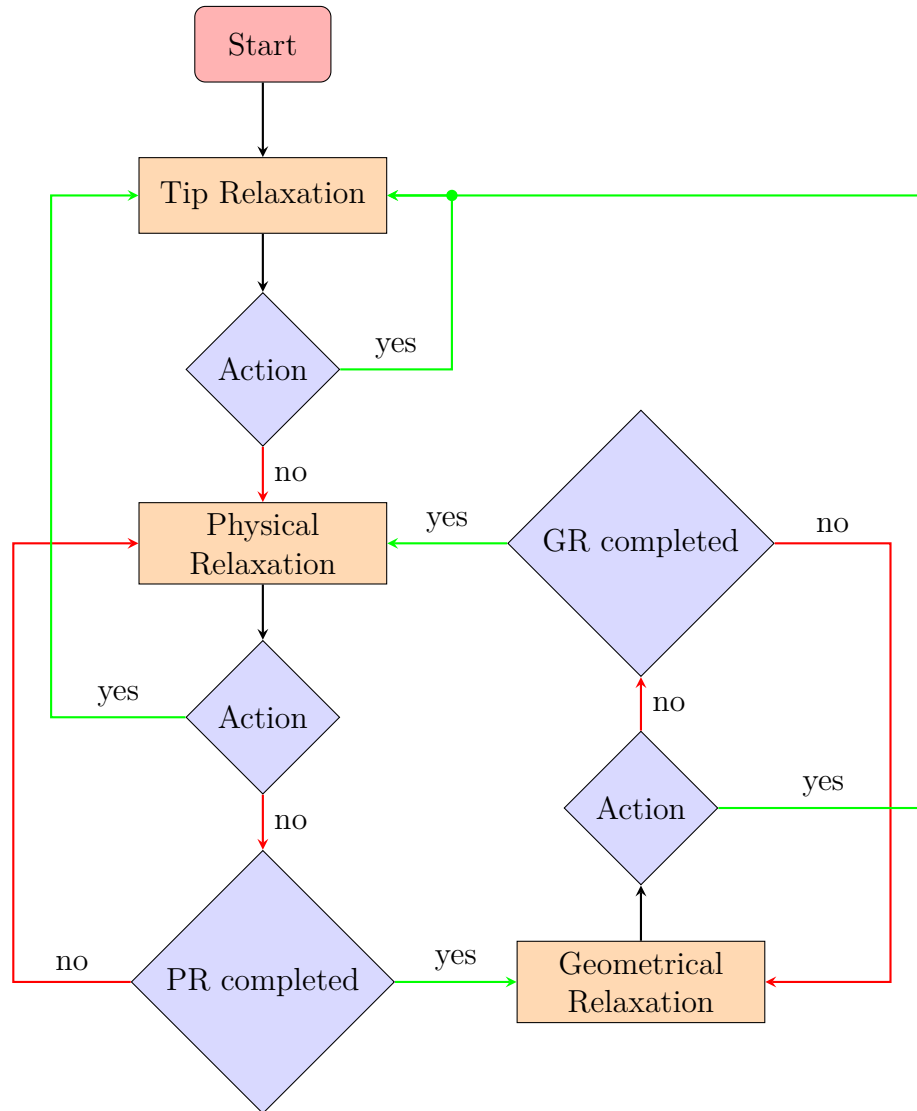


Figure 4.10: *Workflow.* In the “Tip Relaxation” (Section 4.2.1) the procedure *PhysicalUpdate* is applied to the tip of the wire and also to some selected segments. When the “Physical Relaxation” is called, $\frac{1}{2}m(m+1)$ updates are executed. The PR is completed if the cycle ends, i.e. after $\frac{1}{2}n(n+1)$ updates. In the same way, when the “Geometrical Relaxation” is called, $m(m+1)/(\nu-\mu)$ iterations are executed to improve the curve. The GR is completed after $\nu-\mu$ iterations.

- Light and opaque cylinder 170 mm long.
- Optical mouse with a precision of 1200 dpi or higher.
- Set of catheter and steerable wire with 150 mm free length.

The wire is attached to the cylinder, which is put inside the pipe. In particular,

the material of the pipe and the cylinder should be chosen in such a way that the friction between them must be small as possible [173]. The mouse is fixed over the pipe so that the light-emitting diode stays on the window. Moreover, it is possible to add extra commands to improve the simulator. For instance, the mouse buttons can simulate the contrast injection or the activation of the X-ray employed in video generation. Also, a USB-joystick with two axis can be used to change the C-arm [16] perspective.

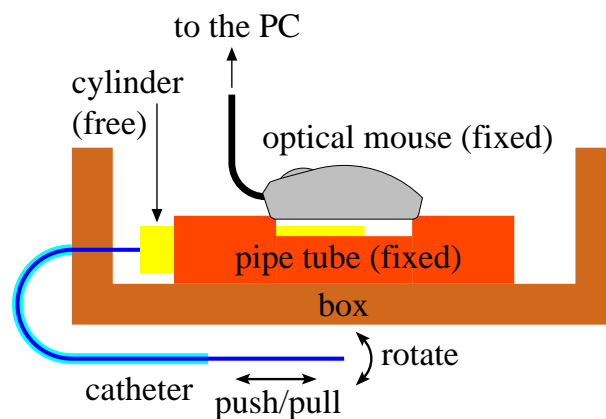
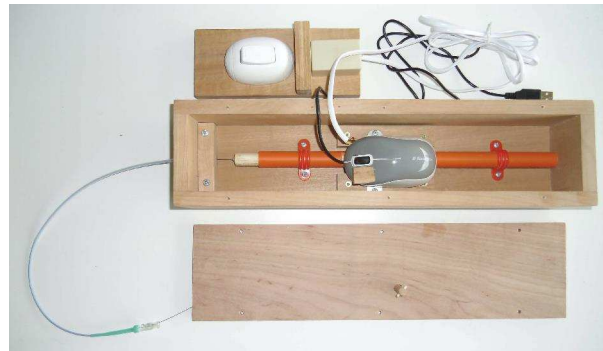


Figure 4.11: *Photography (top-view) and sketch (cross-view) of the wire device. The pipe has a small window and the mouse is over the window. Translating and rotating the wire also translates and rotates the cylinder, which is captured by the mouse.*

The wire movement is transferred to the cylinder and captured by the mouse according to:

- Pushing and pulling the wire = cursor up and down.
- Rotating the wire = cursor left and right.

The mouse must be aligned with the axis of the cylinder, otherwise translations and rotations will appear mixed. Depending on the mouse resolution, pointer speed, and

cylinder diameter, different cursor movements are obtained. Hence, a calibration is required to provide a correct feedback to the user. As an alternative to the optical mouse, a piezoelectric captor [174] can be connected to detect the cylinder motion.

The device has the technology of an optical mouse, whose movements can be read with basic functions in any programming language. The manufacturing cost is low and the portability allows the device to be used without platform restrictions.

Since the tip of the wire is soft [175], the contribution to the sense of touch is not significant. The force feedback is due mainly to the friction between the wire and the catheter [165]. In our device this force is already embodied, because the wire slides inside the catheter. This removes the complex problem of coupling haptics [176] and graphic simulation, especially because they proceed at different frequencies (of the order of 1000 Hz and 30 Hz respectively [177, 178]).

4.3 Technical Evaluation

In order to validate the usefulness and to examine the limitations of the methods developed in this work, several analysis were performed including the stability, wire resolution, and PT of the PR and GR. Moreover, the interaction between the wire and the artery was inspected. Finally, the present model was compared with the model of Alderliesten et al. [12].

In the simulations, a flexural rigidity EI equal to $6.35 \times 10^{-9} \text{ Nm}^2$ is assumed, experimentally obtained from a trial wire [179]. The algorithm was implemented in C++, and the tests were performed in a computer having a Intel Core i7-4500U (2.40 GHz) and 16 GB of RAM.

4.3.1 Stability Analysis

The total PT was tested for the artery shown in Fig. 4.12, which includes a T-like and a Y-like bifurcation (Section 2.2.1). In the first part of the simulation, the wire is outside the artery and it is quickly pushed inside (only the Tip Relaxation is applied). The result (green curve) looks unphysical, but the algorithm does not crash during a fast insertion of the wire. The stability is also verified if λ increases to 2.5 mm, so that a deeper frontal collision occurs at the T-like bifurcation. However, if the wire becomes very stiff (a huge flexural rigidity), then it will “perforate” the artery (like a needle) and the behavior becomes unstable.

In contrast, the algorithm of Alderliesten et al. [12] demands a slow insertion of the wire, otherwise it can crash. For example, in numerical tests Konings et al. [64] and Alderliesten et al. [49] used an internal stepsize smaller than $\lambda/10$. Since they insert the new segment in the proximal end of the wire, to guarantee stability they must execute at least ten times the complete relaxation cycle before a new action takes place. As in Eq. (4.20), their PT is proportional to n^3 for large n , but in our case it is proportional to a constant plus $n^{3/2}$ (see Eq. (4.21)). Hence, this method works much faster under stress conditions.

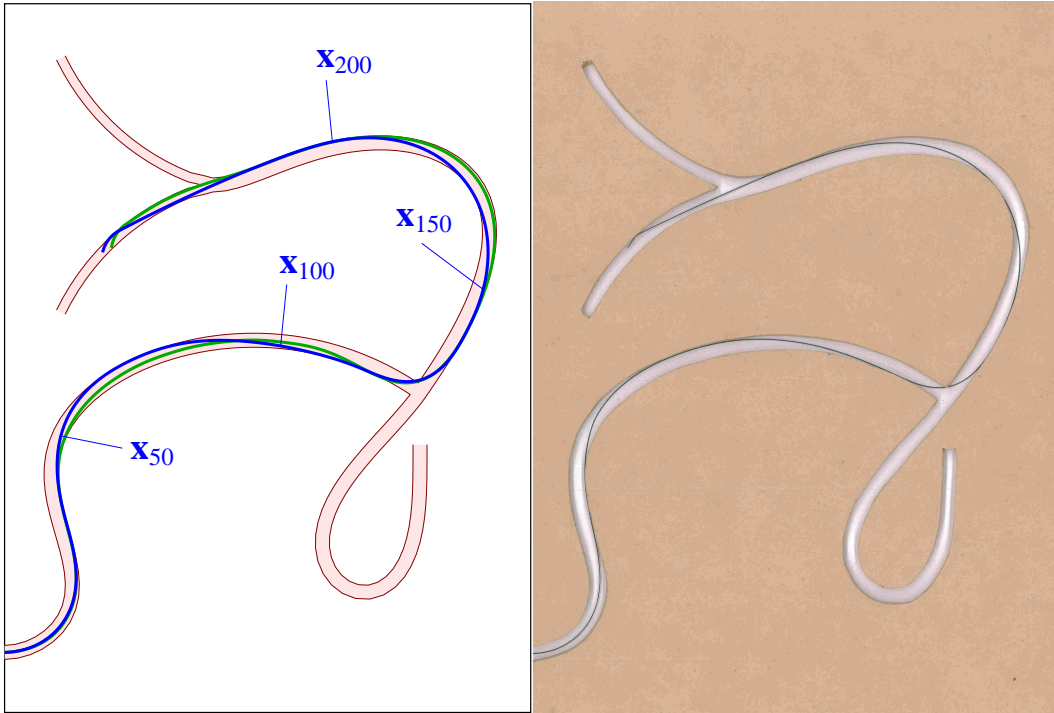


Figure 4.12: Artery with a *T*-like and a *Y*-like bifurcation. (Left) The wire has 250 segments, $\lambda = 1$ mm, and it has been quickly inserted into the artery (green curve). In this part, the program executed only Tip Relaxations and the time consumed was 0.24 seconds. In the second part, no action takes place and a combination of 100 relaxation cycles (Physical and Geometrical) is executed, so that equilibrium is attained (blue curve). The coordinates indicate the location of some wire joints. (Right) Mockup representing the stiff artery. The wire inserted in the artery has the same shape as the blue curve. The average separation between the physical wire (plot digitized with WebPlotDigitizer 3.8 <http://arohatgi.info/WebPlotDigitizer>) and the blue curve is 0.262 mm, with a standard deviation of 0.227 mm. Hence, the calculations with the model developed in this work give a realistic result.

In the second part of the simulation, a large number of cycles are executed. The result is the blue curve in Fig. 4.12 (left) and a numerical comparison with experiment (right) shows that the calculations are truthful. Besides the specific case in Fig. 4.12, several paths have been tested and the results were always good.

In real procedures, the physician should not insert the wire quickly to avoid vascular damage [180, 181]. For security reasons, in the specific case of Teleoperation the speed of the slide platform is less than 10 mm/s [162]. On the other hand, one of the most annoying situations encountered by users in simulators, is the time delay

between the action and the response [182]. In our simulator (green curve in Fig. 4.12) the average speed was $(250 \text{ mm})/(0.24 \text{ s}) \approx 1 \text{ m/s}$.

4.3.2 Segment Size

The PT will depend on the artery's resolution and on the size of the segment λ . The method of Chapter 2 to calculate \mathbf{G}_i is almost independent of the artery's resolution. This artery model refers to a geometry which does not depend on time. Otherwise the proposed method is not feasible, because changes of shape make it more difficult to use precomputed data structures for expediting collision tests during simulation [148]. On the other hand, some works try to enhance the surgeon's endoscopic vision with a time dependent 3D model of the coronary artery tree to be used in a per-operative augmented reality [183, 184], but the resulting images are not segmented.

If λ decreases but the wire length remains the same, the total number of segments n increases. Hence, with a higher wire resolution the PT becomes longer. To determine the optimal segment size, the influence of λ on the shape of the wire must be investigated [12]. Afterwards, set the size to the maximum value which gives a satisfactory visual effect.

In Fig. 4.13, the simulations for $\lambda_A = 2.5 \text{ mm}$ (wire *A*) and $\lambda_B = 1 \text{ mm}$ (wire *B*) are compared. The equilibrium looks similar, but the time t_A required for wire *A* is only 11% of the time t_B required for wire *B*. The shape difference is not due to the precision of the calculations with different values of λ , but to the contact points with the artery, which is not the same in the case of wire *A* and in the case of wire *B*. The wire *A* has less contact points and in the T-like bifurcation the wire *A* penetrates deeper inside the corner of the artery wall. The wire *B* has a bigger resolution and the result is closer to the real artery (Fig. 4.12).

4.3.3 Physical and Geometrical Processing Time

Table 4.1: *PT of the PR (t_{phy}) and of the GR (t_{geo}) for different resolutions: $\lambda_A = 2.5 \text{ mm}$, $\lambda_B = 1.0 \text{ mm}$, and $\lambda_C = 0.4 \text{ mm}$. The PT does not include the fast insertion of the wire, but only the relaxation between the green and the blue curves in Fig. 4.12. The approximated times $t_{\text{phy,fit}}$ and $t_{\text{geo,fit}}$ have been obtained with Eq. (4.33).*

λ_X	2.5	1.0	0.4
t_{phy}	0.9840	9.330	103.7
t_{geo}	0.0160	0.0704	0.2431
$t_{\text{phy,fit}}$	1.026	9.321	103.7
$t_{\text{geo,fit}}$	0.0220	0.0671	0.2435

A further comparison is made using $\lambda_C = 0.4 \text{ mm}$ (wire *C*), so that $\lambda_A/\lambda_B = \lambda_B/\lambda_C = 2.5$ or $n_B/n_A = n_C/n_B = 2.5$. The relative PT is in Table 4.1 and for

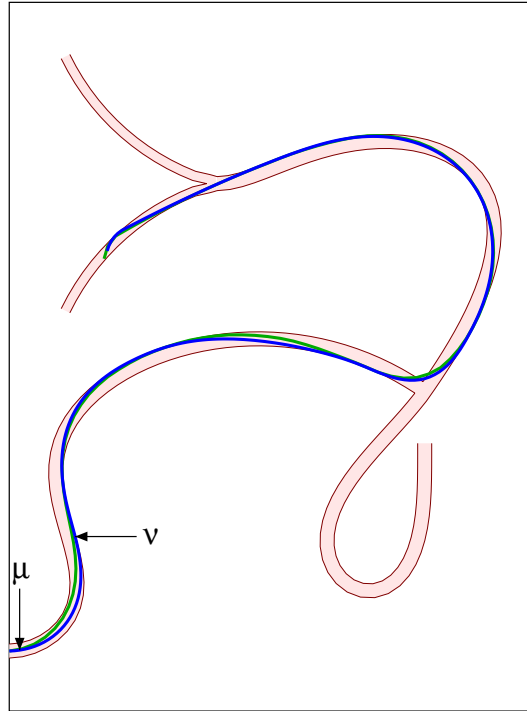


Figure 4.13: The green wire A has $n_A = 100$ segments, $\lambda_A = 2.5$ mm and the blue wire B has $n_B = 250$ segments, $\lambda_B = 1$ mm. Hence $n_A \lambda_A = n_B \lambda_B$. The arrows indicate one of the intervals $\mu < i < \nu$ where the GR is applied. In the case of wire A it was found that $\mu_A = 1$, $\nu_A = 13$ and in the case of wire B it was found that $\mu_B = 2$, $\nu_B = 30$. Thus, μ and ν are closely proportional to n .

increasing resolution the PT of the PR becomes much larger than the PT of the GR. The data can be approximated with Eqs. (4.20) and (4.32)

$$\begin{aligned}
 t_{\text{phy}} &= 0.716 \left(\frac{n}{100} \right)^2 + 0.310 \left(\frac{n}{100} \right)^3 \\
 t_{\text{geo}} &= 0.01875 \frac{n}{100} + 0.00323 \left(\frac{n}{100} \right)^2
 \end{aligned} \tag{4.33}$$

From Table 4.1 it can be read that

- For $\lambda_A = 2.5$ mm or $n_A = 100$: $t_{\text{phy}}/t_{\text{geo}} = 61.6$
- For $\lambda_B = 1.0$ mm or $n_B = 250$: $t_{\text{phy}}/t_{\text{geo}} = 132.5$
- For $\lambda_C = 0.4$ mm or $n_C = 625$: $t_{\text{phy}}/t_{\text{geo}} = 426.5$

Note that the ratio $t_{\text{phy}}/t_{\text{geo}}$ increases from n_A to n_B by a factor 2.15, and from n_B to n_C by a factor 3.22. These factors are close to $n_B/n_A = n_C/n_B = 2.5$ or nearly

proportional to n . Indeed, for $t_{p1} = t_{p2} = 0$ in Eq. (4.20) and $t_{g1} = 0$ in Eq. (4.32), it follows that $t_{\text{phy}}/t_{\text{geo}} \propto n$. In general, for large n the time t_{geo} is much smaller than t_{phy} .

The PT of the GR is discussed now in detail. For a fixed n and given μ, ν , the time in Eq. (4.32) can be put in the form

$$t_{\text{geo}} = t_{\mu\nu 0} + t_{\mu\nu 1}(\nu - \mu) + t_{\mu\nu 2}(\nu - \mu)^2 \quad (4.34)$$

The results for wire B and wire C are shown in Fig. 4.14. Note that there are points missing in the numerical experiments, because in the calculations not every interval size $\nu - \mu$ occurs. In particular, the blue points are not far from the red points for $\nu - \mu \approx 60$.

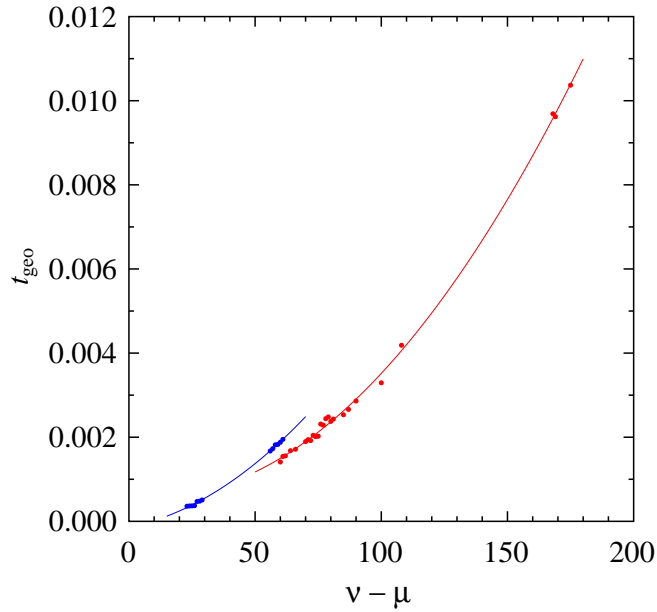


Figure 4.14: GR relaxation time t_{geo} as function of the interval length $\nu - \mu$. The blue color represents the wire B with $n_B = 250$ segments (blue curve in Fig. 4.13) and the red color represents the wire C with $n_C = 625$ segments (not shown in Fig. 4.13). The points are the PT measured in numerical simulations and the lines are the fits performed with Eq. (4.34).

The blue points in the interval $20 < \nu - \mu < 30$ correspond to the red points in the interval $60 < \nu - \mu < 90$, because μ and ν are nearly proportional to n (Section 4.2.2.6). Also, the blue points in $55 < \nu - \mu < 60$ correspond to the red points in $165 < \nu - \mu < 175$.

The PT for a single energy minimization does not depend on the total number of wire segments. Since $(\nu - \mu)^2$ minimization updates are executed in a GR cycle, the quadratic coefficient in Eq. (4.34) should always be the same. Indeed, this

coefficient is equal to $t_{g2} = 0.003663, 0.003586$ for wire B , wire C respectively, and the difference is 2%.

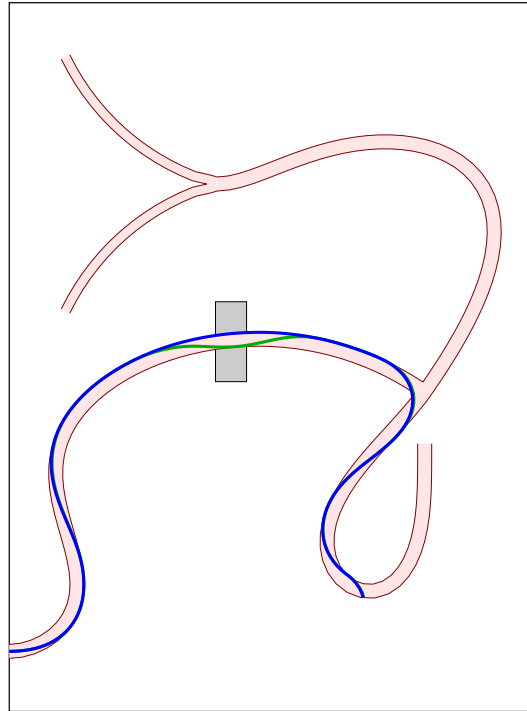


Figure 4.15: *Initial curve (green) and the final equilibrium curve (blue) obtained after a very long relaxation time. The final result is the same with or without the GR. The analysis is focussed in the wire portion located inside the gray box, which goes from wire segment number 90 to 95. In this interval are seen the most relevant changes during relaxation.*

It is also interesting to compare the PT using the PR (case P) and using both the PR and the GR (case G). The outcomes are highly dependent on the initial wire shape and on the boundary conditions (artery geometry). For instance, Fig. 4.15 shows an initial curve (green) and the situation is similar to that depicted in Fig. 4.9. Although the final result is the same in cases P and G (blue curve in Fig. 4.15), the relaxation times are very different. Specifically, the time is computed so that the difference, between the blue and green curve for the segments inside the gray box, is reduced to 10%. The result is $t_P/t_G = 3.73$, which means that the PT with GR is only 27% of the PT without GR.

As pointed out previously, the ratio t_P/t_G depends on the specific boundary conditions and on the initial wire shape. In all cases $t_G < t_P$ is obtained, but the reduction is not always noticeably. In summary, using both the PR and GR a shorter PT is achieved, although the pertinent improvement of the method is found when the wire is hindered.

4.3.4 Wire-Artery Contact

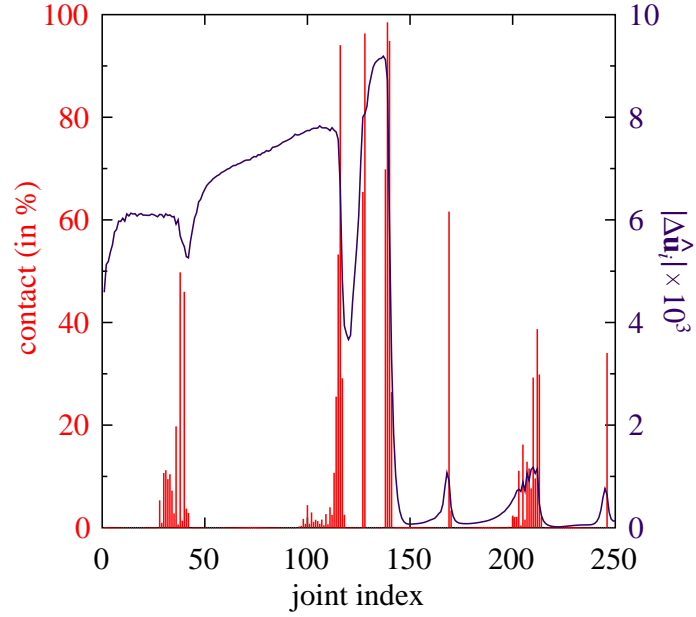


Figure 4.16: The red bars represent the percentage of the time in which each joint (blue curve in Fig. 4.12) is in contact with the artery’s surface. The magenta curve represents the average modulus of the unit vector update $\Delta \hat{\mathbf{u}}_i$ during a PR cycle.

It will now be analyzed how much time each point is in contact with the artery in a *static solution* (Fig. 4.16). In general, a softer wire (small flexural rigidity EI) will have more points (a longer interval) in contact with the artery than a stiffer one [49, 185]. Also, the shape of the artery will influence the number of collisions. Hence, the flexural rigidity and the shape affect the PT to compute the surface energy gradient in Eq. (4.9).

Only few points are effectively touching the surface, holding the wire to the equilibrium position. The points bounce in the artery and the total number of contacts vary from one step to the next. For instance, the surface force can eject the point and then it becomes zero. In the next steps, due to the elastic restoring force of the wire, the same point can move back.

The magenta curve in Fig. 4.16 shows the modulus of the update $\Delta \hat{\mathbf{u}}_i$. In particular, the maximum $|\Delta \hat{\mathbf{u}}_{137}| = 9.2 \times 10^{-3}$ corresponds to an amplitude variation of $4.6 \mu\text{m}$ around the average position of \mathbf{x}_i for $137 \leq i \leq 250$. Note that in one complete PR cycle, the unit vector $\hat{\mathbf{u}}_i$ will be updated i times. Furthermore, after a joint collision has been surpassed, the modulus drops because the contribution of the surface gradient is suppressed from the sum in Eq. (4.9).

Although the numerical solution looks unstable, the oscillations are tiny and they are not perceptible. Moreover, the algorithm is usually applied in dynamic simulations where the wire is moving, and a final equilibrium configuration is not required.

4.3.5 Comparison of Physical Models

The PR is essentially the same relaxation introduced by Alderliesten et al. [12]. The difference is that in the energy of the i -th joint $U_i = C_i g(\theta_i)$ we use the approximation $g_1(\theta_i) = (13 - 14 \cos \theta_i + \cos^2 \theta_i)/12$, while they use $g_2(\theta_i) = (1 - \cos^2 \theta_i)/2$. Thus, in the calculations

$$\frac{k_i}{\lambda^2} = \kappa_{i-1} \lesssim 1$$

$$\frac{k'_i}{\lambda^2} = \kappa_i \lesssim 1$$

are replaced by

$$p_i \gtrsim 1$$

$$q_i \gtrsim 1$$

respectively (see Eq. (4.8)).

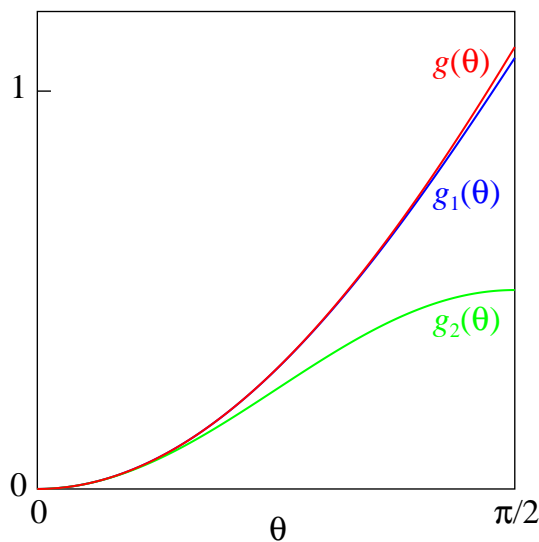


Figure 4.17: Comparison of the functions $g(\theta)$ (red; exact), $g_1(\theta)$ (blue; this work), and $g_2(\theta)$ (green; Alderliesten et al. [12]) in the interval $0 < \theta < \pi/2$.

The functions $g_1(\theta)$ and $g_2(\theta)$ are compared with the exact $g(\theta) = \theta \sin(\theta/2)$ in Fig. 4.17. All functions have a minimum at $\theta = 0$ and, in the absence of external forces, equilibrium is achieved when there is no bending. For $\theta < 0.1$ rad = 5.7° they are almost identical: the errors of $g_1(\theta)$ and $g_2(\theta)$ are less than $4.7 \times 10^{-5}\%$ and 0.29% respectively. But for $\theta \sim 1$ rad = 57° the function $g_1(\theta)$ is clearly superior.

Numerical simulations performed with g_1 and with g_2 have been compared. Specifically, the blue curve in Fig. 4.13 ($\lambda_B = 1$ mm) is relaxed over a long period of time using our model (without including the GR) and using the model of Alderliesten et al. [12]. The average difference between both calculations is 0.052 mm, which

is nearly the same precision of the calculations due to tiny oscillations around the equilibrium position (Section 4.3.4). Moreover, for $\lambda_A = 2.5$ mm and for $\lambda_C = 0.4$ mm the average differences are 0.121 mm and 0.010 mm respectively. Note that for small λ (higher resolution) the calculations are more precise.

Further, the following average and maximum values of the angle θ_i between $\hat{\mathbf{u}}_{i-1}$ and $\hat{\mathbf{u}}_i$ were obtained

- For λ_A : $\bar{\theta} = 4.7^\circ$ and $\theta_{\max} = 13.6^\circ$
- For λ_B : $\bar{\theta} = 1.9^\circ$ and $\theta_{\max} = 6.7^\circ$
- For λ_C : $\bar{\theta} = 0.75^\circ$ and $\theta_{\max} = 2.9^\circ$

Hence, the results with g_1 and with g_2 are practically the same, because the angles θ_i are small. However, in a deep frontal collision of the wire with the artery, the angle is very large. In such situations, it is advantageous to use g_1 which gives a better approximation.

4.3.6 Validation Tests

A dozen specialized participants of a conference in 2011 at INTUS (Interdisziplinäres Trainings- und Simulationszentrum, <http://intus-wuerzburg.de>) performed an informal comparison between our initial setup and three commercial vascular simulators (see Fig. 1.2). The majority of the specialists gave the best approval ratings to our setup. We also requested the participants to fill out a formulary (Appendix A) and the results are summarized in Table 4.2. The worst grade was to the wire realism, which motivated us to work and to improve the method. On the other hand, the best grade was to the easiness of use due to the simplicity and portability of the device.

Table 4.2: *Survey of the initial simulator applied in a conference in 2011 with a dozen specialized participants. The grade scale goes from 1 (poor) to 5 (optimal).*

	Average grade
Easy to use	4.3
Robustness, stability	4.1
Realism of the wire	3.4
Learning effect	4.1
Overall judgment	4.1

Actually, one of the current challenges is to evaluate the propensity of a simulator to help the user gain skills within its professional environment, not only increase its ability in using the simulator [186].

We also ask to the participants to feel free to write any comment, suggestion or compliment. The answers can be summarized as follows:

- Simulate the exchange of the wire.
- Possibility for two angulations.

The commentaries refers basically to the possibility to fold the wire besides the tip and change the type of the wire. These techniques help the navigation of the wire inside the coronaries [187] and have already been incorporated to the simulator. To add a new angulation in a specific point of the wire, it is necessary to redefine the ω_i (Fig. 4.4). To change the type of the wire, it is necessary to modify his flexural moment EI .

4.4 Software

The simulator was developed in C++. It uses the OpenGL² graphic library and can be compiled in any platform. The software has many functionalities shown in the normal perspective (Fig. 4.18):

Curvature, Angle, Tip - Controls the deformation of the wire tip used in the simulation.

Speed - Scales the real wire displacement to the virtual wire displacement.

Beat - Set the beat of the heart.

Time - Reset the time counter.

Keyboard arrows or joystick - Change the position of the C-arm, modifying the view angle.

Contrast - Inject the dye.

X-Ray - Activate the X-Ray.

The last two elements (Contrast and X-Ray) must be used at minimum level by the physician, in order to preserve the health of the patient [190].

One of the most difficult skill the physician must achieve, is the 3D perception of the angioplasty using only the 2D view of the monitor, especially when the arteries overlap [183, 191]. To help this visualization, it is possible to change the perspective in order to view inside the artery. Although this is still not possible in real interventions, it helps the physicians to figure out the problem during learning (Fig. 4.19).

Once the physicians understands the 3D difficulty, he/she can use a joystick to change the left and right anterior oblique views (LAO and RAO) or cranial and caudal angulation of the C-arm,³ obtaining better projections. The position of the C-Arm relative to the patient can be seen in the right bottom screen of the simulator (Fig. 4.18).

²Open Graphics Library www.opengl.org

³The most common values used for these angulations can be found in the Table [5] from Chapter 41 of Lanzer & Topol [192].



Figure 4.18: View of the normal perspective frame from the simulator, showing a fictive left coronary. The user goal is to reach the green ball at the end of the artery. In this case, the implementation follows the idea of “serious games” [188, 189], where there is a primary purpose (increase the ability using the wire) other than pure entertainment.

4.5 Conclusions

Using a hardware in combination with an algorithm that responds in real time is helpful for training MIS. More physicians can be trained over longer periods of time (increasing skills) and no disposable instruments are needed (decreasing costs).

In this chapter a simulation system for MIVS was presented. It consists of a simple device to capture the wire motion and two complementary methods to relax the wire. The physical model introduced by Konings et al. [64] was improved. Although the results are nearly the same for small beam deflections, our approximation $g_1(\theta)$ is superior for larger deflections.

The divergence problem, when the denominator in Eq. (4.16) becomes small or negative, was detected and solved. The update formula in Eq. (4.19) is simpler than

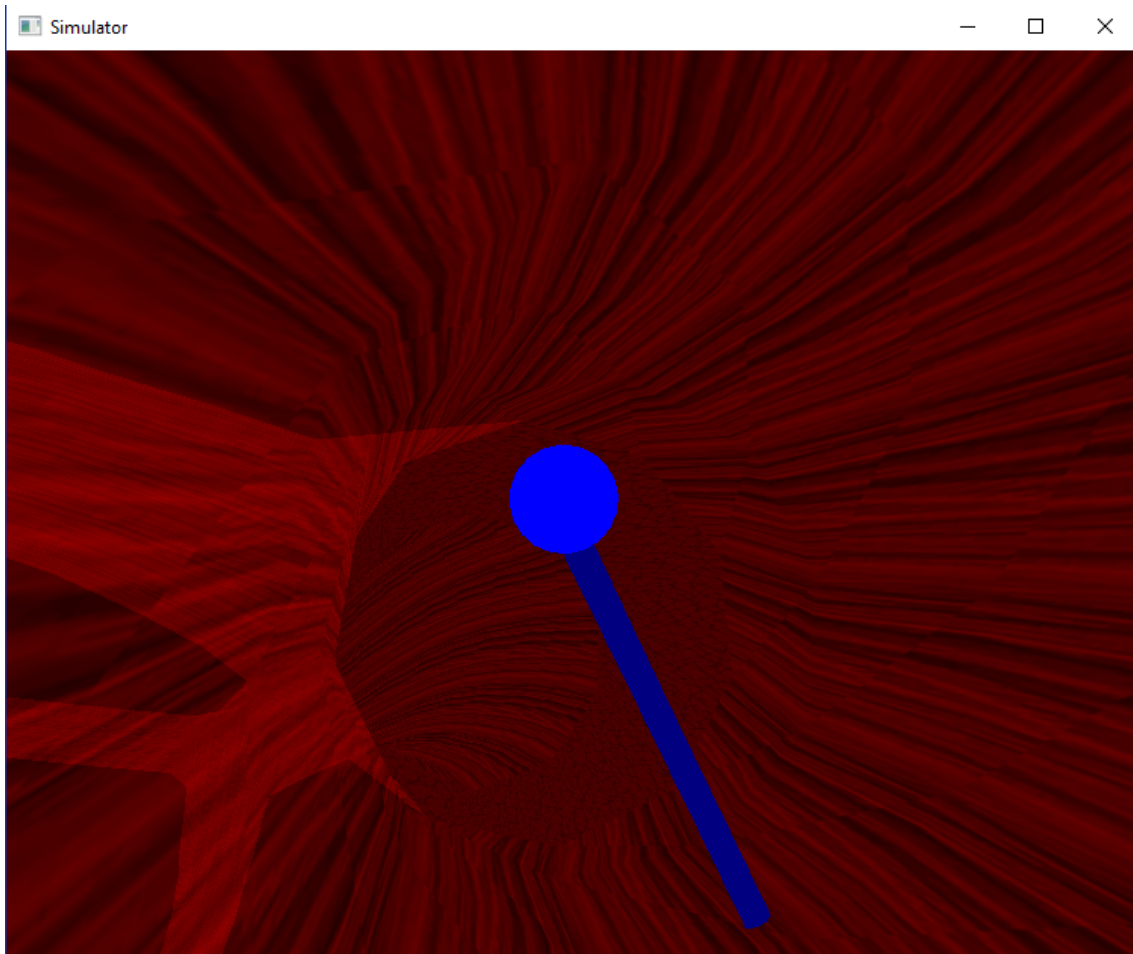


Figure 4.19: *View of the wire perspective. This is useful to elucidate the overlap situations of two or more arteries, helping the physician to understand the bifurcation.*

Eq. (11) of Alderliesten et al. [12]. Also, the algorithm does not crash when the surface gradient becomes large. Hence, the wire can be moved quickly in the artery.

The PR has some drawbacks which have been amended with the GR. The PT of the GR is proportional to n^2 and the PT of the PR is proportional to n^3 . Therefore, the GR is faster, does not interfere with the PR, and helps to correct some wire distortions. Using both methods gives stable and realistic results, as seen in comparisons of experiments with numerical calculations.

In a stiff artery only few points of the wire are in contact with the surface. Although these points are bouncing, the numerical instability is not perceptible. Moreover, several other cases besides the ones shown in Section 4.3 (e.g. different artery shapes, rigidity levels, wire paths in the mockup) have been tested and the outcomes have been similar.

Chapter 5

Conclusions and Future Works

A simulator of MIVS is composed of several parts. First, the surface geometry must be defined; second, the interaction between the surface and the wire must be calculated; third, the shape of the wire must be determined. The performance of the simulator depends on the hardware (CPU and GPU), the resolution of the artery and of the wire, the force field to model the collision, and the wire relaxation.

An intuitive way to create the geometry of an artery using the sweep technique was proposed in Chapter 2, which can be extended to bifurcations. The procedure can also be applied to model arteries with real data. The most time-consuming task in catheter simulations is the calculation of interactions between the wire and the surface. The use of planar surfaces in the segmentation simplifies the collision-detection algorithm and it becomes faster. The artery can have an arbitrary resolution and it does not affect the PT significantly. The proposed force field is a continuous function of position, except under special circumstances at bifurcations.

The artery model developed in Chapter 3 is linear and two dimensional, which results in shorter PT. It is suitable for computing small and noninvasive artery deformations as required, for example, in the calculation of equivalent spring constants for the catheter simulator. Furthermore, our model implicitly includes the individual characteristics and inhomogeneous properties of the artery layers.

Some of the elasticity tensor components were obtained and a method to calculate the spring stiffnesses connecting the mesh nodes was described. Three kinds of springs were introduced: one linear and two angular. The stiffness of the springs was analyzed for different mesh resolutions, artery sizes, and the method was validated by different loads. Finally, the elasticity tensor strongly depends on the stretch, especially if the Intima layer is axially deformed. However, assuming a stretch variation smaller than 1%, the linear approximation is accurate.

In Chapter 4, a simulation system for MIVS was presented. It consists of a simple device to capture the motion and two complementary methods to relax the wire. The physical model introduced by Konings et al. [64] was improved and a divergence problem was detected and solved. The proposed update formula is simpler than Eq. (11) of Alderliesten et al. [12] and the algorithm does not crash during a fast wire movement.

The PR has some drawbacks which have been amended with the GR. The PT of the GR is proportional to n^2 and the PT of the PR is proportional to n^3 , where n represents the number of wire segments. Therefore, the GR is faster, does not interfere with the PR, and helps to correct some wire distortions. Using both methods gives stable and realistic results, as seen in comparisons of experiments with numerical calculations.

The work in this thesis can be extended in several aspects. The sweep surfaces can be made less restrictive with similar results, provided that the boundary between artery segments is planar. Working with a database representing a sequence of surfaces, can simulate the heart beat or any other periodic movements of the arteries. However, in order to apply this idea it is necessary to have an algorithm which performs very fast wire relaxation. If the sweep surfaces are generated in real time using MR Images, they can be used to implement augmented reality, so that the

physicians obtain a better perception during the procedure.

A systematic study of the equivalent spring constants in different artery geometries has not been done. This information can be especially useful to analyze the elastic behaviour close to the bifurcations, because the critical part of catheterism is to guide the wire through the bifurcation. Moreover, the artery deformation plays a central role in balloon angioplasty and stenting. Chapter 3 contains the basic elements and the methodology to perform this study. In particular, a theory using triangular SE would be more useful because they are commonly used in surface meshing. The results in 3D can be compared to numerical calculations performed with FEM.

As remarked previously, even faster relaxation algorithms are necessary to have real time simulations, especially if the artery geometry becomes time dependent. One way to approach this problem can be to consider higher order wire approximation and to analyze how it affects the precision and the PT. Furthermore, a faster energy minimization algorithm (Section 4.2.2.2) can improve the GR substantially.

As the wire is continuously deformed, there are several energy minima. The problem is then equivalent to search the minimum of a function in a very larger dimensional space. Using a more complex numerical procedure would help to skip these minima, so that the absolute (true) minimum is found. Specifically, a multiple joint relaxation procedure can be implemented, where the joints are strategically chosen. The relaxations would be faster but the procedure may become unstable, so that the trade off between the PT and the stability needs to be analyzed.

Finally, a more detailed and extensive evaluation of the simulator must be carried out. Some important questions to be addressed are:

- What are the experience and/or expertise level of the evaluators?
- How does our setup compare to other simulators? On what basis?
- The simulator helps the user to gain skills within its professional environment?

This evaluation will be realized after the software has been improved.

Appendix A

Formulary

Formulary regarding to the wire simulator.

The wire simulator you just tested is been developed to be an auxiliary teaching tool to the physicians with the manipulation of the wire in vascular procedures.

Please help us to improve his development filling out the following formulary.

	Optimal		\leftrightarrow	Poorly	
	5	4	3	2	1
Easy to use	<input type="radio"/>	<input type="radio"/>	<input type="radio"/>	<input type="radio"/>	<input type="radio"/>
Robustness, stability	<input type="radio"/>	<input type="radio"/>	<input type="radio"/>	<input type="radio"/>	<input type="radio"/>
Realism of the wire	<input type="radio"/>	<input type="radio"/>	<input type="radio"/>	<input type="radio"/>	<input type="radio"/>
Learning effect	<input type="radio"/>	<input type="radio"/>	<input type="radio"/>	<input type="radio"/>	<input type="radio"/>
Overall judgment	<input type="radio"/>	<input type="radio"/>	<input type="radio"/>	<input type="radio"/>	<input type="radio"/>

Please feel free to write any comment, suggestion or compliment:

List of Abbreviations

2D	Two-Dimensional	7
3D	Three-Dimensional	10
ET	Elasticity Tensor	7
FEM	Finite Element Method	7
GR	Geometrical Relaxation	7
IVUS	Intravascular Ultrasound	4
MIS	Minimally Invasive Surgery	2
MIVS	Minimally Invasive Vascular Surgery	2
MR	Magnetic Resonance	2
PR	Physical Relaxation	8
PT	Processing Time	5
SE	Surface Elements	12
VRS	Virtual Reality Simulators	2

List of Figures

1.1	Interventional cardiologists from New York-Presbyterian Hospital and Columbia University Medical, performing a coronary angiogram in a cardiac catheterization laboratory. The C-Arm [16] generates/detects the X-Rays and the images are displayed on the screen.	3
1.2	Commercial VRS for endovascular procedures: (a) Mentice VIST-C (www.mentice.com), (b) CAE Cath VR (www.caehealthcare.com), and (c) Symbionix ANGIO Mentor (http://symbionix.com).	4
1.3	Components of a real-time simulator proposed by Dawson et al. [35]. The user interacts with the haptics interface device containing catheters and guidewires linked to force-feedback mechanisms. A haptic controller integrates the catheter model, blood flow models, and synthetic fluoroscopy renderer. Hemodynamic models affect fluid flow and subsequent fluoroscopic appearance. Geometric models of anatomy and devices used during procedures provide tissue-tool interactions. The user interface relays information about the physiologic state of the patient (hemodynamic model) and the progress of the procedure through the fluoroscopic display.	5
1.4	Cross-sectional format of a typical IVUS image. The bright-dark-bright, three-layered appearance is seen in the image with corresponding anatomy as defined. The IVUS represents the imaging catheter in the blood vessel lumen. Histologic correlation with intima, media, and adventitia are shown. The media has lower ultrasound reflectance owing to less collagen and elastin compared with neighboring layers. Because the intimal layer reflects ultrasound more strongly than the media [40], there is a spillover in the image, which results in a slight overestimation of the thickness of the intima and a corresponding underestimation of the medial thickness (black and white image). Figure extracted from Moscucci [26].	6
2.1	(a) A Bezier curve defined by 7 control points representing the trajectory $\alpha(t)$. The orthonormal vectors \mathbf{T} , \mathbf{N} , and \mathbf{B} are illustrated at a particular point. (b) The parametric curve $\xi_t(u)$ changes its shape smoothly. The cross section in this example is a circumference with variable radius.	11

2.2 Top view of connected arteries having polylines with the same number of vertices (open points). The 3D segments are represented by white and light colored areas separated by planar polylines. When two planes intersect some vertices are removed and the truncated polylines have two vertices in common: one at the top (black point) and one at the bottom (not shown). The shape of the arteries is arbitrary, since the only requirement is that the black point remains in the line given by the intersection of the two planes. The black lines represent additional planes that split the volume between adjacent arteries. We show in (a) a T-like bifurcation and in (b) a Y-like bifurcation. 13

2.3 (a) Image from a bifurcation of the Abdominal Aorta into the Common Iliac Arteries. The image was extracted using the **Vascular Modeling Toolkit** software, which can also determine the central line $\alpha(t)$ (not shown). Virtual representation using planar polylines (b) in a T-like bifurcation and (c) in a Y-like bifurcation. Although both bifurcations styles can be applied, in this case the Y-like bifurcation looks more natural. For simplicity, the resolution is low with $N_v = 24$ vertices, and the triangularization is not displayed in order to make the Figure clear. 14

2.4 Cross section in the middle of a segment *i.e.* between two planar polylines. In this example each polyline has $N_v = 8$ vertices and there are $2N_v = 16$ triangular SE (red lines) defining the topology of the artery segment. Additional lateral planes (black lines) are used to divide the volume outside the artery between adjacent SE. Notice that the planes represented by lines are not perpendicular to the Figure but are inclined. (a) Cross section of an artery segment divided as slices of a cake (green lines). In practice the division need not be symmetric. (b) Further subdivision using a single additional plane per subsegment (blue lines). 15

2.5 (a) Side view of the catheter joint at position \mathbf{x} between two vertices at $\mathbf{r}_A, \mathbf{r}_B$. The green lines go through A, B , and are parallel to the unit vectors $\hat{\mathbf{m}}_A, \hat{\mathbf{m}}_B$, respectively. The vectors $\mathbf{x}, \hat{\mathbf{m}}_A$, and $\hat{\mathbf{m}}_B$ are not in the plane of the Figure. (b) Top view of the joint over a triangular SE. The unit vectors $\hat{\mathbf{t}}_{ij}$ are not in the plane of the Figure, and the vectors \mathbf{F}_{ij} are not perpendicular to the plane of the Figure. 16

2.6 Workflow of steps 1–5 to calculate the force \mathbf{F}_{ABC} between the wire and the artery wall. 18

2.7 (a₁) Concave intersection KLM . As a point moves along the line $DEFGH$, the distance s to the planes KL and LM (perpendicular to the Figure) varies continuously as shown in (a₂). (b₁) Convex intersection KLM . As a point moves along the line DFH , the distance s to the planes KL and LM has the dependence shown in (b₂), which is not continuous at point F 19

-
- 2.8 Main window of the Modeler software. The sweep surface in red is built over a real model of coronaries in blue (kindly yielded by LNCC www.lncc.br). The central line is a Bezier curve (cyan) with 4 control points. 21
- 2.9 (a) “*Builder of Sections*” auxiliary window. Here it is possible to edit the planar curves which are swept over the main curve. (b) “*Builder of Bifurcations*” auxiliary window. In this window, the planar curves from the bifurcations are edited. The green point in both windows represents the intersection of the central line and the plane which contains the planar curves. 22
- 3.1 Cross view of the arterial ring in the stress-free reference configuration (not to scale, see Fig. 1.4). The geometrical parameters are the inner radius R_{in} , the tissue thicknesses a_{i} , a_{m} , a_{a} , and the opening angle α . 27
- 3.2 (a) Four nodes (black points) are connected by two springs of stiffness κ_{θ} (red lines), two springs of stiffness κ_z (green lines), and two springs of stiffness κ_{d} (blue lines). Increasing the distance b_{θ} by $b_{\theta}\varepsilon_{\theta\theta}$ (tangential direction) and the distance b_z by $b_z\varepsilon_{zz}$ (axial direction), also increases the length of the diagonal b_{d} . (b) Two adjacent non coplanar rectangles ($\varphi_0 \neq 0$) have two angular springs of stiffness τ connected to straight lines joining the nodes (e.g. $\mathbf{r}_2 - \mathbf{r}_1$ and $\mathbf{r}_3 - \mathbf{r}_1$). The axis of rotation is the unit vector $\hat{\mathbf{n}}_z$. (c) Two adjacent coplanar rectangles have two angular springs of stiffness ζ . The axis of rotation is $\hat{\mathbf{n}}_{\theta}$ 29
- 3.3 (a) Cross view of two adjacent rectangles perpendicular to the plane of the Figure, with nodes at the coordinates \mathbf{r}_1 , \mathbf{r}_2 and \mathbf{r}_1 , \mathbf{r}_3 . The vectors \mathbf{r}_{12} and \mathbf{r}_{13} are the projections of $\mathbf{r}_2 - \mathbf{r}_1$ and $\mathbf{r}_3 - \mathbf{r}_1$ in the plane of the Figure. Without deformation, the moduli r_{12} and r_{13} are both equal to b_{θ} . The unit vector $\hat{\mathbf{n}}_z$, represented by the dot \bullet , is perpendicular to the Figure. When the rectangles are rotated along the axis defined by $\hat{\mathbf{n}}_z$, the structure is bent with a curvature radius R . The stiffness of the angular springs connected to the rectangles is τ (blue). (b) The unit vector $\hat{\mathbf{m}}$ is perpendicular to $\hat{\mathbf{n}}_{\theta}$ and to $\hat{\mathbf{r}}_{45} - \hat{\mathbf{r}}_{46}$. The lengths δs_{45} and δs_{46} are the projections of $\delta \mathbf{r}_5 - \delta \mathbf{r}_4$ and $\delta \mathbf{r}_6 - \delta \mathbf{r}_4$ along $\hat{\mathbf{m}}$. Hence, up to first order $\delta \varphi_{45} = \delta s_{45}/r_{45}$ and $\delta \varphi_{46} = \delta s_{46}/r_{46}$ 31
- 3.4 When the rectangle in Fig. 3.2(a) is deformed and/or rotated, the lengths and the orientations (relative to the tangential and axial directions) are modified. For simplicity, only the length $b_{\theta 1}$ and the angle $\beta_{\theta 1}$ are shown. The spring stiffnesses between the nodes are the same as before. 34

- 3.5 (a) If the adjacent rectangles in Fig. 3.3(a) are not rectangles with the same dimensions, then the bending radius on the right (R_{12}) and the bending radius on the left (R_{13}) are different. The distances between the points are replaced by $b_{\theta 12} = 2R_{12} \sin(\varphi/2)$ and $b_{\theta 13} = 2R_{13} \sin(\varphi/2)$. It is possible to join the points using the same radius $R_{12} = R_{13}$ but different angles $\varphi_{12} \neq \varphi_{13}$. However, in this case, the line defining the beam will not be smooth when connecting consecutive parts, since the radius and the center of the circles (e.g. through $\mathbf{r}_3, \mathbf{r}_1, \mathbf{r}_2$ and through $\mathbf{r}_1, \mathbf{r}_2, \mathbf{r}_4$) will not coincide. (b) Top view of Fig. (a). Note that the points $\mathbf{r}'_1, \mathbf{r}'_2$, and \mathbf{r}'_3 are not represented because they are hidden behind $\mathbf{r}_1, \mathbf{r}_2$, and \mathbf{r}_3 . The sum $V_{\theta 12} + V'_{\theta 12}$ is equal to one half of V_{right} (the volume of the yellow region of thickness h defined by the points $\mathbf{r}_1, \mathbf{r}_2, \mathbf{r}'_2$, and \mathbf{r}'_1) and $V'_{\theta 12}/V_{\theta 12} = V'_{\theta 13}/V_{\theta 13}$ 35
- 3.6 View of a voxel (cyan) corresponding to the volume V of the arterial wall delimited by a quadrilateral parallel to the yz plane (shadow). The normal to the arterial wall points in the x axis direction. For a given z , the integration area (red) of Eq. (3.40) is parallel to the xy plane. The neutral axis (black line) depends on the z coordinate. . . 39
- 3.7 Cross view of the artery discretized by a polyline. The angle is $\theta = 2\pi/24$ and the inner radius (with an internal pressure equal to \bar{p}_{in}) is $r_1 = 1.55$ mm. Thus, the rectangle dimensions in Fig. 3.2 are $b_{\theta} = 2r_1 \sin(\theta/2) = 0.405$ mm and $b_z = b_{\theta} (\bar{c}_{zzzz}/\bar{c}_{\theta\theta\theta\theta})^{1/4} = 0.449$ mm. 39
- 3.8 (a) Four springs of stiffness κ (connected in parallel and then in series) are joined by rigid vertical bars (blue). (b) Two springs connected in parallel are equivalent to one spring of stiffness $\kappa_p = \kappa + \kappa = 2\kappa$ [137]. (c) The two springs connected in series are equivalent to one spring of stiffness $\kappa_s = \kappa_p \kappa_p / (\kappa_p + \kappa_p) = \kappa_p / 2$ 40
- 3.9 Axial view of the artery submitted to different boundary conditions. (a) The pressure p_{in} increases and the axial length z_1 is kept constant. As a result, the tangential stretch and the radius r_1 vary (bottom). (b) The pressure is kept constant at \bar{p}_{in} , the length increases from z_1 (top) to z'_1 (bottom), and the radius becomes smaller ($r_1 \rightarrow r'_1$). . . . 43
- 3.10 Average circumferential stretch $\bar{\lambda}_{\theta}$ as a function of blood pressure p_{in} without residual strain and without external surface traction. The red, blue, and green lines correspond to the calculations with model A (this work), with model B (nonlinear and incompressible artery of Holzapfel et al. [127]), and with model C (one dimensional FEM). . . 44

3.11 Bending of a planar artery subjected to a uniform vertical load. The triangle and the circle at the ends support the artery vertically: the triangle is fixed but the circle can move freely in the horizontal direction (green arrows). The black curve represents Eq. (3.46) and the red points are the result of the calculations performed with the model developed in this work. 46

3.12 Logarithm of the ET as function of the tangential stretch λ_θ (a, b, c) and of the axial stretch λ_z (d, e, f) in the interval $[1, 1.1]$. The constant c_0 is equal to 1 MPa. The different colors indicate the ET components $c_{\theta\theta\theta\theta}$ (red), c_{zzzz} (green), and $c_{\theta\theta zz}$ (blue). The results are given for the Intima (a, d), Media (b, e), and Adventitia (c, f) tissues. 47

4.1 (a) The wire has a curved tip (red) with M segments. They are numbered from the proximal end to the distal end of the wire. (b) The new segment (green) points to the same direction as the segment number $n - M$, and the total number increases to $n + 1$ 51

4.2 The wire geometry. The difference between the coordinates of two consecutive joints $\mathbf{x}_j - \mathbf{x}_{j-1}$ is equal to the vector $\boldsymbol{\lambda}_j$, which has a constant length λ . Changing $\boldsymbol{\lambda}_i$ modifies only $\mathbf{x}_i, \mathbf{x}_{i+1}, \dots, \mathbf{x}_{n-1}, \mathbf{x}_n$, and the difference between the new and the old coordinates $\mathbf{x}'_j - \mathbf{x}_j = \boldsymbol{\lambda}'_j - \boldsymbol{\lambda}_j$ is the same for $j = i, i + 1, \dots, n - 1, n$ 52

4.3 Three successive points $\mathbf{x}_{i-1}, \mathbf{x}_i$, and \mathbf{x}_{i+1} separated by an equal distance $\lambda = |\boldsymbol{\lambda}_i| = |\boldsymbol{\lambda}_{i+1}|$ define a circular arc of radius R_i and angle $2\theta_i$ 54

4.4 The minimum energy of a wire without external forces results when $\boldsymbol{\lambda}_{i-1}$ is parallel to $\boldsymbol{\lambda}_i$, and $\boldsymbol{\lambda}_i$ is parallel to $\boldsymbol{\lambda}_{i+1}$. If $\boldsymbol{\lambda}_{i-1} = \mathbf{x}_{i-1} - \mathbf{x}_{i-2} + \boldsymbol{\omega}_i$, $\boldsymbol{\lambda}_i = \mathbf{x}_i - \mathbf{x}_{i-1}$, and $\boldsymbol{\lambda}_{i+1} = \mathbf{x}_{i+1} - \mathbf{x}_i - \boldsymbol{\omega}_{i+1}$, then the equilibrium is obtained when $\mathbf{x}_{i-2}, \mathbf{x}_{i-1}, \mathbf{x}_i$, and \mathbf{x}_{i+1} are in the positions indicated. Thus, the vectors $\boldsymbol{\omega}_i$ bend a free wire. 55

4.5 The lengths of the vectors $\boldsymbol{\lambda}_i$ (old), $\boldsymbol{\lambda}'_i$ (new) are equal, and the modulus of $\boldsymbol{\alpha}_i = \boldsymbol{\lambda}'_i - \boldsymbol{\lambda}_i$ is a_i . Further, the unit vector $\hat{\mathbf{u}}_i$ is parallel to $\boldsymbol{\lambda}_i$ and perpendicular to $\hat{\mathbf{t}}_i = \cos \psi_i \hat{\mathbf{v}}_i + \sin \psi_i \hat{\mathbf{w}}_i$, where ψ_i represents the azimuthal angle of $\boldsymbol{\alpha}_i$ around $\boldsymbol{\lambda}_i$ 57

4.6 Three points $\mathbf{x}_{i-1}, \mathbf{x}_i$, and \mathbf{x}_{i+1} are separated by different distances $|\boldsymbol{\lambda}_i| \neq |\boldsymbol{\lambda}_{i+1}|$. The two circular arcs have the same angle θ_i but the radii R_i and R_{i+1} are not equal. 61

4.7 (a) Original curve \mathbf{x}_i (red), curve after executing the energy minimization \mathbf{x}_i^* (green), and displaced points \mathbf{x}'_i (black). (b) Closer view of three coordinates $\mathbf{x}_{i-2}^*, \mathbf{x}_{i-1}^*$, and \mathbf{x}_i^* after the minimization. The unit vector $\hat{\mathbf{u}}_i^*$ points from \mathbf{x}_{i-1}^* to \mathbf{x}_i^* , and the vector \mathbf{b}_{ij} goes from \mathbf{x}'_{j-1} to the line passing through \mathbf{x}_{i-1}^* and \mathbf{x}_i^* . The distance between \mathbf{x}'_{j-1} and \mathbf{x}'_j equals λ 64

- 4.8 Second order correction $\varepsilon_{ij}\hat{\mathbf{e}}_i^*$ to the coordinate \mathbf{x}'_j . The displacement is indicated by the green arrow. The arc segment has an angle $\bar{\theta}_i^*$ and a radius R_i^* . The distance between \mathbf{x}_{i-1}^* and \mathbf{x}_i^* is λ_i^* , and the distance between \mathbf{x}'_j and \mathbf{x}_i^* is d_{ij} 65
- 4.9 Wire segments inside an artery. In order to relax, the segment $\overline{P_1P_2}$ should rotate upwards about point P_1 as indicated by the arrow. Note that from P_2 to P_6 the wire is rigid, so that the resulting translation is hindered by the contact points P_3 and P_4 . Nor can it move downwards because of P_5 . The GR is not subjected to this restriction, since from P_3 up to P_6 the wire can slide. It is especially designed to relax intervals like from P_0 to P_3 (red). 68
- 4.10 Workflow. In the “Tip Relaxation” (Section 4.2.1) the procedure `PhysicalUpdate` is applied to the tip of the wire and also to some selected segments. When the “Physical Relaxation” is called, $\frac{1}{2}m(m+1)$ updates are executed. The PR is completed if the cycle ends, i.e. after $\frac{1}{2}n(n+1)$ updates. In the same way, when the “Geometrical Relaxation” is called, $m(m+1)/(\nu-\mu)$ iterations are executed to improve the curve. The GR is completed after $\nu-\mu$ iterations. . . . 69
- 4.11 Photography (top-view) and sketch (cross-view) of the wire device. The pipe has a small window and the mouse is over the window. Translating and rotating the wire also translates and rotates the cylinder, which is captured by the mouse. 70
- 4.12 Artery with a T-like and a Y-like bifurcation. (Left) The wire has 250 segments, $\lambda = 1$ mm, and it has been quickly inserted into the artery (green curve). In this part, the program executed only Tip Relaxations and the time consumed was 0.24 seconds. In the second part, no action takes place and a combination of 100 relaxation cycles (Physical and Geometrical) is executed, so that equilibrium is attained (blue curve). The coordinates indicate the location of some wire joints. (Right) Mockup representing the stiff artery. The wire inserted in the artery has the same shape as the blue curve. The average separation between the physical wire (plot digitized with WebPlotDigitizer 3.8 <http://arohatgi.info/WebPlotDigitizer>) and the blue curve is 0.262 mm, with a standard deviation of 0.227 mm. Hence, the calculations with the model developed in this work give a realistic result. 72
- 4.13 The green wire A has $n_A = 100$ segments, $\lambda_A = 2.5$ mm and the blue wire B has $n_B = 250$ segments, $\lambda_B = 1$ mm. Hence $n_A\lambda_A = n_B\lambda_B$. The arrows indicate one of the intervals $\mu < i < \nu$ where the GR is applied. In the case of wire A it was found that $\mu_A = 1$, $\nu_A = 13$ and in the case of wire B it was found that $\mu_B = 2$, $\nu_B = 30$. Thus, μ and ν are closely proportional to n 74

4.14	GR relaxation time t_{geo} as function of the interval length $\nu - \mu$. The blue color represents the wire B with $n_B = 250$ segments (blue curve in Fig. 4.13) and the red color represents the wire C with $n_C = 625$ segments (not shown in Fig. 4.13). The points are the PT measured in numerical simulations and the lines are the fits performed with Eq. (4.34).	75
4.15	Initial curve (green) and the final equilibrium curve (blue) obtained after a very long relaxation time. The final result is the same with or without the GR. The analysis is focussed in the wire portion located inside the gray box, which goes from wire segment number 90 to 95. In this interval are seen the most relevant changes during relaxation.	76
4.16	The red bars represent the percentage of the time in which each joint (blue curve in Fig. 4.12) is in contact with the artery's surface. The magenta curve represents the average modulus of the unit vector update $\Delta \hat{\mathbf{u}}_i$ during a PR cycle.	77
4.17	Comparison of the functions $g(\theta)$ (red; exact), $g_1(\theta)$ (blue; this work), and $g_2(\theta)$ (green; Alderliesten et al. [12]) in the interval $0 < \theta < \pi/2$.	78
4.18	View of the normal perspective frame from the simulator, showing a fictive left coronary. The user goal is to reach the green ball at the end of the artery. In this case, the implementation follows the idea of “ <i>serious games</i> ” [188, 189], where there is a primary purpose (increase the ability using the wire) other than pure entertainment. .	81
4.19	View of the wire perspective. This is useful to elucidate the overlap situations of two or more arteries, helping the physician to understand the bifurcation.	82

List of Tables

3.1	Average physical parameters from Holzapfel et al. [127] for the Intima (i), Media (m), and Adventitia (a) tissues. The thickness a_t is in mm, μ_t and k_{1t} are in kPa, k_{2t} and ρ_t are dimensionless, and the angle ϕ_t is in degrees.	26
3.2	Ratio between the physical parameters for $R'_{\text{in}} = 2R_{\text{in}}$ and two different layer thicknesses: (i) $h' = h$, (ii) $h' = 2h$. In the calculations the values $R_{\text{in}} = 1.35$ mm and $h = a_i + a_m + a_a = 0.90$ mm are used.	41
3.3	Dependence of the internal radius r_1 on the axial stretch λ_z for a constant pressure equal to \bar{p}_{in}	45
4.1	PT of the PR (t_{phy}) and of the GR (t_{geo}) for different resolutions: $\lambda_A = 2.5$ mm, $\lambda_B = 1.0$ mm, and $\lambda_C = 0.4$ mm. The PT does not include the fast insertion of the wire, but only the relaxation between the green and the blue curves in Fig. 4.12. The approximated times $t_{\text{phy,fit}}$ and $t_{\text{geo,fit}}$ have been obtained with Eq. (4.33).	73
4.2	Survey of the initial simulator applied in a conference in 2011 with a dozen specialized participants. The grade scale goes from 1 (poor) to 5 (optimal).	79

List of Algorithms

3.1	Calculation of the spring constants for a right circular cylindrical artery. The input geometrical parameters are the tissue thicknesses a_i , a_m , a_a , the internal radius R_{in} , the opening angle α , and the axial stretch λ_z . The physical parameters are those appearing in Eqs. (3.1)–(3.4). Finally, n_{vert} represents the number of vertices of the polyline discretizing the artery in the tangential direction and \bar{p}_{in} is the average internal pressure.	37
4.1	Pseudocode of the PR method. The entrance parameter is the segment i of the wire. The procedure updates the points \mathbf{x}_j and orientations ω_j from $j = i$ up to the end of the wire $j = n$	60
4.2	Pseudocode of the GR method. The entrance parameter is the entire wire. The procedure chooses the best interval of the wire to apply the GR and updates the points \mathbf{x}_j from $j = \mu + 1$ up to the end $j = n$	67

References

- [1] C.S. Basdogan, J. Kim, M. Muniyandi, and M.A. Srinivasan. **Haptics in minimally invasive surgical simulation and training.** *IEEE Computer Graphics and Applications*, 24:56–64, 2004.
- [2] V. Velanovich. **Laparoscopic vs open surgery: a preliminary comparison of quality-of-life outcomes.** *Surg Endosc*, 14:16–21, 2000.
- [3] K.H. Fuchs. **Minimally invasive surgery.** *Endoscopy*, 34:154–159, 2002.
- [4] P. Pessaux, M. Diana, L. Soler, T. Piardi, D. Mutter, and J. Marescaux. **Robotic duodenopancreatectomy assisted with augmented reality and real-time fluorescence guidance.** *Surgical endoscopy*, 28:2493–2498, 2014.
- [5] I. Larrabide, P.J. Blanco, S.A. Urquiza, E.A. Dari, M.J. Venere, N.A. de Souza e Silva, and R.A. Feijoo. **HeMoLab - Hemodynamics Modelling Laboratory: an application for modelling the human cardiovascular system.** *Comp Biol Med*, 42:993–1004, 2012.
- [6] S.A. Engum, P. Jeffries, and L. Fisher. **Intravenous catheter training system: Computer-base education versus tradition learning methods.** *The American Journal of Surgery*, 186:67–74, 2003.
- [7] J.S. Tsang, P.A. Naughton, S. Leong, A.D.K. Hill, C.J. Kelly, and A.L. Leahy. **Virtual reality simulation in endovascular surgical training.** *The Surgeon*, 6:214–220, 2008.
- [8] S.P. Pakes, editor. *Guide for the Care and Use os Laboratory Animals*. U.S. Department of Health and Human Service, National Institutes of Health, 1th edition, 1985.
- [9] T. Mori, N. Hatano, S. Maruyama, and Y. Atomi. **Significance of hands-on training in laparoscopic surgery.** *Surgical Endoscopy*, 12:256–260, 1998.
- [10] A. Lunderquist, K. Ivancev, S. Wallace, I. Enge, F. Laerum, and A. Kolbenstvedt. **The acquisition of skills in interventional radiology by supervised training on animal models: a three year multicenter experience.** *Cardiovascular and Interventional Radiology*, 18:209–211, 1995.

- [11] T.R. Coles, D. Meglan, and N. John. **The role of haptics in medical training simulators: A survey of the state of the art.** *IEEE Transactions on Haptics*, 4:51–66, 2011.
- [12] T. Alderliesten, M.K. Konings, and W.J. Niessen. **Simulation of minimally invasive vascular interventions for training purposes.** *Computer Aided Surgery*, 9:3–15, 2004.
- [13] C.U. Cates, L. Lönn, and A.G. Gallagher. **Prospective, randomised and blinded comparison of proficiency-based progression full-physics virtual reality simulator training versus invasive vascular experience for learning carotid artery angiography by very experienced operators.** *BMJ Simulation and Technology Enhanced Learning*, pages bmjstel–2015, 2016.
- [14] B. Gao, K. Hu, and S. Guo. **Collision detection algorithm based on aabb for minimally invasive surgery.** In *Mechatronics and Automation (ICMA), 2014 IEEE International Conference on*, pages 315–320. IEEE, 2014.
- [15] A.G. Gallagher and C.U. Cates. **Approval of virtual reality training for carotid stenting: What this means for procedural-based medicine.** *Journal of the American Medical Association*, 292:3024–3026, 2004.
- [16] R.C. Orth, M.J. Wallace, and M.D. Kuo. **C-arm cone-beam ct: General principles and technical considerations for use in interventional radiology.** *Journal of Vascular and Interventional Radiology*, 19:814–820, 2008.
- [17] N.R. Balaji and P.B. Shah. **Radial artery catheterization.** *Circulation*, 124:e407–e408, 2011.
- [18] D. Kasper, editor. ***Harrison’s Principles of Internal Medicine.*** McGraw-Hill Education, Columbus, OH, 19th edition, 2015.
- [19] S.S. Ahrabi, M. Shojafar, H.K. Esfeh, and A. Abraham. **Mathematical modeling of blood flow through an eccentric catheterized artery: A practical approach for a complex system.** In *Hybrid Intelligent Systems (HIS), 2014 14th International Conference on*, pages 315–321. IEEE, 2014.
- [20] D.C. Rosenman, D. Kayser, and P.A. Altman. **Devices and methods for accessing the vasculature of a patient**, 2015. US Patent App. 14/876,268.
- [21] D.J. Sogard and S. Savitt. **Perfusion balloon catheter**, 1990. US Patent 4,944,745.
- [22] R. Hess. **Catheter with high tactile guide wire**, 1992. US Patent 5,120,308.

-
- [23] M.K. Konings, S. Weiss, C.J.G. Bakker, L.W. Bartels, and W.P.T.M. Mali. **Catheters and guidewires in interventional mri: problems and solutions.** *Medica Mundi*, 45, 2001.
- [24] Y. Haga, T. Mineta, and M. Esashi. **Active catheter, active guide wire and related sensor systems.** In *Proceedings of the 5th Biannual World Automation Congress*, volume 14, pages 291–296, 2014.
- [25] Z. Li, C.-K. Chui, J.H. Anderson, X. Chen, X. Ma, W. Hua, Q. Peng, Y. Cai, Y. Wang, and W.L. Nowinski. **Computer environment for interventional neuroradiology procedures.** *Simulation & Gaming*, 32:404–419, 2001.
- [26] M. Moscucci. *Grossman & Baim’s Cardiac Catheterization, Angiography, and Intervention.* Lippincott Williams & Wilkins, Philadelphia, PA, 8th edition, 2014.
- [27] M.J. Mack. **Minimally invasive and robotic surgery.** *JAMA*, 285:568–572, 2001.
- [28] H. Chen, R. Kim, D. Perret, J. Hata, J. Rinehart, and E. Chang. **Improving trainee competency and comfort level with needle driving using simulation training.** *Pain Medicine*, page pnv056, 2015.
- [29] R.H. Riley. *Manual of Simulation in Healthcare.* Oxford University Press, Oxford, UK, 2th edition, 2016.
- [30] S. Rudin, D.R. Bednarek, and K.R. Hoffmann. **Endovascular image-guided interventions (EIGIs).** *Med Phys*, 35:301–309, 2008.
- [31] F. Argelaguet, D.A.G Jauregui, M. Marchal, and A. Lecuyer. **Elastic images: Perceiving local elasticity of images through a novel pseudo-haptic deformation effect.** *ACM Trans. Appl. Percept.*, 10:1–14, 2013.
- [32] M. Mahvash, V. Hayward, and J.E. Lloyd. **Haptic rendering of tool contact.** pages 110–115, Proc: Eurohaptics; Edinburgh, Scotland, 2002.
- [33] J.A. Gordon, D.N. Tancredi, W.D. Binder, W.M. Wilkerson, and D.W. Shaffer. **Assessment of a clinical performance evaluation tool for use in a simulator-based testing environment: A pilot study.** *Journal of the Association of American Medical Colleges*, 78:S45–S47, 2003.
- [34] W.I.M. Willaert, R. Aggarwal, I. Herzeele, N.J. Cheshire, and F.E. Vermassen. **Recent advancements in medical simulation: Patient-specific virtual reality simulation.** *World Journal of Surgery*, 36:1703–1712, 2012.
- [35] S.L. Dawson, S. Cotin, D. Meglan, D.W. Shaffer, and M.A. Ferrell. **Designing a computer-based simulator for interventional cardiology training.** *Catheterization and Cardiovascular Interventions*, 51:522–527, 2000.

- [36] M. Sanz-Lopez, J. Dequidt, E. Kerrien, C. Duriez, M. Berger, and S. Cotin. **Testbed for assessing the accuracy of interventional radiology simulations.** In *Biomedical Simulation*, pages 106–111, 2014.
- [37] W. Gerstner and R. Naud. **How good are neuron models?** *Science*, 326:379–380, 2009.
- [38] S. Eckert, U. Gleichmann, O. Zagorski, and A. Klapp. **Validation of the omron r3 blood pressure self-measuring device through simultaneous comparative invasive measurements according to protocol 58130 of the german institute for validation.** *Blood pressure monitoring*, 2:189–192, 1997.
- [39] P. Badel, S. Avril, M.A. Sutton, and S.M. Lessner. **Numerical simulation of arterial dissection during balloon angioplasty of atherosclerotic coronary arteries.** *Journal of Biomechanics*, 47:878–889, 2014.
- [40] J. Persson, J. Formgren, B. Israelsson, and G. Berglund. **Ultrasound-determined intima-media thickness and atherosclerosis. direct and indirect validation.** *Arteriosclerosis, Thrombosis, and Vascular Biology*, 14:261–264, 1994.
- [41] L.H. Peterson, R.E. Jensen, and J. Parnell. **Mechanical properties of arteries in vivo.** *Circulation Research*, 8:622–639, 1960.
- [42] R.R. Diehl, D. Linden, D. Lücke, and P. Berlit. **Phase relationship between cerebral blood flow velocity and blood pressure.** *Stroke*, 26:1801–1804, 1995.
- [43] B. Folkow. **Intravascular pressure as a factor regulating the tone of the small vessels.** *Acta Physiologica*, 17:289–310, 1949.
- [44] A. Yamashina, H. Tomiyama, K. Takeda, H. Tsuda, a. Tomio, K. Hirose, K. Yutaka, and Y. Yamamoto. **Validity, reproducibility, and clinical significance of noninvasive brachial-ankle pulse wave velocity measurement.** *Hypertension research*, 25:359–364, 2002.
- [45] E.D. Boland, J.A. Matthews, K.J. Pawlowski, D.G. Simpson, G.E. Wnek, and G.L. Bowlin. **Electrospinning collagen and elastin: preliminary vascular tissue engineering.** *Frontiers in Bioscience*, 9:1422–1432, 2004.
- [46] C.M. García-Herrera, D.J. Celentano, M.A. Cruchaga, J.M. Atienza F.J. Rojo, G.V. Guinea, and J.M. Goicole. **Mechanical characterisation of the human thoracic descending aorta: experiments and modelling.** *Comput Methods Biomech Biomed Engin*, 15:185–193, 2012.
- [47] T. Pereira, C. Correia, and J. Cardoso. **Novel methods for pulse wave velocity measurement.** *J Med Biol Eng*, 35:555–565, 2015.

-
- [48] G.A. Holzapfel, T.C. Gasser, and M. Stadler. **A structural model for the viscoelastic behavior of arterial walls: continuum formulation and finite element analysis.** *European J Mech A/Solids*, 21:441–463, 2002.
- [49] T. Alderliesten, M.K. Konings, and W.J. Niessen. **Modeling friction, intrinsic curvature, and rotation of guide wires for simulation of minimally invasive vascular interventions.** *IEEE Transactions on Biomedical Engineering*, 54:29–38, 2007.
- [50] Y. Wang, S. Guo, T. Tamiya, H. Hirata, and H. Ishihara. **A blood vessel deformation model based virtual-reality simulator for the robotic catheter operating system.** *Neurosci Biomed Eng*, 2:126–131, 2014.
- [51] F.T. Zohora and A.Y.M.A. Azim. **Inkjet printing: an emerging technology for 3d tissue or organ printing.** *European Scientific Journal*, 10(30), 2014.
- [52] P.N.T. Wells and H.D. Liang. **Medical ultrasound: imaging of soft tissue strain and elasticity.** *J R Soc Interface*, 8:1521–1549, 2011.
- [53] W. Li. **Damage models for soft tissues: A survey.** *J Med Biol Eng*, 36:285–307, 2016.
- [54] S.H. Strogatz. *Nonlinear dynamics and chaos: with applications to physics, biology, chemistry, and engineering.* Westview press, Boulder, CO, 2nd edition, 2014.
- [55] P.A. Baier and P.C.P. Carvalho. **Optimal software-based projector alignment.** *1st Ibero-American Symposium in Computer Graphics*, 2002.
- [56] P.A. Baier, N. Petri, W. Voelker, and K. Schilling. **Simulation of virtual arteries based on sweep surfaces.** *Society in Europe for Simulation applied to medicine*, 1:43–43, 2010.
- [57] P.A. Baier and K. Schilling. **A simple and inexpensive wire motion capture device to the simulation of catheter procedures.** *Society in Europe for Simulation applied to medicine*, 1:150–151, 2011.
- [58] P.A. Baier and K. Schilling. **Linear collision detection method to a sequenced points guide wire inside of arteries modeled by sweep surfaces.** *Society in Europe for Simulation applied to medicine*, 1:151–152, 2011.
- [59] J.A. Baier-Saip, M.H. Gutierrez, A.L. Cabrera, and P.A. Baier. **Hysteresis in the rhombohedral orthorhombic phase transition of knbo₃ under inhomogeneous strain.** *Solid State Communications*, 154:6–10, 2013.

- [60] L. Srinivasan, P.A. Baier, C. Herrmann, J. Scharnagl, and K. Schilling. **Redefining voting to enable simultaneous multioperator robot navigation.** *IFAC-PapersOnLine*, 48:170–175, 2015.
- [61] P.A. Baier, L. Srinivasan, J.A. Baier-Saip, W. Voelker, and K. Schilling. **Surfaces for modeling arteries in virtual reality simulators.** *IFAC-PapersOnLine*, 48:031–036, 2015.
- [62] J.A. Baier-Saip, P.A. Baier, K. Schilling, and J.C. Oliveira. **Approximate artery elasticity using linear springs.** *Journal of Medical and Biological Engineering*, 37:899–911, 2017.
- [63] P.A. Baier, J.A. Baier-Saip, K. Schilling, and J. C. Oliveira. **Simulator for minimally invasive vascular interventions: hardware and software.** *Presence*, 25:108–128, 2016.
- [64] M.K. Konings, E.B. van de Kraats, T. Alderliesten, and W.J. Niessen. **Analytical guide wire motion algorithm for simulation of endovascular interventions.** *Medical & Biological Engineering & Computing*, 41:689–700, 2003.
- [65] J. Kretschmer, C. Godenschwager, B. Preim, and M. Stamminger. **Interactive patient-specific vascular modeling with sweep surfaces.** *IEEE Transactions on Visualization and Computer Graphics*, 19:2828–2837, 2013.
- [66] F. Remondino. **From point cloud to surface: the modeling and visualization problem.** *International Archives of Photogrammetry, Remote Sensing and Spatial Information Sciences*, 34:W10, 2003.
- [67] C. Schumann, S. Oeltze, R. Bade, B. Preim, and H. Peitgen. **Model-free surface visualization of vascular trees.** *IEEE Eurographics Symposium on Visualization*, pages 283–290, 2007.
- [68] J. Wu, M. Wei, Y. Li, X. Ma, F. Jia, and Q. Hu. **Scale-adaptive surface modeling of vascular structures.** *BioMedical Engineering OnLine*, 9:75, 2010.
- [69] P. Felkl, R. Wegenkittl, and K. Bühler. **Surface models of tube trees.** In *Proceedings of Computer Graphics International*, pages 70–77, 2004.
- [70] H.K. Hahn, B. Preim, D. Selle, and H.O. Peitgen. **Visualization and interaction techniques for the exploration of vascular structures.** *IEEE Visualization*, pages 395–402, 2001.
- [71] Y. Zhang, Y. Bazilevs, S. Goswami, C.L. Bajaj, and T.J. Hughes. **Patient-specific vascular nurbs modeling for isogeometric analysis of blood flow.** *Computer methods in applied mechanics and engineering*, 196:2943–2959, 2007.

-
- [72] J.A. Moore, D.A. Steinman, and D.W. Holdsworth. **Accuracy of computational hemodynamics in complex arterial geometries reconstructed from magnetic resonance imaging.** *Annals of Biomedical Engineering*, 27:32–41, 1999.
- [73] S. Oeltze and B. Preim. **Visualization of vasculature with convolution surfaces: method, validation and evaluation.** *IEEE Transactions on Medical Imaging*, 24:540–548, 2005.
- [74] J. Kretschmer, T. Beck, C. Tietjen, B. Preim, and M. Stamminger. **Reliable adaptive modelling of vascular structures with non-circular cross-sections.** *Computer Graphics Forum (EuroVis)*, 31:1055–1064, 2012.
- [75] S. Diepenbrock and T. Ropinski. **From imprecise user input to precise vessel segmentations.** In *EG Visual Computing for Biology and Medicine*, pages 65–72, 2012.
- [76] C. Wang and Ö. Smedby. **Integrating automatic and interactive methods for coronary artery segmentation: let the pacs workstation think ahead.** *International journal of computer assisted radiology and surgery*, 5:275–285, 2010.
- [77] G.D. Santis, M.D. Beule, K.D. Canneyt, P. Segers, P. Verdonck, and B. Verhegghe. **Full-hexahedral structured meshing for image-based computational vascular modeling.** *Med Eng Phys*, 33:1318–1325, 2011.
- [78] J.R. Cebal, R. Löhner, P.L. Choyke, and P.J. Yim. **Merging of intersecting triangulations for finite element modeling.** *Journal of Biomechanics*, 34:815–819, 2001.
- [79] D. Gillet, H.A. Latchman, C. Salzmann, and O.D. Crisalle. **Hands-on laboratory experiments in flexible and distance learning.** *Journal of Engineering Education*, 90:187, 2001.
- [80] P. Jiménez, F. Thomas, and C. Torras. **3D collision detection: a survey.** *Computers & Graphics*, 25:269–285, 2001.
- [81] G. Farin. *Curves and Surfaces for Computer Aided Geometric Design: A Practical Guide*. Harcourt Brace Jovanovich, San Diego, CA, 3rd edition, 1992.
- [82] A.A.G. Requicha. **Representations for rigid solids: theory, methods and systems.** *Computing Surveys*, 12:437–464, 1980.
- [83] L.A. McCullough. *An Analysis of the Numerical Solution of the Frenet-Serret Equations*. University of Virginia, Charlottesville, VA, 1st edition, 1978.

- [84] W.P. Thurston and S. Levy. ***Three-Dimensional Geometry and Topology***. Princeton Mathematical Series. Princeton University Press, Princeton, NJ, 1997.
- [85] S. Cotin, S. Dawson, D. Meglan, D. Shaffer, M. Ferrell, R. Bardsley, F. Morgan, T. Nagano, J. Nikom, and P. Sherman. **Icts, an interventional cardiology training system**. *Studies in health technology and informatics*, pages 59–64, 2000.
- [86] A. Goldsztejn and L. Jaulin. **Inner and outer approximations of existentially quantified equality constraints**. *Lecture Notes in Comput. Sci.*, 4204:198–212, 2006.
- [87] P. Lanzer. ***Catheter-Based Cardiovascular Interventions: A Knowledge-Based Approach***. Springer Science & Business Media, Heidelberg, Germany, 1st edition, 2012.
- [88] F. Wang, L. Duratti, E. Samur, U. Spaelter, and H. Bleuler. **A computer-based real-time simulation of interventional radiology**. In *2007 29th Annual International Conference of the IEEE Engineering in Medicine and Biology Society*, pages 1742–1745, 2007.
- [89] B.-S.K. Skagerstam. **Stochastic mechanics and dissipative forces**. *Journal of Mathematical Physics*, 18:308–311, 1977.
- [90] M. Woo, J. Neider, T. Davis, and D. Shreiner. ***OpenGL Programming Guide: The Official Guide to Learning OpenGL, Version 1.2***. Addison-Wesley Longman, Boston, MA, 3rd edition, 1999.
- [91] J. Diez. **Arterial stiffness and extracellular matrix**. *Advanced Cardiology*, 44:76–95, 2007.
- [92] M.E. Safar, J. Blacher, J.J. Mourad, and G.M. London. **Stiffness of carotid artery wall material and blood pressure in humans**. *Stroke*, 31:782–790, 2000.
- [93] G.A. Holzapfel, J.A. Niestrawska, R.W. Ogden, A.J. Reinisch, and A.J. Schrief. **Modelling non-symmetric collagen fibre dispersion in arterial walls**. *J R Soc Interface*, 12:20150188, 2015.
- [94] G.A. Holzapfel and R.W. Ogden. **Constitutive modelling of arteries**. *Proceedings of the Royal Society of London A: Mathematical, Physical and Engineering Sciences*, 466:1551–1597, 2010.
- [95] L. Robert, A. Kadar, and B. Robert. ***The Macromolecules of the Intercellular Matrix of the Arterial Wall: Collagen, Elastin, Proteoglycans, and Glycoproteins***, pages 85–123. Springer US, Boston, MA, 1974.

-
- [96] A. Maton, J. Hopkins, C.W. McLaughlin, S. Johnson, M.Q. Warner, D. LaHart, and J.D. Wright. **Human Biology and Health**. Prentice Hall, Englewood Cliffs, NJ, 2nd edition, 1999.
- [97] E. Gentleman, A.N. Lay, D.A. Dickerson, E.A. Nauman, G.A. Livesay, and K.C. Dee. **Mechanical characterization of collagen fibers and scaffolds for tissue engineering**. *Biomaterials*, 24:3805–3813, 2003.
- [98] L.H. Timmins, Q. Wu, A.T. Yeh, J.E. Moore, and S.E. Greenwald. **Structural inhomogeneity and fiber orientation in the inner arterial media**. *American Journal of Physiology-Heart and Circulatory Physiology*, 298:H1537–H1545, 2010.
- [99] P.B. Canham, H.M. Finlay, J.G. Dixon, D.R. Boughner, and A. Chen. **Measurements from light and polarised light microscopy of human coronary arteries fixed at distending pressure**. *Cardiovasc Res*, 23:973–982, 1989.
- [100] H.M. Finlay, L. McCullough, and P.B. Canham. **Threedimensional collagen organization of human brain arteries at different transmural pressures**. *Journal of Vascular Research*, 32:301–312, 1995.
- [101] H.M. Finlay, P. Whittaker, and P.B. Canham. **Collagen organization in the branching region of human brain arteries**. *Stroke*, 29:1595–1601, 1998.
- [102] A.J. Schriebl, A.J. Reinisch, S. Sankaran, D.M. Pierce, and G.A. Holzapfel. **Quantitative assessment of collagen fiber orientations from two-dimensional images of soft biological tissues**. *Journal of the Royal Society Interface*, pages 3081–3093, 2012.
- [103] G.A. Holzapfel. **Collagen in Arterial Walls: Biomechanical Aspects**, pages 285–324. Springer US, Boston, MA, 1st edition, 2008.
- [104] D.M. Pierce, T.E. Fastl, B. Rodriguez-Vila, P. Verbrugghe, I. Fourneau, G. Maleux, P. Herijgers, E.J. Gomez, and G.A. Holzapfel. **A method for incorporating three-dimensional residual stretches/stresses into patient-specific finite element simulations of arteries**. *J Mech Behav Biomed Mater*, 47:147–164, 2015.
- [105] Y.C. Fung. **Biomechanics: Mechanical Properties of Living Tissues**. Springer, 1993.
- [106] J.D. Humphrey. **Cardiovascular Solid Mechanics: Cells, Tissues, and Organs**. Springer-Verlag, 2002.
- [107] R.P. Vito and S.A. Dixon. **Blood vessel constitutive models: 1995-2002**. *Annu Rev Biomed Eng*, 5:413–439, 2003.

- [108] D.P. Sokolis. **Passive mechanical properties and constitutive modeling of blood vessels in relation to microstructure.** *Med Biol Eng Comput*, 46:1187–1199, 2008.
- [109] N.J. Driessen, C.V. Bouten, and F.P. Baaijens. **A structural constitutive model for collagenous cardiovascular tissues incorporating the angular fiber distribution.** *Biomech Eng*, 127:494–503, 2005.
- [110] M. Carboni, G.W. Desch, and H.W. Weizsacker. **Passive mechanical properties of porcine left circumflex artery and its mathematical description.** *Med Eng Phys*, 29:8–16, 2007.
- [111] P. Saez, E. Pena, and M.A. Martinez. **A structural approach including the behavior of collagen cross-links to model patient-specific human carotid arteries.** *Ann Biomed Eng*, 42:1158–1169, 2014.
- [112] M.R. Hill, X. Duan, G.A. Gibson, S. Watkins, and A.M. Robertson. **A theoretical and non-destructive experimental approach for direct inclusion of measured collagen orientation and recruitment into mechanical models of the artery wall.** *Journal of Biomechanics*, 45:762–771, 2012.
- [113] A.N. Gent. ***Engineering with Rubber - How to Design Rubber Components.*** Carl Hanser Verlag, Munich, Germany, 2012.
- [114] R.L. Taylor. ***The Finite Element Method, Volume 1: The Basis.*** Butterworth-Heinemann, Woburn, MA, 5th edition, 2000.
- [115] M. Garcia, C. Mendoza, L. Pastor, and A. Rodriguez. **Optimized linear FEM for modeling deformable objects.** *Comp Anim Virtual Worlds*, 17:393–402, 2006.
- [116] I.M. Smith, D.V. Griffiths, and L. Margetts. ***Programming the Finite Element Method.*** John Wiley & Sons Ltd, 15th edition, 2014.
- [117] S. Misra, K.T. Ramesh, and A.M. Okamura. **Modeling of tool-tissue interactions for computer-based surgical simulation: a literature review.** *Presence (Camb)*, 17:463–491, 2008.
- [118] M. Bro-Nielsen. **Finite element modeling in surgery simulation.** *Proc IEEE*, 86:490–503, 1998.
- [119] X. Wang and V. Devarajan. **Improved 2d mass-spring-damper model with unstructured triangular meshes.** *Visual Comput*, 24:57–75, 2008.
- [120] P. Chen, K.E. Barner, and K.V. Steiner. **A displacement driven real-time deformable model for haptic surgery simulation.** In *Proceedings of 2006 14th Symposium on Haptic Interfaces for Virtual Environment and Teleoperator Systems*, pages 499–505, 2006.

-
- [121] D. Zhang, T. Wang, D. Liu, and G. Lin. **Vascular deformation for vascular interventional surgery simulation.** *Int J Med Robot Comput Assist Surg*, 6:170–177, 2010.
- [122] E. Johnson, Y. Zhang, and K. Shimada. **Estimating an equivalent wall-thickness of a cerebral aneurysm through surface parameterization and a non-linear spring system.** *Int J Numer Meth Biomed Engng*, 27:1054–1072, 2011.
- [123] M. Harders, R. Hutter, A. Rutz, P. Niederer, and G. Székely. **Comparing a simplified fem approach with the mass-spring model for surgery simulation.** *Stud Health Technol Inform*, 94:103–109, 2003.
- [124] K. Sprangera, C. Capelli, G.M. Bosi, S. Schievano, and Y. Ventikos. **Comparison and calibration of a real-time virtual stenting algorithm using finite element analysis and genetic algorithms.** *Comput. Methods Appl. Mech. Engrg*, 293:462–480, 2015.
- [125] P. Pedersen and N.L. Pedersen. **Design of material anisotropic constitutive mmatrices for structural stiffness and strength optimization.** In H. Rodrigues, J. Herskovits, C.M. Soares, J.M. Guedes, A. Araujo, J. Folgado, F. Moleiro, and J.A. Madeira, editors, *Engineering Optimization IV*, volume 4, pages 169–174, Lisbon, Portugal, 2014. CRC Press.
- [126] J. Ophir, I. Cespedes, H. Ponnekanti, Y. Yazdi, and X. Li. **Elastography: A quantitative method for imaging the elasticity of biological tissues.** *Ultrasonic Imaging*, 13:111–134, 1991.
- [127] G.A. Holzapfel, G. Sommer, C.T. Gasser, and P. Regitnig. **Determination of layer-specific mechanical properties of human coronary arteries with nonatherosclerotic intimal thickening and related constitutive modeling.** *Am J Physiol Heart Circ Physiol*, 289:H2048–H2058, 2005.
- [128] G.A. Holzapfel, T.C. Gasser, and R.W. Ogden. **A new constitutive framework for arterial wall mechanics and a comparative study of material models.** *J Elast*, 61:1–48, 2000.
- [129] C.J. Chuong and Y.C. Fung. **Compressibility and constitutive equation of arterial wall in radial compression experiments.** *Journal of Biomechanics*, 17:35–40, 1984.
- [130] A. Karimi, T. Sera, S. Kudo, and M. Navidbakhsh. **Experimental verification of the healthy and atherosclerotic coronary arteries incompressibility via digital image correlation.** *Artery Research*, 16:1–7, 2016.
- [131] R.W. Ogden. *Non-linear elastic deformations.* Dover Publications, New York, NY, 1997.

- [132] I.E. Vignon-Clementel, C.A. Figueroa, K.E. Jansen, and C.A. Taylor. **Out-flow boundary conditions for three-dimensional finite element modeling of blood flow and pressure in arteries.** *Computer Methods in Applied Mechanics and Engineering*, 195:3776–3796, 2006.
- [133] J. Loncaric. **Normal forms of stiffness and compliance matrices.** *IEEE Journal on Robotics and Automation*, 3:567–572, 1987.
- [134] R.M. Sanford, S.A. Crawford, M.G. Doyle, C.H. Amon, and T.L. Forbes. **Predicting iliac artery deformation in response to guidewire insertion using computational simulations.** *Journal of Vascular Surgery*, 64:1546, 2016.
- [135] H. Schmid, A. Grytsan, E. Poshtan, P.N. Watton, and M. Itskov. **Influence of differing material properties in media and adventitia on arterial adaptation - application to aneurysm formation and rupture.** *Comput Methods Biomech Biomed Engin*, 16:33–53, 2013.
- [136] E. O’Brien, G. Parati, G. Stergiou, R. Asmar, L. Beilin, G. Bilo, D. Clement, A. de la Sierra, P. de Leeuw, E. Dolan, R. Fagard, J. Graves, G. Head, Y. Imai, K. Kario, E. Lurbe, J-M. Mallion, G. Mancia, T. Mengden, M. Myers, G. Ogedegbe, T. Ohkubo, S. Omboni, P. Palatini, J. Redon, L. Ruilope, A. Shennan, J. Staessen, G. vanMontfrans, P. Verdecchia, B. Waeber, J. Wang, A. Zanchetti, and Y. Zhang. **European society of hypertension position paper on ambulatory blood pressure monitoring.** *Journal of Hypertension*, 31:1731–1768, 2013.
- [137] D. Halliday, R. Resnick, and J. Walker. *Fundamentals of Physics*. John Wiley & Sons, Danvers, MA, 9th edition, 2011.
- [138] C. Lanczos. *The Variational Principles of Mechanics*. Dover Books On Physics. Dover Publications, Mineola, NY, 4th edition, 1970.
- [139] S. Estrada, M.K. O’Malley, C. Duran, D. Schulz, and J. Bismuth. **On the development of objective metrics for surgical skills evaluation based on tool motion.** In *2014 IEEE International Conference on Systems, Man, and Cybernetics (SMC)*, pages 3144–3149, 2014.
- [140] C. Morin and S. Avril. **Inverse problems in the mechanical characterization of elastic arteries.** *MRS Bulletin*, 40:317–323, 2015.
- [141] A. Delfino, N. Stergiopoulos, J.E. Moore, and J.-J. Meister. **Residual strain effects on the stress field in a thick wall finite element model of the human carotid bifurcation.** *J. Biomechanics*, 30:777–786, 1997.
- [142] C.A.J. Schulze-Bauer, P. Regitnig, and G.A. Holzapfel. **Mechanics of the human femoral adventitia including the high-pressure response.** *Am J Physiol Heart Circ Physiol*, 282:H2427–H2440, 2002.

-
- [143] A.E. Kerdok, S.M. Cotin, M.P. Ottensmeyer, A.M. Galea, R.D. Hove, and S.L. Dawson. **Thruth cube: establishing physical standards for soft tissue simulation.** *Med Image Anal*, 7:283–291, 2003.
- [144] J.M. Gere and B.J. Goodno. *Mechanics of Materials*. Global Engineering, Stamford, CT, 8th edition, 2012.
- [145] I. Mirsky. **Ventricular and arterial wall stresses based on large deformation analyses.** *Biophysical Journal*, 13:1141–1159, 1973.
- [146] A. Hemmasizadeh, M. Autieri, and K. Darvish. **Multilayer material properties of aorta determined from nanoindentation tests.** *J Mech Behav Biomed Mater*, 15:199–207, 2012.
- [147] M.T. Mason. **On the scope of quasi-static pushing.** In *International Symposium on Robotics Research*, pages 229–233, Cambridge, MA, 1986. MIT Press.
- [148] J. Brown, J.C. Latombe, and K. Montgomery. **Real-time knot-tying simulation.** *The Visual Computer*, 20:165–179, 2004.
- [149] M. Müller, T.J. Kim, and N. Chentanez. **Fast simulation of inextensible hair and fur.** In *Workshop on Virtual Reality Interaction and Physical Simulation (VRIPhys)*. The Eurographics Association, 2012.
- [150] M.B. Rubin. *Cosserat Theories: Shells, Rods and Points*. Solid Mechanics and its Applications. Springer, 2000.
- [151] D.K. Pai. **STRANDS: Interactive Simulation of Thin Solids using Cosserat Models.** *Computer Graphics Forum*, 21:347–352, 2002.
- [152] D.Q. Cao and R.W. Tucker. **Nonlinear dynamics of elastic rods using the cosserat theory: Modelling and simulation.** *International Journal of Solids and Structures*, 45:460–477, 2008.
- [153] Z.J. Gao, X.L. Xie, G.B. Bian, J.L. Hao, Z.Q. Feng, and Z.G. Hou. **Fast and stable guidewire simulator for minimally invasive vascular surgery.** In *Engineering in Medicine and Biology Society (EMBC), 2015 37th Annual International Conference of the IEEE*, pages 5809–5812, 2015.
- [154] J.S. Przemieniecki. *Theory of Matrix Structural Analysis*. Dover Civil and Mechanical Engineering. Dover, Mineola, NY, 1985.
- [155] C. Duriez, S. Cotin, J. Lenoir, and P. Neumann. **New approaches to catheter navigation for interventional radiology simulation.** *Computer Aided Surgery*, 11:300–308, 2006.

- [156] X. Wu, J. Allard, and S. Cotin. **Real-time modeling of vascular flow for angiography simulation.** In *Int. Conf. Medical Image Computing and Computer-Assisted Intervention*, pages 557–565. MICCAI Society, 2007.
- [157] J. Dequidt, J. Lenoir, and S. Cotin. **Interactive contacts resolution using smooth surface representation.** In *Int. Conf. Medical Image Computing and Computer-Assisted Intervention*, pages 850–857. MICCAI Society, 2007.
- [158] P. Moore and D. Molloy. **A survey of computer-based deformable models.** In *Int. Conf. Machine Vision and Image Processing*, pages 55–66. IMVIP, 2007.
- [159] V. Luboz, R. Blazewski, D. Gould, and F. Bello. **Real-time guidewire simulation in complex vascular models.** *The Visual Computer*, 25:827–834, 2009.
- [160] H. Kodama, C. Shi, S. Ikeda, T. Fukuda, F. Arai, M. Negoro, and I. Takahashi. **Catheter motion capture with optical encoder at the insertion port to find the reference area of catheter insertion.** In *Micro-NanoMechatronics and Human Science (MHS), 2012 International Symposium on*, pages 235–238, 2012.
- [161] P.F. Hokayem and M.W. Spong. **Bilateral teleoperation: An historical survey.** *Automatica*, 42:2035–2057, 2006.
- [162] Y. Yu, J. Guo, S. Guo, and L. Shao. **Modelling and analysis of the damping force for the master manipulator of the robotic catheter system.** In *Mechatronics and Automation (ICMA), 2015 IEEE International Conference on*, pages 693–697, 2015.
- [163] X. Yin, S. Guo, H. Hirata, and H. Ishihara. **Design and experimental evaluation of a teleoperated haptic robot-assisted catheter operating system.** *Journal of Intelligent Material Systems and Structures*, 27:3–16, 2014.
- [164] T. Alderliesten, P.A.N. Bosman, and W.J. Niessen. **Towards a real-time minimally-invasive vascular intervention simulation system.** *IEEE Transactions on Medical Imaging*, 26:128–132, 2006.
- [165] K. Takashima, S. Tsuzuki, A. Ooike, K. Yoshinaka, K. Yu, M. Ohta, and K. Mori. **Numerical analysis and experimental observation of guidewire motion in a blood vessel model.** *Medical Engineering & Physics*, 36:1672–1683, 2014.
- [166] K. Pearson. **The problem of the random walk.** *Nature*, 72:294, 1905.
- [167] J. Nocedal and S.J. Wright. *Numerical Optimization.* (Springer Science+Business Media, New York, NY, 2nd edition, 2000.

-
- [168] J.A. Nelder and R. Mead. **A simplex method for function minimization.** *The computer journal*, 7:308–313, 1965.
- [169] S.P. Timoshenko. **History of strength of materials.** McGraw-Hill, New York, NY, 1st edition, 1953.
- [170] R.H. Bartels, J.C. Beatty, and B.A. Barsky. **An Introduction to Splines for Use in Computer Graphics and Geometric Modeling.** Morgan Kaufmann, San Mateo, CA, 1st edition, 1987.
- [171] D. Wackerly, W. Mendenhall, and R.L. Scheaffer. **Mathematical Statistics with Applications.** Thomson Higher Education, Belmont, CA, 7th edition, 1987.
- [172] V. Fuster and R. O'Rourke. **Hurst's the Heart.** McGraw-Hill Professional, New York, NY, 12th edition, 2007.
- [173] Y. Fujii and T. Yamaguchis. **Optical method for evaluating material friction.** *Measurement Science and Technology*, 15:1971, 2004.
- [174] A. Manbachi and R.S.C. Cobbold. **Development and application of piezoelectric materials for ultrasound generation and detection.** *Ultrasound*, 19:187–196, 2011.
- [175] T.J. Palermo. **Steerable guidewire with soft adjustable tip**, 1989. US Patent 4,886,067.
- [176] S.J. Biggs and M.A. Srinivasan. **Haptic Interfaces**, pages 93–116. Lawrence Erlbaum, London, England, 1st edition, 2002.
- [177] D. d'Aulignac, R. Balaniuk, and C. Laugier. **A haptic interface for a virtual exam of the human thigh.** In *Proceedings 2000 ICRA. Millennium Conference. IEEE International Conference on Robotics and Automation. Symposia Proceedings (Cat. No.00CH37065)*, volume 3, pages 2452–2457, 2000.
- [178] J.D. Foley, A. Dam, S.K. Feiner, and J.F. Hughes. **Computer Graphics: Principles and Practice in C.** Addison-Wesley Professional, Boston, MA, 2nd edition, 1995.
- [179] J.J. Espindola and J.M.S Neto. **Identification of flexural stiffness parameters of beams.** *Journal of the Brazilian Society of Mechanical Sciences*, 23:217 – 225, 2001.
- [180] E. Tatli, A. Buturak, A. Cakar, B.M. Vatan, A. Degirmencioglu, T.M. Agac, H. Kilic, H. Gunduz, and R. Akdemir. **Unusual vascular complications associated with transradial coronary procedures among 10,324 patients: Case based experience and treatment options.** *Journal of Interventional Cardiology*, 28:305–313, 2015.

- [181] F. Farooqi, J. Alexander, and A. Sarma. **Rare vascular perforation complicating radial approach to percutaneous coronary angioplasty.** *BMJ Case Reports*, 2013.
- [182] Y. Lin, K. Guo, and S. Paul. **Sync-ms: synchronized messaging service for real-time multi-player distributed games.** In *10th IEEE International Conference on Network Protocols, 2002. Proceedings.*, pages 155–164, 2002.
- [183] M. Fabien, F. Devernay, G. Malandain, and E. Coste-Maniere. **3D+t Modeling of Coronary Artery Tree from Standard Non Simultaneous Angiograms**, pages 1320–1322. Springer Berlin Heidelberg, Berlin, Germany, 2001.
- [184] A. Kaladji, A. Dumenil, M. Castro, A. Cardona, J.P. Becquemind, B. Bou-Saide, A. Lucas, and P. Haigron. **Prediction of deformations during endovascular aortic aneurysm repair using finite element simulation.** *Computerized Medical Imaging and Graphics*, 37:142–149, 2013.
- [185] W. Tang, P. Lagadec, D. Gould, T. Wan, J. Zhai, and T. How. **A realistic elastic rod model for real-time simulation of minimally invasive vascular interventions.** *The Visual Computer*, 26:1157–1165, 2010.
- [186] L.M. Haskvitz and E.C. Koop. **Students struggling in clinical? A new role for the patient simulator.** *Journal of Nursing Education*, 43:181–184, 2004.
- [187] I.B. Vijayalakshmi. **Cardiac Catheterization and Imaging (From Pediatrics to Geriatrics).** Jaypee Brothers, Medical Publishers Pvt. Ltd, New Delhi, India, 1st edition, 2015.
- [188] H.F. O’Neil, R. Wainess, and E.L. Baker. **Classification of learning outcomes: evidence from the computer games literature.** *The Curriculum Journal*, 16:455–474, 2005.
- [189] D. Michael and S. Chen. **Serious Games: Games That Educate, Train, and Inform.** Cengage Learning PTR, Mason, OH, 2005.
- [190] M. Andreucci, R. Solomon, and A. Tasanarong. **Side effects of radiographic contrast media: Pathogenesis, risk factors, and prevention.** *BioMed Research International*, 2014:20 pages, 2014.
- [191] M.J. Kern. **The Cardiac Catheterization Handbook.** Saunders Elsevier, Philadelphia, PA, 5th edition, 2011.
- [192] P. Lanzer and E.J. Topol. **Pan Vascular Medicine: Integrated Clinical Management.** Springer-Verlag Berlin Heidelberg, New York, NY, 1st edition, 2012.